Study of the Inclusive Characteristics of Secondary Charged Particles Produced in the Hadron Nucleus Collisions at LHC Energies

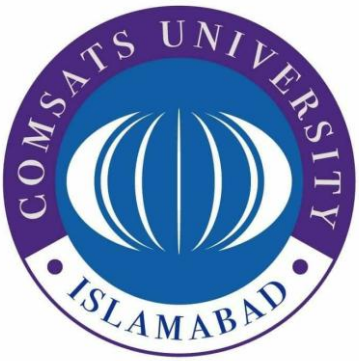

By

Qasim Ali

CIIT/FA14-PPH-005/ISB

PhD Thesis

In

Physics

COMSATS University Islamabad
Islamabad-Pakistan

Spring, 2019

COMSATS University Islamabad

Study of the Inclusive Characteristics of Secondary Charged Particles Produced in the Hadron Nucleus Collisions at LHC Energies

A Thesis Presented to

COMSATS University Islamabad

In partial fulfillment

of the requirement for the degree of

PhD (Physics)

By

Qasim Ali

CIIT/FA14-PPH-005/ISB

Spring, 2019

Study of the Inclusive Characteristics of Secondary Charged Particles Produced in the Hadron Nucleus Collisions at LHC Energies

A Post Graduate Thesis submitted to the Department of Physics as partial fulfillment of the requirement for the award of Degree of Ph.D in Physics.

Name	Registration Number
Qasim Ali	CIIT/FA14-PPH-005/ISB

Supervisor:

Dr. Mahnaz Q. Haseeb
Professor Department of Physics
COMSATS University Islamabad

Co-Supervisor:

Dr. Yasir Ali
Assistant Professor Department of Physics
COMSATS University Islamabad

Certificate of Approval

This is to certify that the research work presented in this thesis, entitled "Study of the Inclusive Characteristics of Secondary Charged Particles Produced in the Hadron Nucleus Collisions at LHC Energies" was conducted by Qasim Ali, CIIT/FA14-PPH-005/ISB, PhD Scholar, under the supervision of Professor Dr. Mahnaz Q. Haseeb. No part of this thesis has been submitted anywhere else for any other degree. This thesis is submitted to the Department of Physics, COMSATS University Islamabad, in the partial fulfillment of the requirement for the degree of Doctor of Philosophy in the field of Physics.

Student Name*:* Qasim Ali Signature: _____

Examinations Committee:

Signature: _____
Prof. Dr. Jameel-Un Nabi
Pro-Rector (Academic)
Department of Physics
GIK Swabi kpk.

Signature: _____
Prof. Dr. Bilal Masud
Director
Centre for High Energy Physics
University of the Panjab Lahore.

Signature: _____
Prof. Dr. Mahnaz Q. Haseeb
Supervisor
Department of Physics
CUI Islamabad.

Signature: _____
Prof. Dr. Muhammad Anis ur Rehman
HoD
Department of Physics
CUI Islamabad.

Signature: _____
Prof. Dr. Sadia Manzoor
Chairperson, Department of Physics
CUI Islamabad.

Signature: _____
Prof. Dr. Arshad Saleem Bhatti
Dean, Faculty of Science
CUI Islamabad.

Author's Declaration

I Qasim Ali, CIIT/FA14-PPH-005/ISB, hereby state that my PhD thesis titled "Study of the Inclusive Characteristics of Secondary Charged Particles Produced in the Hadron Nucleus Collisions at LHC Energies" is my own work and has not been submitted previously by me for taking any degree from this university i.e. COMSATS University Islamabad or anywhere else in the country/world.

At any time if my statement is found to be incorrect even after I graduate the university has the right to withdraw my PhD degree.

Date: _____

Qasim Ali

CIIT/FA14-PPH-005/ISB

Plagiarism Undertaking

I solemnly declare that research work presented in the thesis titled "Study of the Inclusive Characteristics of Secondary Charged Particles Produced in the Hadron Nucleus Collisions at LHC Energies" is solely my research work with no significant contribution from any other person. Small contribution/help wherever taken has been duly acknowledged and that complete thesis has been written by me.

I understand the zero tolerance policy of HEC and COMSATS University Islamabad towards plagiarism. Therefore, I as an author of the above titled thesis declare that no portion of my thesis has been plagiarized and any material used as reference is properly referred/cited.

I undertake that if I am found guilty of any formal plagiarism in the above titled thesis even after award of PhD Degree, the University reserves the right to withdraw/revoke my PhD degree and that HEC and the university has the right to publish my name on the HEC/university website on which names of students are placed who submitted plagiarized thesis.

Date: _____

Qasim Ali

CIIT/FA14-PPH-005/ISB

Certificate

It is certified that Mr. Qasim Ali, Registration number CIIT/FA14-PPH-005/ISB has carried out all the work related to this thesis under my supervision at the Department of Physics, COMSATS University Islamabad and the work fulfills the requirement for award of PhD degree.

Date: _____ Supervisor:

_____
Prof. Dr. Mahnaz Q. Haseeb
Professor Department of Physics

Head of Department:

_____
Prof. Dr. Muhammad Anis ur Rehman
Head, Department of Physics

DEDICATED

to

My Beloved Parents and Family

ACKNOWLEDGEMENTS

All the praise to Almighty Allah, the most benevolent, merciful and the creator of the universe who enabled me to complete this dissertation. My thanks would be incomplete without mentioning the Prophet Muhammad (PBUH), who always encouraged people to explore the nature. First of all I would like to pay my heartiest thanks to my supervisor **Prof. Dr. Mahnaz Qadir Haseeb** for her great support. She helped me to the utmost level to achieve my goal. Despite of her very tough routine, she was ready to help me in difficult situations. I am also thankful to Head, all other academic staff and other staff members of the Department of Physics, CUI, Islamabad, for their help in academic matters as well as research facilities throughout my PhD program.

I would like to pay my special thanks to my co-supervisor **Dr. Yasir Ali** for his great support, guidance and encouragement me at all stages of my research. Without his careful consideration and encouragement this research work could have never been completed.

I would like to pay special thanks from the core of my heart to my supervisory committee members **Dr. Maiz Suleymonov**, **Dr. Uzma Tabassam and Dr. M. Ajaz** for their support, guidance throughtout my research work. I got a lot of knowledge from them during my research work as well as during my presentation.

I would like to thanks Dr. Jamila Bashir Butt, Dr. Farida Tahir, Dr. Sohail Amjad, Dr. Azeem Mir and Dr. Qamrul Hassan for their encouragement and support. I would like to special thanks of Dr. Fazal Ghafoor, Dr. Salman Khan Safi, Dr. Ziauddin, Dr. Anwar Ali, Dr. Mushtaq, Dr. Rahmatullah and Dr. Rashid for their encouragement. My heartiest thanks to all my friends especially Shakir Ullah, Haleema Sadia Qureshi, Leena (mashra), Shahid Khan, Mujeeb Khan, Atif Arif, Mukhtar Ahmad, Rubab, Qamar, Ibrar Ahmad, Omair Sarfraz, Obaid Ullah Jan, Akhtar Iqbal Khattak, Abdul Muneem, Tufail, Gul Tiaz, Hamid (pir sb), Nasir Khan, Hisham Al-Nasir, Musaddiq, Irshad Marwat, Gohar Ali and Anum with whom I spent some of unforgettable moments of life during my Ph.D. I also want to remember and thank Dr. Khusniddin Olimov for his support, guidance and encouragement.

I also want to mention and pay special thanks to my brothers Mehboob Ali, Zulfiqar Ali, Akbar Ali, Wajid Ali, Javed Ali (bala), Murad Ali (chahchay), and sisters (S, K) who always prayed for my better future. I would never forget to thank my mother in law, sister in law (Wali Khan) and father in law for support, cares and helping me through out my Ph.D work. Great thanks to my family for their unconditional support, belief in me and keeping me grounded. I also want to mention and say special thanks to Salman Khan and brother in law Mukhtiar Ali and Muhammad Alamgir Khan. I am profoundly thankful to my caring wife for her love and support throughout my PhD tenure.

Last but not least I wish to record my deepest obligation to my mother and father for every thing they have done for me (May Allah give them long life and good health, ameen).

Qasim Ali
CIIT/FA14-PPH-005/ISB

ABSTRACT

Study of the Inclusive Characteristics of Secondary Charged Particles Produced in the Hadron Nucleus Collisions at LHC Energies

We have studied inclusive characteristics of secondary charged particles produced in p-Pb collisions at LHC energies using simulated data obtained from different models. We used: HIJING-1.0, UrQMD-3.4, EPOS-LHC, EPOS-1.99, QGSJETII-04 and SIBYLL-2.3c, models to generate 150k events for p-Pb and pp interactions. The results have been compared with ALICE, ATLAS, and CMS data. The nuclear modification factor was calculated using the pp collisions as a reference. The charged particles density as a function of charged particles multiplicity, average transverse momentum as a function of charged particles multiplicity, charged particles density as a function of pseudorapidity and charged particles multiplicity have been studied for the pp collisions. We have found that: universality behaviour for the characteristics of the charged high p_T particles is observed; the UrQMD model gives more suppression as compared to HIJING-1.0 which shows some medium effect; the EPOS-LHC, EPOS-1.99, QGSJETII-04 codes give good predictions for the soft interactions and only EPOS-LHC can explain hard interactions satisfactorily. The model shows that the pions at low p_T are absorbed by the medium weakly than can be expected; the Cronin-like enhancement was observed for the (anti) protons with intermediate p_T; no suppression is observed in the p-Pb collisions; EPOS-LHC model describes the experimental data better as compared to the EPOS-1.99 and QGSJETII-04.

TABLE OF CONTENTS

LIST OF FIGURES

LIST OF TABLES

LIST OF ABBREVIATIONS

QCD	Quantum Chromodynamics
QGP	Quark Gluon Plasma
HIC	Heavy Ions Collisions
LHC	Large Hadrons Collider
RHIC	Relativistic Heavy Ions Collider
CERN	European Organization for Nuclear Research
SM	Standard Model
SLAC	Stanford Linear Accelerator Centre
QED	Quantum Electrodynamics
QFT	Quantum Field Theory
MC	Monte Carlo
BBT	Big Bang Theory
pQCD	Perturbative Quantum Chromodynamics
PDG	Particle Data Group
SPS	Super Protonsynchrotron
NMF	Nuclear Modification Factor
pp	Proton-Proton
p-Pb	Proton-Lead
Pb-Pb	Lead-Lead
GRT	Gribov-Regge Theory
EAS	Extensive Air Shower
CM	Centre of Mass Energy
HEP	High Energy Physics

LIST OF PUBLICATIONS

This thesis is based on the following publications

1. **Q**.**Ali**, Y. Ali, M. Haseeb, U. Tabassam, M. Ajaz, and S. Ullah, "Study of transverse momentum distributions in p-Pb interactions at 0.9 TeV and 5.02 TeV", Mod. Phys. Lett. A **33,** 1850179 (2018).
2. **Q. Ali**, Y. Ali, M. Haseeb, and M. Ajaz, "Transverse Momentum and nuclear modification factor distribution of charged particles in p+Pb and p+p collisions at $\sqrt{s_{NN}}$ = 5.02 TeV", Mod. Phys. Lett. A **33**, 1950120 (2019).
3. Y. Ali, **Q. Ali,** M. Haseeb, M. Ajaz, and U. Tabassam, "Study of Pseudorapidity and Transverse Momentum Distributions of Charged Particles in pp Interactions at $\sqrt{s_{NN}}$ = 13 TeV Using Hadrons Production Models" IJTP **58** (2019).
4. **Q. Ali**, Y. Ali, M. Haseeb, and M. Ajaz, "Distributions of charged particles transverse momentum and pseudorapidity in pp collisions at 0.9 TeV", Pis'ma v ZhETF **109** (2019).
5. U. Tabassam, Y. Ali, and **Q. Ali**, *et al*., "Observation of universality for high p_T distribution at LHC energies", Int. J. Mod. Phys. E **27**, 1850036 (2018).
6. **Q. Ali**, Y. Ali, and M. Haseeb, *et al*., "Distributions of charged particles transverse momentum and pseudorapidity in pp collisions at 0.9 TeV", JETP Lett. **109** (2019).
7. **Q. Ali**, Y. Ali, and M. Haseeb, *et al*., "Study of p_T distributions and nuclear modification factor of charged particles production in p-Pb interaction at LHC energies", (JETP Letter, Under reveiw).
8. **Q. Ali**, Y. Ali, M. Haseeb, *et al*., "Distribution of strange particles transverse momentum and rapidity in high energy proton-proton collisions at $\sqrt{s_{NN}}$ = 0.9 TeV at LHC", Mod. Phys. Lett. A **33** 2050006 (2020).
9. **Q. Ali**, Y. Ali, M. Haseeb, *et al*., "Transverse momentum and rapidity distribution of strange particles in pp collisions at $\sqrt{s_{NN}}$ = 7 TeV", Phys. Particle and Nucl. Lett. (Under review).

OTHER PUBLICATIONS

1. **Q. Ali**, Y. Ali, M. Haseeb, and M. Ajaz, "Study of pseudorapidity distributions ofcharged particles in pp collisions at $\sqrt{s_{NN}}$ = 8 TeV using hadrons production models" Chinese J. Phys. (Under review).
2. **Q. Ali**, Y. Ali, M. Haseeb *et al.,* "Some characteristics of the midrapidity charged hadrons produced in the pp collisions at 7 TeV", JETP (Under review).
3. M. Ajaz, Y. Ali, **Q. Ali** *et al.,* "Comparison of different hadron production model forthe study of $\pi^{\pm}$, $K^{\pm}$, protons and antiprotons production in proton-carbon interactionat90 GeV/c", Mod. Phys. Lett. A **33,** 1850079 (2018).
4. Khusniddin K. Olimov, **Q. Ali**, *et al.,* "Phenomenological analysis of rapiditydistribution negative pions in central C^{12} + C^{12} collisions at $\sqrt{s_{NN}}$ = 3.14 GeV", Int. J. Mod. Phys. E **24**, 1550049 (2015).
5. S. Ullah, Y. Ali, **Q. Ali**, *et al.,* "$\pi^{\pm}$, $K^{\pm}$, protons and antiprotons production inproton-carbon interactions at 31 GeV/c using hadron production models", Int. J. Mod. Phys. A **33**, 1850108 (2018).
6. M. Ajaz, Y. Ali, **Q. Ali** *et al.,* "Study of Hadron Produced in Proton-Carbon Interactions at 120 GeV/c Using Hadron Production Models", Phys. Atomic. Nucl. **82**, 291 (2019).

Chapter 1

INTRODUCTION

Particle physics [1] is concerned with the fundamental constituents of matter and the forces through which these constituents interact with each other. The study of fundamental particles is done in elementary particle physics, or high energy physics. Electrons and nuclei build atoms of all the matter around us and these nuclei are further composed of neutrons as well as protons. These neutrons and protons are then made up of quarks. In free form quarks can not exist but only in the form of bound states called hadrons.

The field which connect nuclear physics with high energy physics is called ultra-relativistic heavy ion collisions physics [2]. Here the ultra-relativistic energies refer to the energy regime where, as compared to the rest energy, the kinetic energy is significantly higher and the term "heavy-ions" refers to heavy atomic nuclei. Study of the properties of the dense and hot nuclear or hadronic matter is possible only through elementary interactions of subatomic particles at relativistic energies [3]. One of the fundamental theory which explains the interactions between gluons and quarks is called the Quantum Chromodynamics (QCD).

If the condensed matter is heated up then a phase transition occurs into a gas phase and further increase in temperature results in a phase of plasma called electrical plasma with free ions and electrons. But in the case of nuclear matter a phase transition occurs into a medium of deconfined quarks and gluons which is called Quark Gluon Plasma (QGP). This state of matter existed after the Big Bang for a few microseconds (μs). In relativistic heavy ion collision the conditions of the universe's early phase can be re-created upto some extent. A very dense medium with high temperature is formed by ultra-relativistic collisions of heavy ions. This highest energy can be achieved at Large Hadron Collider (LHC) at CERN, in collisions of heavy nuclei at high energy, forms a medium whose temperature is very high i.e. several times the critical temperature (T_c). The approximation of the temperature depends upon the hydrodynamic measurements and production of thermal photons exist for very brief time [4, 5]. In an accelerator for a very short interval of time the QGP could be created which composed free quarks and

gluons ($\approx$ 10 fm/c) [6] and again these quarks and gluons formed the hadrons before the temperature drops below T_c and finally in the experiments these hadrons are observed. From these final state hadrons we can extrapolate the properties of the QGP. QGP is transparent for the particles that do not strongly interact, (like electron, photons) etc.

1.1 The Standard Model

The universe is made up of fundamental particles that are twelve in numbers and their anti-particles according to the Standard Model (SM) and these fundamental particles are categorized into quarks and leptons. There are four force carriers or exchange particles called gauge bosons through which these quarks and leptons are bound together [7]. There are four known fundamental interactions according to the present theoretical understanding of physics. But SM includes only three interactions because gravity has negligible effect on the fundamental particles interactions. The relative strength of these four interactions along with their force carriers and ranges are given in Table (1.1).

Gauge boson	Interaction	Mass(GeV)	Strength	Range	Spin
Gluon	strong	0	1	10^{-15} m	1
γ	electromagnetic	0	10^{-2}	$1/r^2$	1
$W^{\pm}$, Z^0	weak	80.4, 91.2	10^{-5}	10^{-18}	1
graviton	gravity	0	10^{-39}	$1/r^2$	2

Table 1.1: *Gauge Bosons*

Because of strong interaction the nucleons are located inside the nucleus and quarks are confined inside nucleons. Similarly the interactions of color charges is also described by the QCD, whose range is limited to a couple of femto meter. It is the strongest interaction. Another interaction, which is experienced by us in our daily life is electromagnetism. The theory which describes the electromagnetic interaction is called the Quantum Electrodynamics (QED). The particles which are unstable, and thus for their decays the weak interaction is responsible, include e.g. free neutron nuclear beta (β) decay:

$$n \rightarrow p + \bar{e} + \bar{\nu_e} \tag{1.1}$$

The strength of weak interaction is smaller as compared to the electromagnetic interaction. It is because the mediators of weak interaction are heavy such as $W^{\pm}$ and Z bosons, whose masses are 80.4 GeV and 91.2 GeV respectively. The unified theory which describes the later two interactions is called Electroweak theory. Lepton and quark families experience weak interaction. It is the weak interaction due to which the quarks change their flavor. As there is no color charge associated with the leptons therefore they do not undergo strong interaction. Similarly there is no charge on the neutrinos therefore they

do not experience any electromagnetic force but they interact via weak interaction [8]. Moreover one of the weakest forces that has an infinite range is called gravity. This force is the most familiar force to us but the particle which mediates this force, called graviton, is not yet discovered experimentally. Among the individual particles the strength of this force is very small. That is why in experimental high energy particle physics we safely ignore it. Experimentally all the SM particles have been observed at LHC along with the recent discovery of Higgs boson [9, 10].

As mentioned earlier, there are two categories of fundamental particles. First category is called quarks which were independently proposed in 1964 [11] by theorists Zweig and Gell-Mann and they observed that hadrons consist of spin-1/2 elementary particles. They named these particles the "quarks" such as up, down and strange quarks. The Stanford Linear Accelerator Centre (SLAC) in 1974 [12] discovered new quark and this new fourth quark was given a name "charm". Finally Cabbibo, Kobayashi and Maskawa (CKM) extended the four quarks scheme to six quarks. These quarks and anti quarks along with their charges and masses are listed in Table (1.2). From the observed masses of hadrons the masses of quarks can be measured indirectly. We cannot obtain masses from the measurement of free quarks because free quarks do not exist beyond boundaries of hadrons.

Quark	Symbol	Charge	Antiparticle	Anticharge	Mass (MeV/c^2)	Generation
up	u	$+2/3$	$\bar{u}$	-2/3	1.7-3.3	1
down	d	-1/3	$\bar{d}$	$+1/3$	4.1-5.8	1
charm	c	$+2/3$	$\bar{c}$	-2/3	1270	2
strange	s	-1/3	$\bar{s}$	$+1/3$	101	2
top	t	$+2/3$	$\bar{t}$	-2/3	172000	3
bottom	b	-1/3	$\bar{b}$	$+1/3$	4190	3

Table 1.2: *Quarks, anti-Quarks along with their charges and masses*

In Table (1.2), six types or flavors of quarks (q) and anti - quarks ($\bar{q}$) are given. There are three generations of quarks (both quarks and anti quarks) based on the masses and stability. Further, due to color charge carried by quarks they also interact via strong force. Charged particles and their anti particles are different because of their electric charge, that is the particles carry charge while the anti particles carry anti charge, with all other properties being identical. The relationship between particle and anti particle plays an important role because to satisfy the conservation laws, without anti- particle a particle cannot be created from the vacuum. Neutral particles such as neutrinos, which are their own anti-particles, are called Majorana particles.

The other category of fundamental particles is called leptons. We have two main types of leptons: one type of leptons have electric charge such as electron, muon, tauon while the other type of leptons are neutral such as their associated neutrinos. Leptons are spin-

Lepton	Antiparticle	Charge	Mass (MeV)	Generation
e^-	e^+	$\pm$ 1	0.511	1
ν_{e^-}	$\bar{\nu}_{e^-}$	–	(0-0.13)$\times$ 10^{-6}	1
μ^-	μ^+	$\pm$ 1	105.7	2
ν_{μ^-}	$\bar{\nu}_{\mu^-}$	–	(0.009-0.13) $\times$ 10^{-6}	2
τ^-	τ^+	$\pm$ 1	1777	3
ν_{τ^-}	$\bar{\nu}_{\tau^-}$	–	(0.04-0.14) $\times$ 10^{-6}	3

Table 1.3: *Leptons*

1/2 particles like quarks. There are total six leptons which are in pairs forming three generations. The charged leptons interact weakly as well as electromagnetically while neutrino has no charge therefore it is affected only by weak force. The leptons along with their symbols, charges and masses are shown in Table (1.3).

Similarly the third category of particles is called the gauge bosons which are the mediators or force carriers of the four fundamental interactions. The gauge bosons obey Bose Einstein statistics and have integer spins (0, 1, 2 etc). The gauge boson for strong force is gluon, photon for the electromagnetic force, $W^{\pm}$, Z^0 for the weak force and graviton for the gravitational force. These gauge bosons were listed in the Table (1.1) along with interactions, strength, mass and range of these particles.

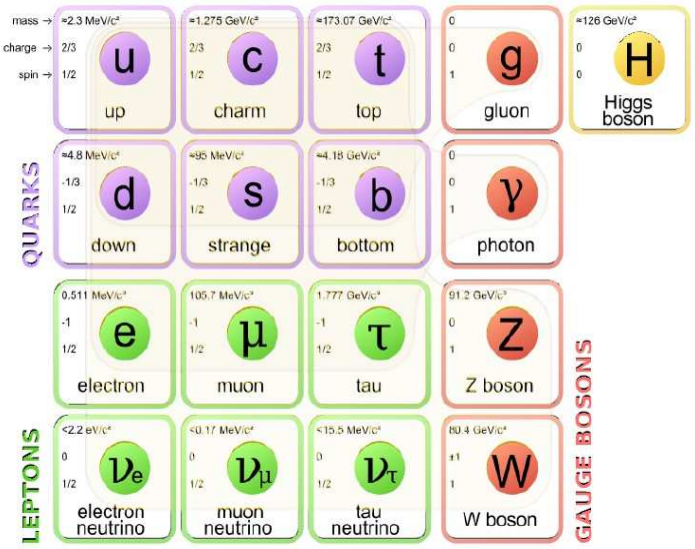

Figure 1.1: *The elementary particles in SM [13].*

In Fig. (1.1) an overview of fundamental particles is shown along with the properties of these particles.

1.2 Quantum Chromodynamics

We know that there are four fundamental interactions, and amongst these four fundamental interactions the strong interaction is the strongest which binds nucleons to form atomic nuclei. However these nucleons are further made up of quarks and it is also the strong force which is responsible for the binding of these quarks. QCD is like QED but the difference is that QED deals with electric charge only while in QCD we consider color charge as well. The gluons carry the color charge and interactions amongst themselves as well. The quark parton model of 1960s is the base for the theory of strong interactions. This model was established as a result of highly energetic particle accelerators which probe the internal structure of the nucleons by deep inelastic electron proton scattering [14]. According to Bjorken scaling the observed cross sections had shown that nucleons were not the elementary particles but composed of point-like particles called "partons" [15]. Gell Mann and Zweig, proposed independently the quark model at the same time [16, 17]. According to the quark model, fractional charges of quarks along with their anti-quarks made up all the composite particles such as mesons, which are made up of quark anti- quark ($q\bar{q}$) pair. Similarly the three quarks (qqq) bound state is called baryon and the anti-baryons come from anti-quarks ($\bar{q}\bar{q}\bar{q}$). For the observed combinations of charge, isospin and strangeness three flavours of quarks were needed. These three quarks flavours are up (u), down (d) and strange (s) quarks. For the validity of quark model, the strongest evidence was the discovery of Ω^-, which is formed by three strange quarks [18]. In addition to up, down and strange quarks it was discovered in 1960s that there exist other three flavours of quarks called charm (c), top (t) and bottom (b) quarks which have higher masses as compared to the first three quarks. In Table (1.4), the quantum numbers of quarks are summarised.

Flavour	Charge	Other
u	+2/3	Isospin = +1/2
d	-1/3	Isospin = -1/2
c	+2/3	Charm = +1
s	-1/3	Strangeness = -1
t	+2/3	Top = +1
b	-1/3	Bottom = -1

Table 1.4: *Quark flavours and their quantum numbers*

A problem was created with the discovery of Δ^{++} baryon because it contains three up quarks which have parallel spin according to the quark model. But according to the Pauli exclusion principle it is not possible, so Δ^{++} was inconsistent with the principle. By introducing an additional quantum number of color, the problem was solved. These colors are "red", "green" and "blue" for the quarks and "anti-red", "anti-green" and

"anti-blue" for the anti- quarks. Thus in nature, with such postulations, only "white" particles are observed such as meson made up quark and anti-quark (color and its anti-color) and similarly red, green and blue quarks form baryons.

1.2.1 Confinement

An important QCD property is the phenomenon of confinement, which means that quarks are bound inside hadrons. According to this fact we cannot observe free quarks and gluons because they cannot exist in isolated form [19]. As we already know, in QCD the exchange particles of the strong interactions are massless gluons which carry color charge. This is the main reason which leads to the phenomenon of confinement even when we pulled apart two quarks. To observe this phenomenon it is necessary to consider the QCD color field lines as a function of separation distance, which is shown in Fig. (1.2). QCD potential behaves like QED potential in case of very short distance i.e. much less than the size of hadron (1 fm) which has r^{-1} dependence as shown in Fig. (1.2a). When the distance becomes large, approaching the size of hadron, then the gluon self interaction pulls the gluon exchanges into "flux tube" between quarks as shown in Fig. (1.2b). In this case the field energy is approximately constant per unit length like in the case of stretched spring. Thus the mathematical form of strong potential has the form of V_s.

$$V_s = -\frac{4}{3}\frac{\alpha_s}{r} + kr \tag{1.2}$$

where "α_s" is the constant used for strong coupling, tension in the flux tube is represented by "k" in Eq. (1.2) and "r" is the quarks separation.

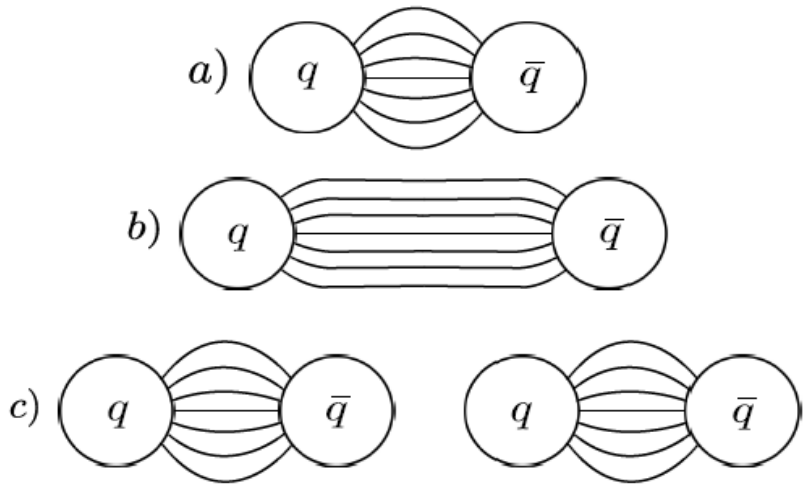

Figure 1.2: *The confinement of quarks in terms of QCD field lines [20].*

Whenever the separation between the quarks becomes greater than 1 fm, the energy

stored in the field of gluons increases such that a pair of $q\bar{q}$ is produced from the field energy. So in this way when the flux tubes breaks, two separate hadrons are produced which are individually confined. Thus whenever the two quarks are pulled apart then in these flux tubes or strings greater amount of energy is stored which becomes large enough to produce a pair of quark anti-quark. Most of the mass of a hadron also arise from confinement because mass of nucleons are of the order of 1 GeV but in case of bare quark the expected mass is of the order of 1 MeV.

1.2.2 Asymptotic freedom

One of the QCD distinctive property is called asymptotic freedom which states that at shorter distance the strength of strong force decreases but at larger distance the strength increases. We know that in nature there are different interactions which play an important role in dynamics. These interaction are characterised by their interactions strength. The strength of interactions is called coupling constant (α), e.g. for the electromagnetic interaction the coupling constant is called fine structure constant, i.e. $\alpha = e^2/4\pi\epsilon_0\hbar c \sim 1/137$. The strength of the strong interaction is denoted by α_s which is called strong coupling. In fact this is not constant but varies with length scale and has dependence on four - momentum transfer (Q). Due to quantum fluctuations this running coupling constant is a general phenomenon which creates vacuum as a polarized medium. The "screening" phenomenon of electric charge appears due to vacuum polarization in QED, which shows that at larger distances the effective charge appears weaker. However, on the other hand in QCD, the polarization phenomenon of anti-screening of charge (color) occurs due to the gluons self coupling. So at larger distances the effective charge appears stronger and at a shorter distances the effective charge becomes weaker. According to QCD, with vanishing coupling constant, the strong interactions becomes asymptotically free gauge theory. In other words, as Q $\rightarrow \infty$, α_{strong} (Q)$\rightarrow$ 0. This phenomenon is called asymptotic freedom and for the non - Abelian gauge theories this is unique [21]. As with separation the coupling increases so in QCD the absolute size of α_s is not predicted. Rather through the renormalization, its energy dependence can be determined precisely [22]. According to the Quantum Field Theory (QFT) the expression for the $\alpha_s(Q^2)$ where $Q^2 = -q^2$ is given by:

$$\alpha_s(Q^2) = \frac{\alpha_s(\mu^2)}{1 + \beta_0\alpha_s(\mu^2) log\frac{Q^2}{\mu^2}} \tag{1.3}$$

where $\beta_0 = \frac{1}{12\pi}(2n_q - 11n_c)$, $n_{q,c}$ show the number of quarks and colors. For QCD there are six flavors of quarks and three colors, so the value of β_0 = -$\frac{7}{12\pi}$. In terms of QCD scale constant it is expressed as: $\Lambda^2_{QCD} = \mu^2 exp[-1/\beta_0\alpha_s(\mu^2)]$. So by defining positive

quantity b $= -\beta_0$ the Eq. (1.3) can be simplified to

$$\alpha_s(Q^2) = \frac{1}{bln(Q^2/\Lambda_Q^2 CD)} \tag{1.4}$$

At small separation, when $Q^2 >> \Lambda_{QCD}$ the $\alpha_s << 1$, perturbatively the interactions can be treated, like in QED and this is the basis for pQCD and in calculating the cross section of hard (high Q^2) it plays an important role in QCD processes [23]. On the other hand the perturbative expansion is impossible for the low Q^2 as α_s becomes larger. In such cases another non-perturbative technique called lattice QCD is used. This technique formulates the QCD on the discrete spacetime lattice of finite size with gluons on the links and quarks on the sites [24]. To solve such a system numerically the MC techniques can be applied. In Fig. (1.3), the values of Q^2 ranges versus α_s are shown and from this

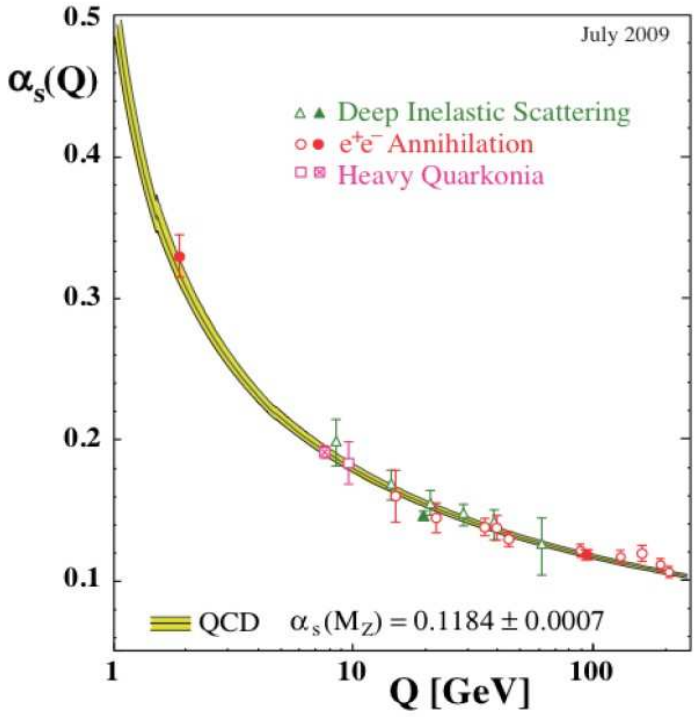

Figure 1.3: *The strong coupling (α_s) dependence on momentum Q transferred [25]*

measurement it has been determined that $\Lambda_{QCD} \sim 0.2$ GeV which is roughly equivalent to a distance of 1 fm. This is the main reason for hadrons size to be constrained to this scale.

1.3 Quark Gluon Plasma

One of the exotic states of matter: QGP is predicted by QCD [26, 27, 28, 29]. In 2001, in a press release CERN announced that they have found a new fourth state of matter in

the experiment of relativistic heavy ion collisions known as QGP. Quarks and gluons are deconfined at high energy densities. Just as at high energy the strong coupling constant decreases, according to QCD, at high energy density it is expected that a relativistic weakly interacting parton gas called QGP is formed by the quarks and gluons.
From the study of Big Bang Theory it is clear that the creation of universe is due to the explosion which was very hot and dense. The expansion of the universe after that is shown in Fig. (1.4).

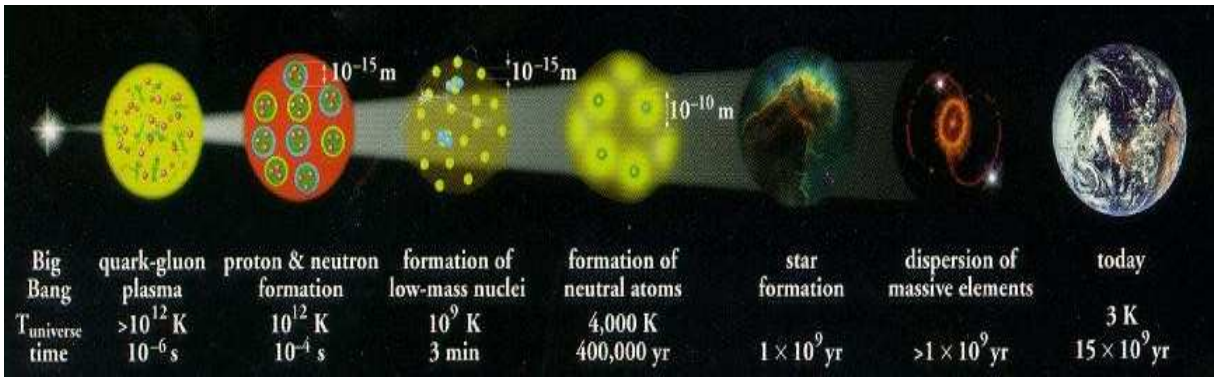

Figure 1.4: *A probable evolution of the universe [30]*

A few microsecond after the Big Bang i.e. in early stage of the universe it is believed that matter was in the form of quarks and gluons. When expansion of the universe occurred and the universe became cool and its temperature as well as pressure decreased, it allowed quarks to merge into hadrons (e.g. proton and neutrons). Similarly by further cooling of the universe the hadrons merged and formed the atoms and finally universe emerged in the present form.
We know that at present one of the important topics in high energy physics (HEP) is the study of QGP, since it gives important information about an early stage of the universe. In sufficiently hot and dense system, it is expected that QGP can be created [31, 32]. Heavy ion collisions provide us a way to produce QGP in the lab for a time around 10^{-23} s.

1.4 Signatures of Quark Gluon Plasma

One of the main aim of many highly energetic collisions experiments is to prove the existence of QGP. But it is not possible to observe QGP directly within its small lifetime. However for QGP the detection of various particles might prove to be useful as signatures and plasma diagnostic tools. It is recognized that for the identification of QGP there may be no unique signals but there are a number of different indirect signals that come out from the QGP medium which may be treated as QGP signatures. Some of these probes and QGP signatures are described below.

1.4.1 Strangeness enhancement

One of the signature which shows the existence of QGP is strangeness enhancement. As compared to ordinary u and d quarks, a large amount of energy is required for the production of strange (s) quarks. For the $s\bar{s}$ production the high energy densities in QGP are conducive. Therefore as compared to the strangeness production in proton-proton (pp) collision the enhancement of strange particles occurs in the QGP medium. As compared to hadron gas the production of strange quarks in QGP is energetically easier. Moreover only in weak decays strangeness can disappear, so strange hadrons can survive hadronization time scale because as compared to hadronization the weak decay is a longer process. Therefore it is considered that strangeness enhancement is one of the signatures of the QGP. At Super Proton Synchrotron (SPS) experiments such an effect was observed [33, 34, 35]. As compared to the production of all non strange particles the production yield of strange quarks is higher in nucleus-nucleus (AA) interaction than in hadron-nucleus (pA) or hadron-hadron (pp) collision. Similarly it was expected that the QGP transition temperature is 170 MeV which is similar in magnitude to that of strange quark mass. So through scattering subprocess many strange quarks are produced. The $gg \rightarrow s\bar{s}$ is the dominant subprocess at SPS energies [36].

1.4.2 Charmonium suppression

Charmonium states (e.g. J/ψ) which can form by the charm quark pairs ($c\bar{c}$) are produced at the initial stage of the collision. If QGP is formed then in the medium the open color charges prevent c and $\bar{c}$ quarks from binding to J/ψ because the open charge can screen the color charge potential. If J/ψ, is placed in a thermal medium the interaction between c and $\bar{c}$ may weaken due to the Debye screening, the illustration of J/ψ suppression is given in Fig. (1.5). Similarly the potential between c and $\bar{c}$ may alter considerably because of the quarks and gluons around bounded $c\bar{c}$. For the first time Matsui and Satz [37] suggested that these two effects may lead to J/ψ dissociation resulting in its suppression. Therefore after the collision when the QGP appears $c\bar{c}$ production is suppressed. At SPS, Relativistic Heavy Ion Collider (RHIC) and Large Hadron Collider (LHC) experiments this effect was observed [38, 39, 40, 41]. Similarly the high mass of the charm quarks suggests that, the production of $c\bar{c}$ occurs in the heavy ion collisions at very early stage. At sufficiently high temperature in a medium relatively large size of $c\bar{c}$ bound states (i.e. J/ψ), the Debye screening radius $r_D(T)$ becomes smaller. Therefore it is observed that the production of these states gets suppressed while due to the availability of free charm quark the production of $D^{\pm}$ and D^0 states is enhanced [42].

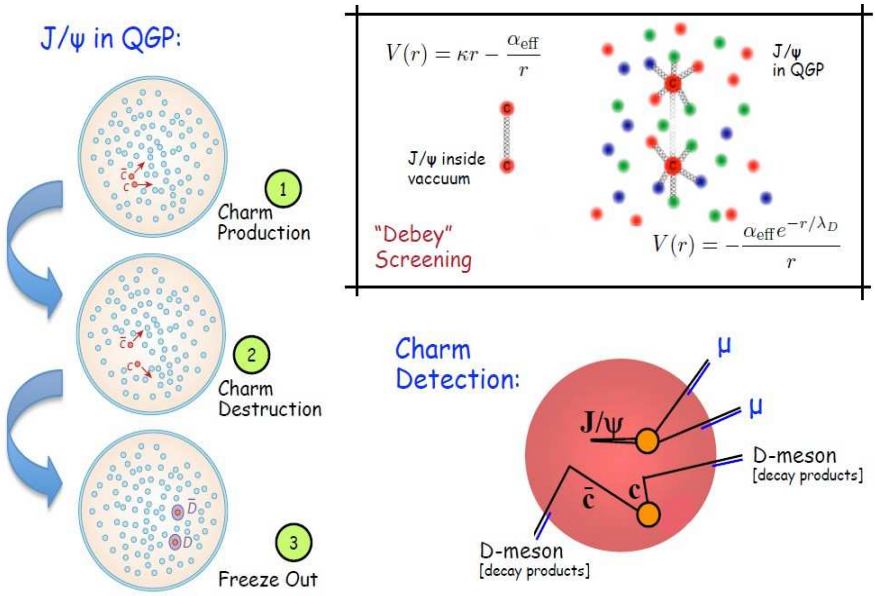

Figure 1.5: *J/Ψ suppression due to Debye screening effect [43]*

1.4.3 Dileptons production

Di-leptons production gives us important information about the thermodynamical state of QGP. Dileptons are produced in the initial quark-antiquark annihilation. The dileptons are also produced in subsequently produced hadronic medium e.g. $\pi^+\pi^- \rightarrow \ell^+\ell^-$ or ρ, ω or J/ψ decay. The high energy lepton pairs, some of the most prominent observables in particular (e^+e^- and $\mu^+\mu^-$). Besides QGP and hadronic medium for dilepton production there are other sources also, such as the Drell-Yan processes, produce a virtual photon via quark and sea quark annihilation. Then virtual photon decays into lepton pairs, ($q\bar{q} \rightarrow \gamma^* \rightarrow \ell^+\ell^-$). However as compared to the Drell-Yan processes the hadronic phase production gains importance because large number of dileptons are produced from the hadronic decays which depends on the collider energies. As we know that leptons have electromagnetic charge so they only interact electromagnetically, therefore such leptons without any interaction reach the detectors. Therefore the distribution of dileptons momentum give us an important information about the produced medium in heavy ion collisions (HIC).

1.4.4 Electromagnetic probe

Similar to the production of dileptons the photons(γ) are produced via quark(q) antiquark($\bar{q}$) annihilation. For photon production the processes, $q\bar{q} \rightarrow \gamma\gamma$(QED, $\mathcal{O}(\alpha_e^2)$) and $q\bar{q} \rightarrow \gamma g$(QED-QCD, $\mathcal{O}(\alpha_e\alpha_s)$) can be treated as the dominant channels. However, for the QED to QED-QCD channel, the probability ratio is about 0.02 [44]. So the contribution due to QED process, can be safely neglected. Similarly from Compton like

processes the photons can also be emitted i.e. $(gq(\bar{q}) \rightarrow \gamma q(\bar{q}))$. Depending upon the production mechanism in heavy ion collision, there are different types of photons: i.e. first ones are produced in pre-equilibrium phase are the prompt photons while second ones are called thermal photons. During QGP phase, mixed phase and hadrons gas phase, thermal photons are produced via scattering of quarks and gluons and final product of electromagnetic decay of hadrons are decay photons. After the collision, the majority of the photons produced are the decay photons. Therefore direct photons (prompt and thermal) observations is not a trivial problem. However one can eventually estimate the temperature of the early stage of the QGP by subtracting the huge background signal coming from decay photons. In short, similar to the dileptons the photon momentum distribution can yield a very important information about the quarks and gluons momentum distribution which make up the plasma produced in the collisions process. In this way it opens a window for the study of produced medium thermodynamical properties. Direct photon studies are performed at SPS, RHIC and LHC [45, 46, 47].

1.4.5 Jet quenching

For QGP studies one of the interesting experimental signature is jet quenching in which the high (p_T) particles are suppressed due to the energy loss inside the medium [48]. As compared to pp collision the results from the AA collision show a clear evidence for the jet quenching effects at LHC [49, 50, 51] and RHIC [52, 53, 54, 55] through the inclusive high (p_T) hadrons production and modification of high (p_T) dihadron angular correlations. At high energy, a group of particles which is direction correlated or the spray of hadrons is called jets. These jets are formed due to the partons fragmentation which escape from

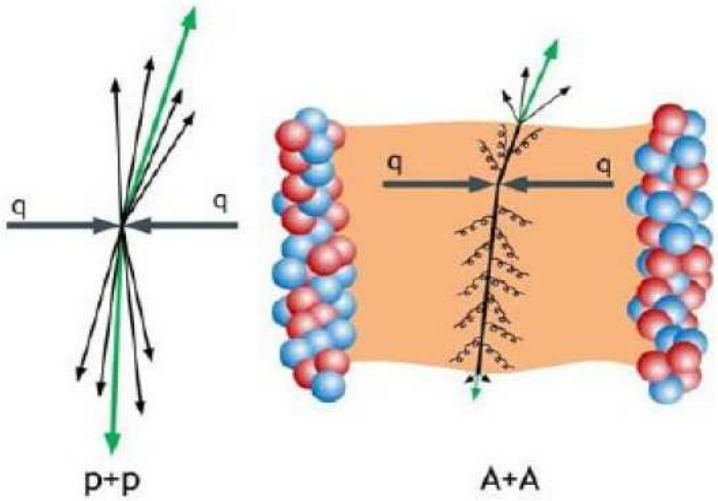

Figure 1.6: *Jet quenching phenomenon. A comparison of di-jet production is shown in the QCD vacuum (left) during pp collision and hot and dense medium (right) in heavy ion collision [56]*

the collision region. As we know that in the hard processes these partons are produced, (transfer maximum momentum) so the jets have high transverse momentum. Amongst the jets, dijets is a specific type of jets which move in the opposite direction in pairs as shown in Fig. (1.6).

If jet is produced near the surface of QGP then one jet which is at near side will be normally propagated while the other side jet will be smeared. The reason behind smearing jets is that the other side jets are produced as a result of those partons fragments which travel through hot and dense medium. The momentum of those partons will be lowered because jets lose energy due to their interactions with the partons of the produced medium, a phenomenon termed as jet quenching. An interesting consequence of jet

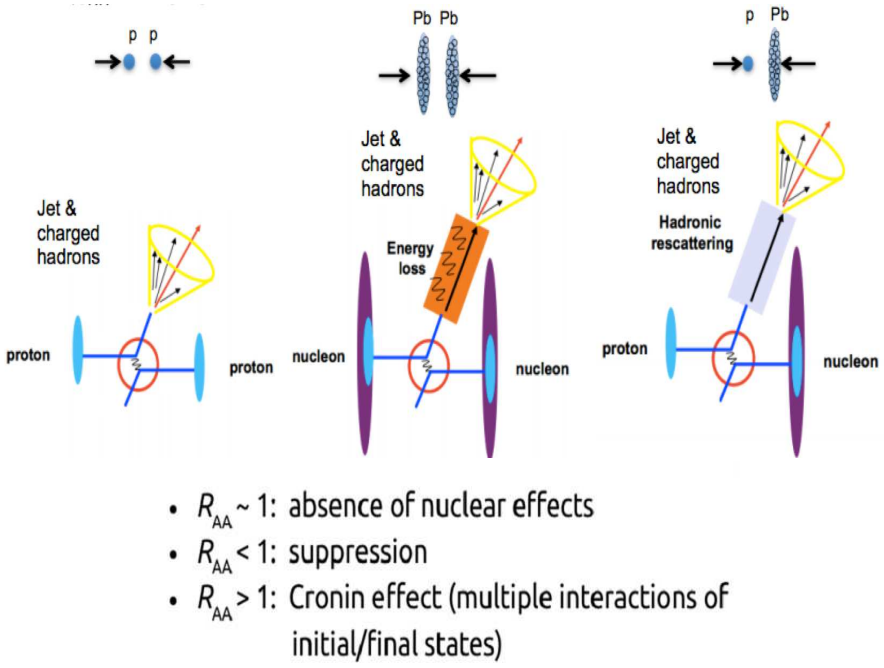

Figure 1.7: *Medium effects in pp, p-Pb and Pb-Pb collisions [57]*

quenching is the energy spectrum modification of jets and in turn the charged particles due to the energy loss inside the QGP medium. The quantified spectrum of modified charged particles is obtained by comparing the charged particle spectrum in AA collision to that of pp collisions, which is also referred as spectrum baseline of produced particles. It can be expressed in terms of Nuclear Modification Factor, R_{AA}:

$$R_{AA}(p_T) = \frac{d^2N_{ch}^{AA}/dp_T d\eta}{< T_{AA} > d^2\sigma_{ch}^{NN}/dp_T d\eta} \tag{1.5}$$

In Eq. (1.5), N_{ch}^{AA} is the charged particle yield in AA collision while the σ_{ch}^{NN} represents cross section of nucleon- nucleon (NN) collision. $< T_{AA} >$ is called the nuclear overlap factor. While using the Glauber model we can calculate this factor and it is the effective

overlap area in which one nucleon A interacts with another nucleon A. To provide a proper normalization in AA collision a scaling factor, nuclear overlap factor $< T_{AA} >$ is used to compare the high-p_T charged particles produced in AA to that produced in NN collision. The nuclear overlap factor can be formulated by $< T_{AA} >=< N_{coll} > /\sigma_{inel}^{NN}$. The σ_{inel}^{NN} is the inelastic nucleon collision cross section [58]. In the absence of nuclear effects the ratio of R_{AA} will be unity i.e. $R_{AA} \sim 1$, while in case of medium effects this ratio will be less than unity i.e. $R_{AA} < 1$ and similarly if the ratio is greater than unity i.e. $R_{AA} > 1$ then it shows that there is enhancement of low p_T charged particles which is called Cronin effect. Sketches of these three effects are shown in Fig. (1.7).

1.4.6 Hydrodynamics flow

In heavy ion collisions for the study of the QGP properties in detail the measurement of collective expansion is very important for the created matter. The heavy ions are the extended objects with the systems created in a head on collision and in peripheral collision being different. Schematically geometry of the collision between two nuclei is

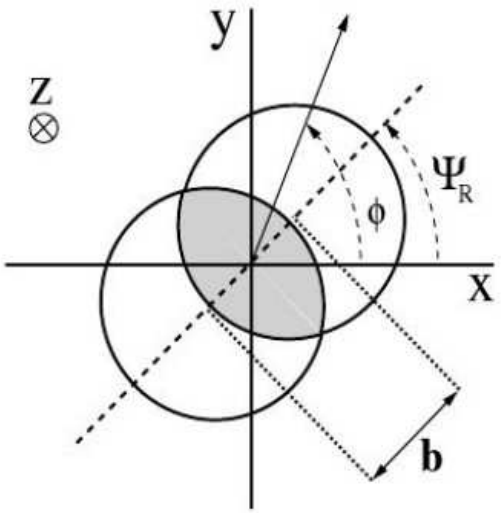

Figure 1.8: *Schematic view of the collision geometry as seen in the plane transverse to the beam direction (z-axis)[59].*

represented in Fig. (1.8). The perpendicular separation between the projectile and target centers is termed as "impact parameter" and is represented by "b". For small "b" the collision is said to be most central collision and the created system's spatial distribution is approximately azimuthally symmetric. As a result a symmetric expansion will be produced which is called the radial flow. However an initially asymmetric overlap region is created when the heavy ion collision is non central, which gives rise to anisotropic flow. If there is large number of rescattering of the produced particles during the collision in

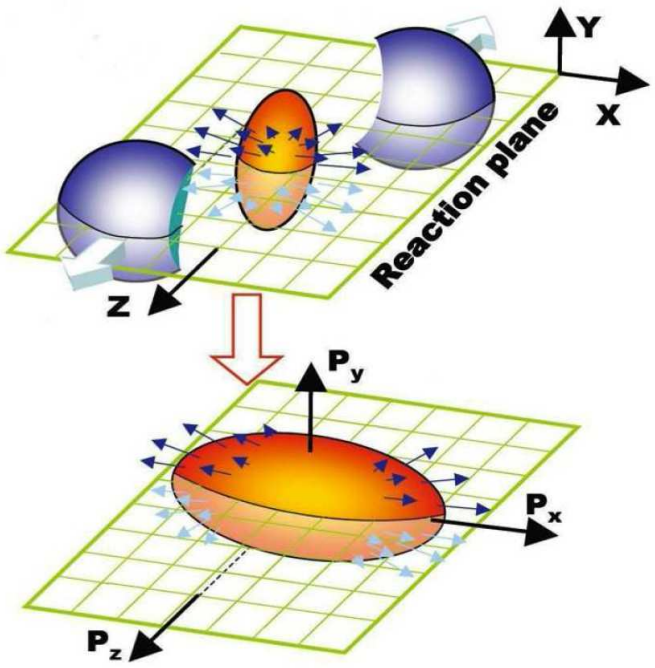

Figure 1.9: *Initial anisotropy transformation into a momentum space anisotropy in non central heavy ion collision [60].*

the overlap region then with respect to the reaction plane (Ψ), the produced particle's spatial anisotropy is converted into the momentum anisotropy as demonstrated in Fig. (1.9). At perpendicular axis the pressure gradient is lower while it is maximum towards the x-axis, therefore, maximum number of particles with higher velocities (so with higher momentum) are produced in shorter direction i.e. along x - direction. Therefore as a result of the heavy ion non central collisions, particles momentum distribution is azimuthally asymmetric. This type of flow is called elliptic flow. Axis of the beam and "b" form a plane which is termed as reaction plane. Anisotropic flow measurements, give us useful information about the QGP properties. In non central collisions the anisotropy in the initial shape of the fireball in the presence of strongly interacting matter is converted into an azimuthal dependence of the final state particles momentum distribution. The azimuthal anisotropy with respect to the reaction plane of the particles produced can be quantified by studying the Fourier expansion of the azimuthal angle distribution [61] given by Eq. (1.6).

$$E\frac{d^3N}{d^3p} = \frac{1}{2\pi}\frac{d^2N}{p_T dp_T dy}(1 + \sum_{n=1}^{\infty} 2v_n cos[n(\phi - \Psi_R)]) \tag{1.6}$$

where ϕ is the particle azimuthal angle, Ψ_R is the reaction plane angle and the n^{th} harmonic coefficient is v_n. v_1 is the first harmonic coefficient and is called directed flow while

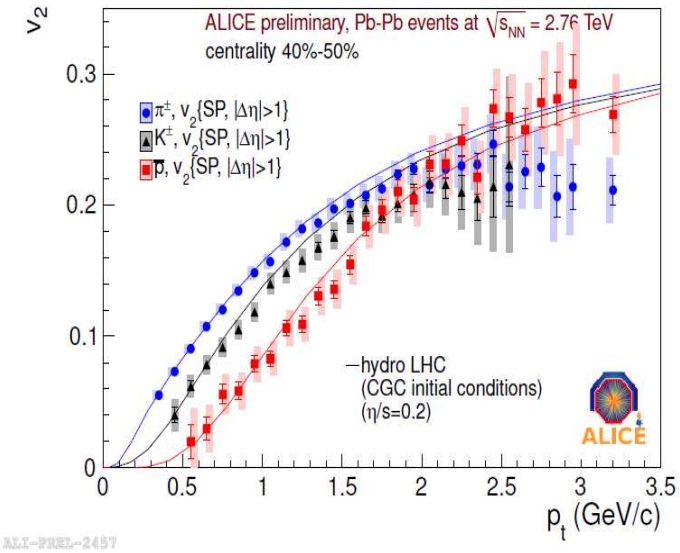

Figure 1.10: *Elliptic flow v_2 in the $40\% - 50\%$ vs p_T at ALICE [65]*

the second harmonic coefficient, v_2, is called elliptic flow and similarly v_3 is triangular flow and so on. Assuming a QGP equation of state with quarks degree of freedom the measurements of v_2 are compared with predictions from relativistic hydrodynamics. The elliptic flow v_2 as a function of p_T for the $40\% - 50\%$ centrality is plotted in Fig. (1.10) [65].

At RHIC [62] and at LHC [63, 64] for lower momentum particles, the data is well described by these predictions. Thus for the production of QGP it gives strong evidence. These models were successful in the description of the QGP as a "perfect liquid" with very small viscosity.

1.5 Phase diagram of QCD

A phase transition into a deconfined quarks and gluons plasma from hadrons was first suggested by T. D. Lee in 1974 [66]. Edward Shuryak in 1978 introduced the name of Quark Gluon Plasma with the realisation that thermal fluctuations of gauge fields can lead to color screening [67]. This screening effect is similar to the mobile charges in an electromagnetic plasma. It was suggested that a particle and energy dense environment could be produced in heavy ion collisions where the screening effects melt hadrons and form QGP [68]. This creates a phenomenon of deconfinement where quarks and gluons become free.

A phase transition is expected to occur when one phase changes to another and one can obtain another state by changing the temperature and baryon chemical potential of strongly interacting matter. The baryon chemical potential is represented by μ_B which is

Gibbs energy required to add or remove one baryon from the system at fixed pressure and temperature. The baryon chemical potential is approximately equal to the mass of the nucleon $\mu_B \approx \mu_N = 940$ MeV. Phase diagram in Fig. (1.11) shows two phases i.e. hadron gas phase and partonic phase. At low T, and μ_B, $\mu_B \sim 1$ GeV, there will be ordinary hadronic matter while the system shows that between hadronic matter and QGP, a first order transition occurs at sufficiently high values of baryon chemical potential [69]. At $\mu_B \neq 0$, the lattice QCD calculations [70] suggest that there is a critical point ($\mu_{B,c}$ T_B) existence such that for $\mu_B < \mu_{B,c}$, the transition is no longer first order.

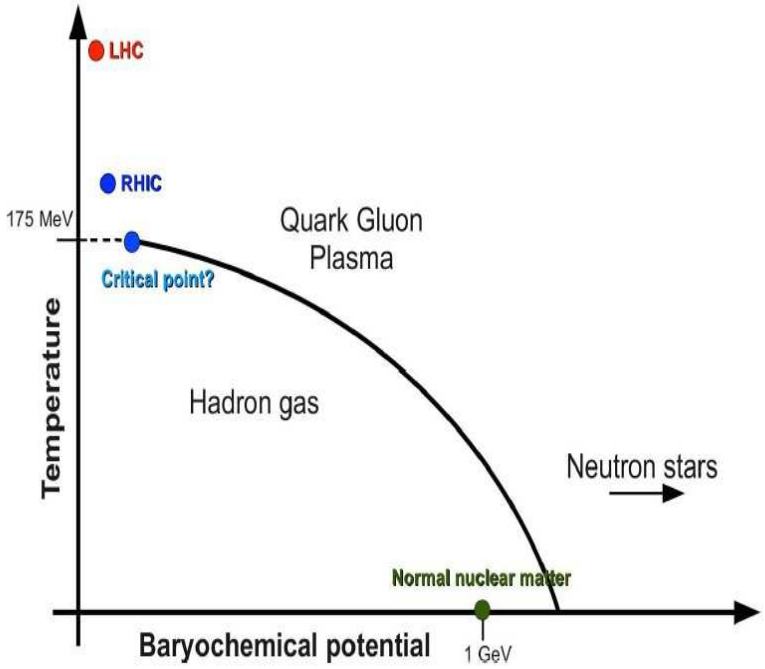

Figure 1.11: *Schematic phase diagram of nuclear matter as a function of temperature and baryon chemical potential [73].*

According to the recent calculations [71], at low value of baryo-chemical potential the transition is simply a rapid crossover that occurs in a small, well defined temperature intervals. In the early universe during a rapid expansion and cooling the transition from QGP to hadronic matter occurred at high temperature and vanishing baryo chemical potential. The QGP state is expected, in the neutron star, where due to the gravitational collapse, the temperature is low but baryo chemical potential is very high. Nowadays with high energy accelerators, like RHIC, and LHC the region of low μ_B, and high temperature (T), is investigated. In the context of astrophysical studies [72] the high μ_B and $T \sim 0$ regime is indirectly investigated. Similarly different relevant experiments scan the phase diagram by changing the collision system and collision energies.

1.6 Heavy Ion Collisions

In relativistic heavy ion collisions nuclear matter of extreme density and temperature can be created in which within a small volume a large amount of energy can be concentrated for a very short period of time. At LHC in Pb-Pb central collisions, approximately 1900 nucleon - nucleon collision [74] take place within central region [75]. In heavy ion collisions a good perspective of the created system evolution is necessary for the study of QGP properties. In the collision of two nuclei the evolution of the system created can be divided into different phases as shown in Fig. (1.12).

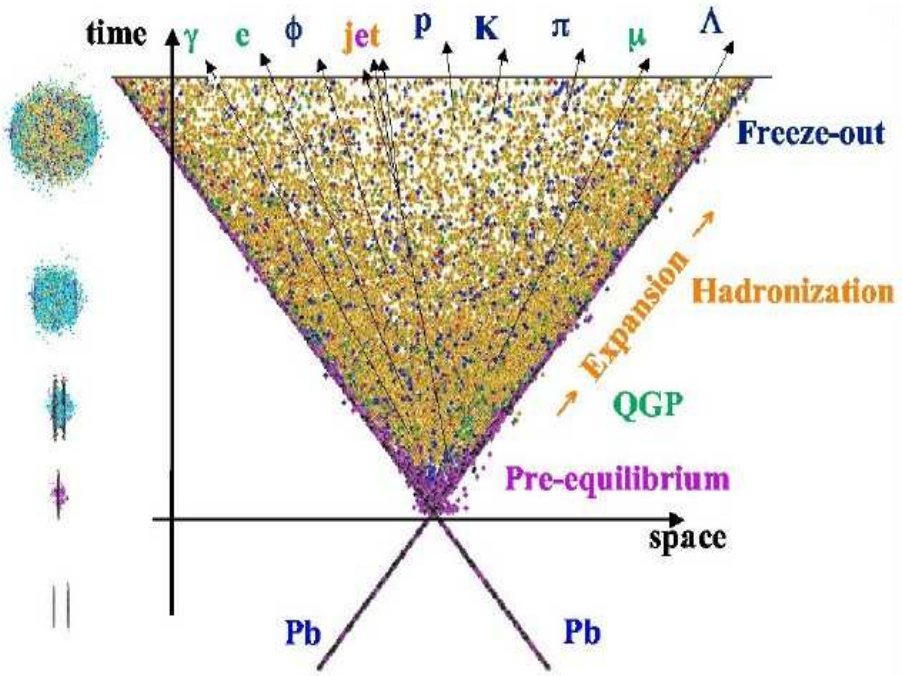

Figure 1.12: *Space - time evolution according to the Bjorken's hydrodynamic model [76]*

- **Pre - equilibrium**($\tau < \tau_{th}$)$\longrightarrow$ During the parton scattering hard processes occur leading to the creation of high-p_T probe, like heavy quarks, jets, direct photons etc.
- **Thermalization and QGP phase**($\tau_{th} \sim 1$ fm/c)$\longrightarrow$ In case of multiple scattering amongst the constituents of the system created after a certain time, τ_{th} leads to the thermal equilibrium. If the energy density is high enough ($\varepsilon_c \sim 1GeV/fm^3$), and as compared to the system size the mean free path is expected to be small then hydrodynamically the thermalized QGP will expand and cool down due to the expansion of the system.
- **Hadronization**$\longrightarrow$ Due to expanding medium the temperature decreases and a transition takes place. When temperature of the system is below the critical temperature T_c the quarks and gluons are again confined into ordinary hadrons. As

the inelastic interactions take place, so the system can still be in local thermal equilibrium.

- **Chemical freeze-out**$\longrightarrow$ When there is further expansion of the system and temperature drops, the inelastic processes among the hadrons cease. The hadrons abundances are fixed at this stage. It means that at this stage no new particles will be produced.
- **Kinetic freeze-out** $\longrightarrow$ At this stage due to the elastic collision ceasing, the momentum spectra of the produced particles are fixed.

In heavy ion collisions, to study different characteristics of the produced system, it is important and also necessary to determine its parameters such as chemical potential, flow velocity, temperature and equation of state. From a wide variety of experimentally accessible observables the relevant parameters can be inferred. To characterize the various collision stages these parameters can help to disentangle the different physical mechanisms. This is demonstrated in Fig. (1.12), where different particles are shown in different colors format and are also used to display the collision stages from which they carry information.

1.7 Kinematic variables

In order to better understand the particle collision at ultra relativistic energy it is necessary to define certain variables. Therefore in relation to the beam axis and laboratory frame it is convenient to use kinematic variables. For the ALICE experiments the coordinates system used is such that the z-axis is the direction of beam of particles, the x-axis is horizontal, and y-axis is vertical pointing up. The region where the beams cross and collision occurs is roughly the point (0, 0, 0). Exactly at the interaction point the collisions do not always happen. They are rarely displaced from the interaction point in x and y direction more than 0.1 mm, but on the z-axis displacements of more than 10 cm are not uncommon. Some of the key variables used in this work are presented here.

1.7.1 Collision Energy

Collision energy in the centre of mass (c.m) frame is the total energy available from a particle collision. The energy can be measured by four momentum vector, $p^{\mu} = (E, -p)$, where E represents the particle energy and p is particle three momentum. In the system of colliding particles four-momentum is a conserved quantity. The c.m. energy of the system having the same energy and mass but three momentum is opposite ($p_1 = (E, p)$ and $p_2 = (E, -p)$) can be calculated by taking the total four-momentum squaring of the

two colliding particles.

$$\begin{aligned} p^{\mu}p_{\mu} &= (p_1 + p_2)^2 && (1.7)\\ &= p_1^2 + p_2^2 + 2p_1p_2 && (1.8)\\ &= (E^2 + |p|^2) + (E^2 + |p|^2) + 2(E^2 - |p|^2) && (1.9)\\ &= 4E^2 = E_{cm}^2 \equiv s && (1.10) \end{aligned}$$

so that the c.m. energy is $E_{cm} = \sqrt{s}$. From the above Eq. (1.10), it is clear that the c.m. energy in this type of collision is given by, $\sqrt{s} = 2E$ which is twice the beam energy. To define the centre of mass energy the use of $\sqrt{s}$ is standard in pp collision but different in heavy ion collision. Typically one can use $\sqrt{s}_{NN}$ where NN denotes the energy per colliding nucleon pair. By colliding different types of ions this makes it convenient to compare energy scales across the experiments.

1.7.2 Transverse Momentum

Momenta are mainly split into two components that is transverse momentum (p_T) component which is perpendicular to the beam direction while longitudinal momentum component, which is denoted by p_z, and is along the direction of beam. The transverse momentum components is defined as:

$$p_T = \sqrt{p_x^2 + p_y^2} \tag{1.11}$$

We are interested in p_T because it is a Lorentz invariant quantity. One of the main feature of p_T is that it is always related with physics that is involved in particle interactions, while calculating p_z is very difficult because in this direction the particles of the beam could have some left over momentum. As compared to longitudinal momentum, p_T gives relatively a clean sample of interesting physics due to particle interactions. We are interested in transverse momentum because to study QGP one needs high momentum particles which could be produced in hard interactions. This is possible when we study particles in the transverse direction.

1.7.3 Rapidity

Rapidity "y" is useful variable in high energy physics which is defined as:

$$y = \frac{1}{2}\ln\frac{E + p_z}{E - p_z} \tag{1.12}$$

Rapidity represents the particles movement along the beam direction and it is dimensionless quantity. Positive "y", represents the motion of the particles along forward direction while for negative "y" it represents the particles movement in the backward direction. The definition of rapidity is similar to the magnitude of the velocity but under a Lorentz boost rapidity is additive, which is not for the case of velocity. The general shape of the rapidity distributions remains unchanged in collisions while going to the laboratory frame from the c.m frame [77], which makes rapidity very useful for studying particle production. Energy of the particle is necessary to compute the rapidity which in a detector system sometimes can be measured directly. Indirectly it can also be calculated by identifying the particle mass and momentum and using the relativistic energy-momentum relations given by:

$$E = \sqrt{m^2 + p^2} \tag{1.13}$$

1.7.4 Pseudorapidity

The rapidity has problem that for relativistic particles it is hard to measure. To calculate the rapidity we need both the total-momentum and energy. It is often difficult to get total momentum of the particles due to the detector limitations. One can make the assumption in such a case that when a particle is moving close to the speed of light, i.e. moving with ultra relativistic speed, the momentum of the particle is larger than the mass of the particle, $p \gg m$ and the particle energy is simply given by its momentum:

$$y \approx \frac{1}{2}\ln\frac{p + p_z}{p - p_z} = \frac{1}{2}\ln(\frac{1 + \cos\theta}{1 - \cos\theta}) = -ln[tan\frac{\theta}{2}] \equiv \eta \tag{1.14}$$

where "η" is the pseudorapidity and "θ" is the emission angle also called the polar angle of the particle with respect to the beam axis. Therefore advantage of the pseudorapidity

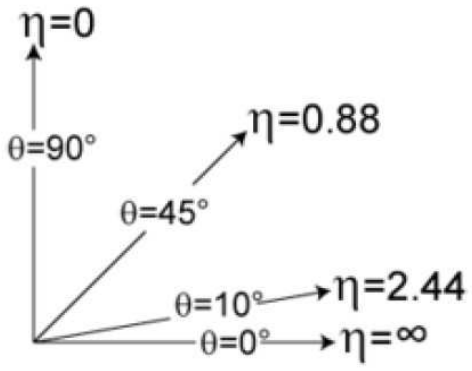

Figure 1.13: *Different emission angle corresponds to different pseudorapidity values where $\theta = 0^0 \rightarrow \eta = \infty$ is along the beam direction and $\theta = 90^0 \rightarrow \eta = 0$ is perpendicular to the beam direction [78]*

is that it has angular dependence which does not require the energy and momentum of

the particle. For ultra-relativistic particles the pseudorapidity is a good approximation of rapidity. Thus the pseudorapidity and rapidity are identical, $\eta \approx y$. For different polar angles the pseudorapidity is shown in Fig. (1.13).

1.8 Motivation and main goal of the present work

As we have mentioned in Sec. 1.3, one of the main subject of the modern HEP is to study the QGP. It has been mentioned that QGP is a phase of strongly interacting matter under extreme temperature and densities (see Sec. 1.5). It is believed that this state of matter existed for microseconds after the Big Bang. That is why study of QGP could gives us information about the early universe. To get QGP phase, interaction of heavy ions is performed at Ultra-relativistic energies (see Sec. 1.6). For more than 40 years, starting from BEVALAC, AGS, SPS, upto RHIC and LHC, physicists tried to get some clean information about this state of QGP. The problem gets difficult (see Sec. 1.4), because strongly interacting QGP matter is an invisible entity due to color confinement. As stated before, in the identification of quark gluon plasma there may be no unique signals, rather a number of different signals that come out from the QGP medium may be treated as QGP signatures such as: Dileptons production, thermal radiations, strangeness enhancement, J/ψ suppression, elliptic flow and jet quenching.

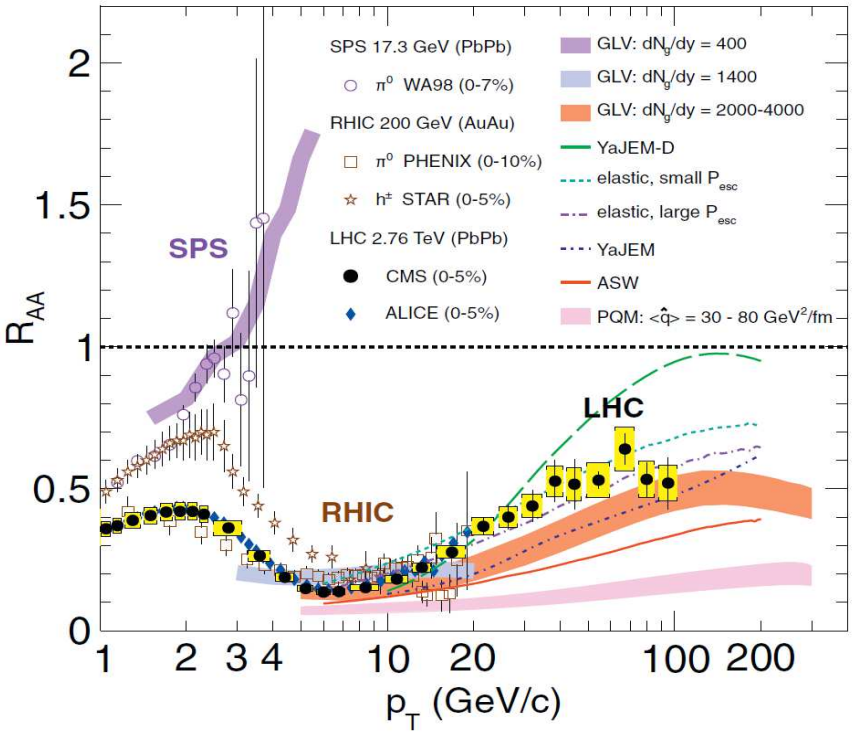

Figure 1.14: *Nuclear Modification Factor (NMF) at SPS, RHIC and LHC energies [79].*

Nuclear Modification Factor (NMF), shows how the characteristics of observables change

when we pass from pp collisions to AA collisions or pA collisions. Description of the behaviour of R_{AA} function is very difficult and alot of theoretical models were used to describe this behaviour. As we can see from Fig. (1.14), different models give different behaviour in various p_T regions. It means that the nature of the behavior is very difficult and to understand this it is necessary to use different codes. That is why in the thesis we have used different MC simulation. NMF has some structure, e.g. in Fig. (1.14), the behaviour of R_{AA} as a function of p_T is shown for the LHC, RHIC and SPS, energies. It is very difficult task to extract information on QGP from Fig.(1.14) and some additional information is necessary. We expect that this information could be obtained from the behaviour of the NMF in p-Pb collisions because the probability of QGP formation in this reaction is small. That is why R_{pPb} can give additional information to identify the behaviour of the NMF. The pp collisions have been used to create NMF. That is why the pp collisions study is also necessary. So the study of p-Pb and pp interactions at LHC energies is carried out. The aim of this work is to study the inclusive characteristics of the protons, anti-protons, K^+, K^-, π^+ and π^- mesons produced in the p-Pb collisions at LHC energies using simulated data coming from different codes (see Sec. 3.1, 3.2, 3.4, 3.5, 3.6, 3.7, 3.8) and compare the obtained spectra with the experimental ones (see Chap. 4 and 5). In order to calculate nuclear effects in p+Pb collisions, the p_T differential yield relative to the pp reference, the nuclear modification factor, R_{pPb}, is calculated as:

$$R_{pPb}(p_T) = \frac{d^2N_{ch}^{pPb}/dp_T dy}{< T_{pPb} > d^2\sigma_{ch}^{pp}/dp_T dy} \tag{1.15}$$

where $d^2N_{ch}^{pPb}$ shows the differential yield for p+Pb collisions, $d^2\sigma_{ch}^{pp}$ shows the differential cross section for pp collisions and $< T_{pPb} >$ is the nuclear overlap function for p+Pb collisions. For minimum bias (NSD) p+Pb collisions, the average nuclear overlap function $< T_{pPb} >$ is $0.0983 \pm 0.0035\ mb^{-1}$. In absence of nuclear effects the R_{pPb} is expected to be one.

Chapter 2

The ALICE Experiment at LHC

In this chapter we will briefly describe the LHC and A Large Ion Collider Experiment (ALICE) detectors at CERN. The layout as well as subsystems of the ALICE detectors will be introduced.

2.1 The Large Hadron Collider

LHC is the largest and highest beam energy particle accelerator and collider in the human history [80-83] which is 26.7 km in circumference located at CERN, Geneva. There are eight arcs at LHC intercepted by eight sections where in the four sections inside the experiment the two particles beams crosses. LHC interest came as a result of the collisions of heavy ions at high energies and so the reason behind the physics program for studying pp, p-Pb and Pb-Pb interactions, LHC was designed. Beside heavy ion collisions, the lighter ions can also be operated in the LHC, e.g. Argon etc. At LHC the design beam energy and luminosity for protons are 7 TeV and $\pounds_{pp} = 10^{34}\ cm^{-2}s^{-1}$ respectively. As compared to the $p\bar{p}$ collider, Tevatron at Fermilab a factor of 7 times higher beam energy and a factor of 60 times greater luminosity was used at LHC. In the heavy ion (Pb-Pb) mode the energy and luminosity of $\sqrt{s} = 5.52$ TeV, and $\pounds_{Pb-Pb} = 10^{27}\ cm^{-2}s^{-1}$ respectively per colliding nucleon pair are used. This energy at LHC is 30 times higher as compared to the energy at RHIC at BNL. Superconducting dipole of maximum magnetic field 8.33 Tesla are used. For bending the beams of particles and focusing these beams 1232 superconducting dipole magnets and 392 lattice quadrupoles are installed. In total, at LHC in the main ring there are over 9000 magnets used.

The main reason to design LHC for pp collision is its high luminosity in contrast to Tevatron, SPS and other hadron colliders that were used before. Only one accelerator ring is needed in LHC for particle anti-particle collider. Earlier, to collide two particle beams having the same charges were required opposite magnetic fields as well as two separate rings. For example in RHIC two rings are used which are completely independent, whereas

Figure 2.1: *View of the LHC tunnel [84]*

at LHC only one magnet is used for bending the two beams of particles as shown in Fig. (2.1). A detailed sketch of the CERN accelerator complex is shown in Fig. (2.2). For the two ion sources (hydrogen and heavy nuclei) the creation of ions is the starting step of LHC accelerator chain. To extract the ions the electrostatics field are used. To split the continuous proton/ions beams in bunches the Radio Frequency Quardrupole (RFQ) are used. To increase the energy of the particles first the bunches enter the two Linear Accelerators (LINAC) i.e. LINAC2 (proton) and LINAC3 (lead) where the energy of the particles is increased upto 50 MeV in the case of protons and upto 4.2 MeV for lead by the drift tubes and AC voltage. Low Energy Ion Ring (LEIR) at LINAC1 accelerates the Pb ions up to 72.2 MeV/u energy from where it transfers into the Proton Synchrotron Booster (PSB) where the energy of the lead ions reaches 94 MeV/u. Similarly in PSB the protons are injected directly where the energy becomes 1.4 GeV. Then in the subsequent step, proton energy increases up to 2.5 GeV/u (p) and that of lead to 5.9 GeV/u in Proton Synchrotron (PS). In the PS splitting the bunches final structure is shaped with length of 4 ns into 72 (p) respectively 54 (Pb). The particle energy in the SPS for the proton reaches 450 GeV while for the lead ion it is accelerated upto 177 GeV and then in the final step these beams are injected into the LHC rings. It requires 3 to 4 cycles of the PS and 12 fills from SPS to complete one fill of LHC. The acceleration takes only few seconds upto LHC injection energy and heavy (lead) ions and protons are accelerated upto the final LHC energy in about 20 minutes. In the LHC rings clockwise and anti-clockwise beams protons and ions are circulated. In four interaction regions (points 1-4) the bunches are brought into collision after a reduction in crossing angle.

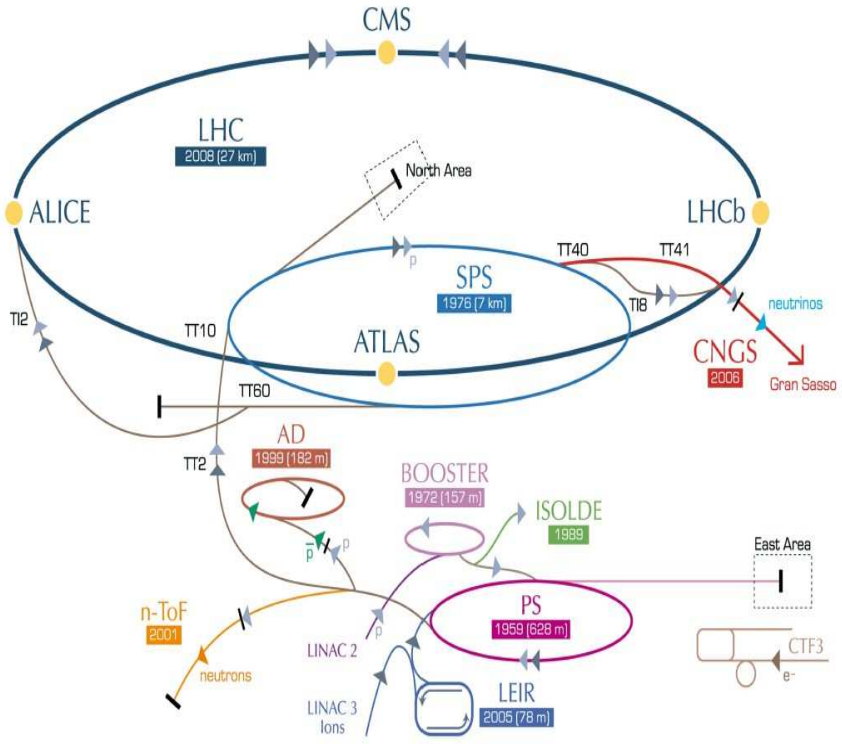

Figure 2.2: *CERN accelerator complex and the injector chain [93].*

2.2 LHC Experiments

At LHC there are a total seven experiments in which four are the major detectors installed [85] such as: A Large Ion Collider Experiment (ALICE)[86], A Toroidal LHC Apparatus (ATLAS) [87], Compact Muon Solenoid (CMS) [88] and LHC beauty (LHCb) [89] while three smaller experiments such as LHC forward (LHCf) [90], Total Cross Section, Elastic Scattering and Diffraction Dissociation (TOTEM) [91], and more recently the Monopole and Exotics Detector At the LHC (MOEDAL) [92]. A brief explanation of these experiments is given below:

- **ALICE**

  ALICE detector is used for measuring and analysing lead ion collisions. This experiment studies different properties of quark gluon plasma. ALICE however collects data for pp collisions as well as for reference for heavy ion collision studies. The detailed description of this detector will be given in Sec (2.3).

- **ATLAS**

  ATLAS is a general purpose detector at LHC, firstly to look into the physics at a wide range such as to explore the Higgs Boson which was discovered in 2012, and the extra dimension and supersymmetry (SUSY). Secondly its main purpose is to investigate those particles which are thought to make the dark matter. The

measurement of particle path, energy created in the collision are also recorded by the ATLAS detector.

- **CMS**

  CMS is a general purpose detector and its goal is the same as that of the ATLAS detector but it has different technical solution and design. To study the produced particles in pp collisions at $\sqrt{s} = 14$ TeV at luminosity of $10^{34}\ cm^{-2}\ s^{-1}$ at LHC is the main purpose of CMS detector. The goal of CMS experiment is to answer the most fundamental questions regarding the universe, e.g. what is the universe made up of ? and what forces act within it?

- **LHCb**

  LHCb is a forward detector. The main focus of this detector is on the pp physics. It studies the production and decays of beauty quarks, to understand why the entire universe in which we live is composed of matter but no anti-matter? LHCb investigates the difference between matter, anti-matter and also studies CP violations.

- **LHCf**

  LHCf is a small experiment at LHC for studying those particles which are in the direction of the beam. The energy and number of neutral particles are measured which gives us important information about the cosmic rays origin. This is the main purpose of LHCf detector.

- **TOTEM**

  The TOTEM is used to measure elastic, diffractive and total pp cross section.

- **MOEDAL**

  MOEDAL is used to search highly exotic particles and magnetic monopoles. In the LHCb/IP8 region the MOEDAL is installed whose surface area is about 30 m^2.

2.3 The ALICE setup

ALICE [94-97] is a heavy ion detector using heavy ion collisions. The study of QGP is the main aim of this detector. As discussed in Sec (2.2), the main focus of the ALICE detector is to study QGP. The weight of ALICE detector is 10000 tons, and it is 26 m long, 16 m high and 16 m wide. At LHC interaction point 2, the ALICE detector is situated 56 m underground. ALICE detector's overall view with red magnets door open is shown in Fig. (2.3). During the collisions, characterizing and subsequently reconstructing every particle is the main aim of ALICE detector. Similarly giving information about

the mass of the particles, its velocity and sign is the main task of the ALICE detector. The produced particles in the collisions then traverse through different layers of the detector outwards. The particles go through the first layer called the tracking system, next through electromagnetic and hadronic calorimeter and then finally through the last layer of muon spectrometer. As the detector is embedded in the magnetic field that bends the trajectories of the particles, so to find out the momentum and charge of the particles the magnetic field play an important role.

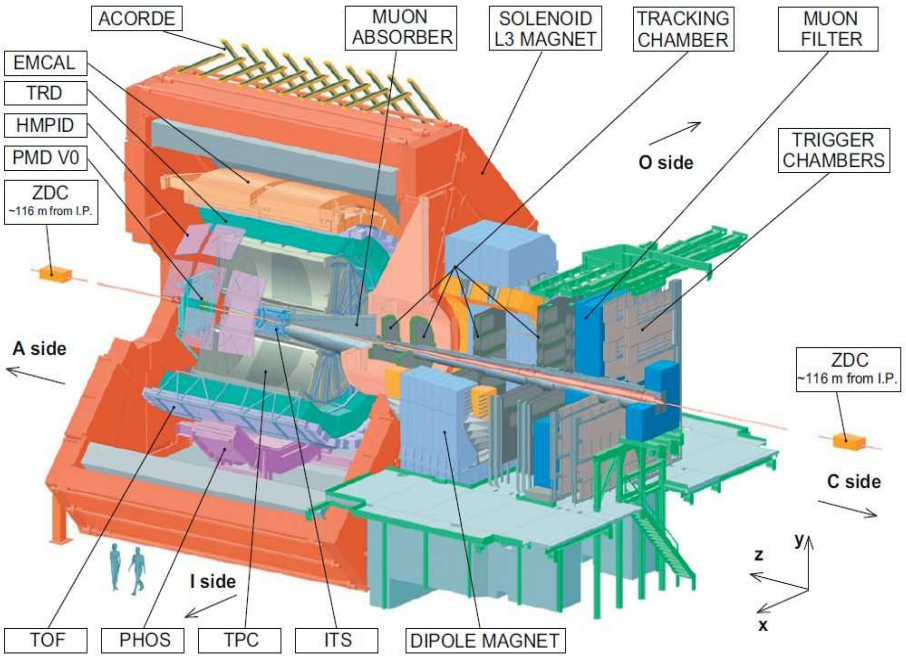

Figure 2.3: *ALICE detector layout [98].*

2.3.1 ALICE coordinates system

To describe the position of the detector and reconstructed tracks of the particles, the ALICE coordinates frame system is used [99, 100]. The origin of the coordinates system is defined by the nominal interaction point. The z-axis is defined as the direction of the beam and transverse plane is the x-y plane. LHC beam 2 is directed along +ve z-axis while LHC beam 1 is in the direction of -ve z-axis. The horizontal axis is represented by x-axis while vertical axis is represented by y-axis with positive y pointing up. "A" side in the Fig. (2.3), of the detector is given by positive z-axis, "C" side is given by negative z-axis, "I" side is given by positive x and "O" side is the region of negative x. The Cartesian coordinates system can be expressed also in terms of (r, θ, ϕ) or (ρ, ϕ, z) which represent spherical and cylindrical coordinates respectively.

2.4 Central Barrel Detector

For the particle tracking and its identification, the Central Barrel Detector (CBD) of ALICE is used which covers approximately the pseudorapidity region of $|\eta| < 1$. A uniform solenoidal magnetic field of 0.5 T is provided by the L3 magnet. The ITS and TPC is used for charged particles tracking and also providing the particle Identification. In addition, in central barrel there are several detectors which have more specific task (with smaller acceptance) and for particle identification most of these detectors are used. Central barrel detector description is given below.

2.4.1 Inner Tracking System

Located closest to interaction region and beam pipe [101] is the subdetector called Inner Tracking System (ITS). It is made of six layers of silicon detectors, with different detector technologies. Silicon Pixel Detector (SPD) makes the two innermost layers succeeded by two layers of Silicon Drift Detector (SDD) as can be seen in Fig. (2.4). The Silicon Strip

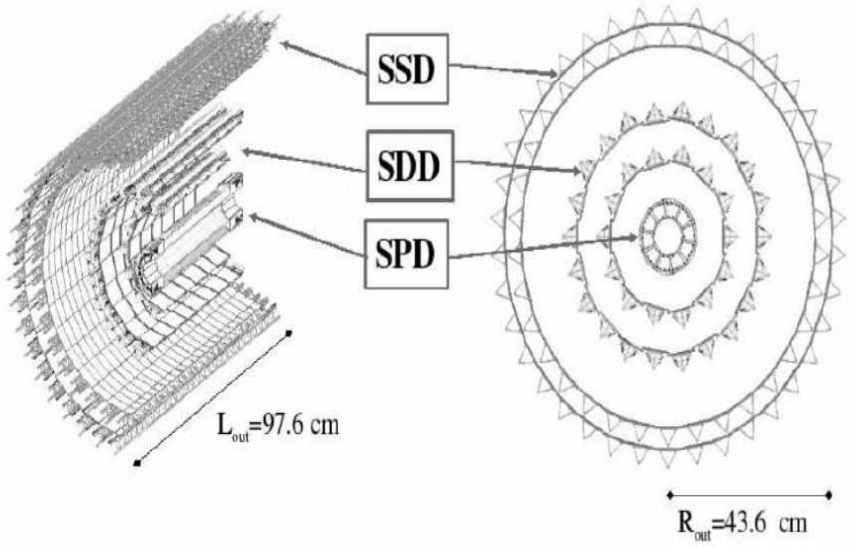

Figure 2.4: *Layout of the ITS detector, composed of SPD, SDD and SSD [102].*

Detector (SSD) forms the two outermost layers. The pseudorapidity range covered will be $|\eta| < 0.9$ to $|\eta| < 2$. Because of the closeness of the ITS detector to the interaction point it is used to track and identify particles which have momentum < 200 MeV and measure the position of primary interaction vertex with extremely high precision (100 μm) as well as improve particle momentum and angle resolution. Similarly, via decay length, study of the decay of charm and bottom can be performed by SPD because it can accommodated high particle density.

2.4.2 Time Projection Chamber

A large tracking detector located in the central barrel is Time Projection Chamber (TPC). It is filled by different mixture of gases such as, N_2, CO_2 and Ne. For track crossing the full detector, the full azimuth and $|\eta| < 0.9$ is covered by the TPC detector. The pseudorapidity coverage of TPC matches the ITS, TOF and TRD. From the collision point the charged particles when crossing through the gas inside the volume of the chamber, ionize it, and produce ions and free electrons which are separated in the drift field. The drift velocity of electrons towards the end plate is 2.65 cm/μs while it is 1000 times smaller in the case of ions. TPC can be used for the particle identification, vertex determination and charged particle momentum measurements.

2.4.3 Transition Radiation Detector

To identify positron and electron in 1 GeV/c momentum range is the primary purpose of the Transition Radiation Detector (TRD) [103]. For electron and high p_T charged particles TRD can also be used as trigger detector. The implementation of jet trigger is done by requiring several particles above some p_T. TRD has 18 super modules which contain 30 modules each. TRD allows to reconstruct products of semileptonic decay along with the information from the ITS. In conjunction with TPC, the production of heavy and light vector mesons resonances study is also done by TRD.

2.4.4 Time of Flight Detector

For identification of charged particle the Time Of Flight (TOF) detector is designed [104, 105]. This detector is also used to measure the speed of the particles and determining the time that a particle takes to travels from the vertex to reach it. In particular at the 3σ level, separation of pions to kaons up to 4 GeV/c momentum while separation of protons to kaons ratio is up to momentum 2.5 GeV/c is provided by TOF. Also with TOF information the identification of electrons and nuclei improves. Similarly charged particles velocity β, the time required to travel from the interaction point to the particle detector is measured by this detector. TOF has time resolution greater than 40 psec. In the interactions of different bunch crossing (pile up), it also allows to separate produced particles. TOF is comprised of Multigap Resistive Plate Chamber and area of 141 m^2 is covered by it. It is made up of thin layers of parallel glass with high electric field gas gaps. In a momentum range from 0.6 to 3 GeV/c, it identifies different types of particles such as kaons, pions and protons.

2.4.5 Electromagnetic Calorimeter

To measure the photon and electron energy at high p_T Electromagnetic Calorimeter (EMCal) is used [107, 108]. Trigger signals for photons, electrons and jets are also provided by this detector. Photons and electrons interact electromagnetically without hadronic showers. It is a lead calorimeter with cylindrical geometry and measurements of the energetic partons interactions with the dense matter is the main objective of this detector. The various particles can be detected in different layers of the detectors which is shown in Fig. (2.5). Its pseudorapidity coverage is $|\eta| < 0.7$ and is close to the acceptance of the L3 magnet.

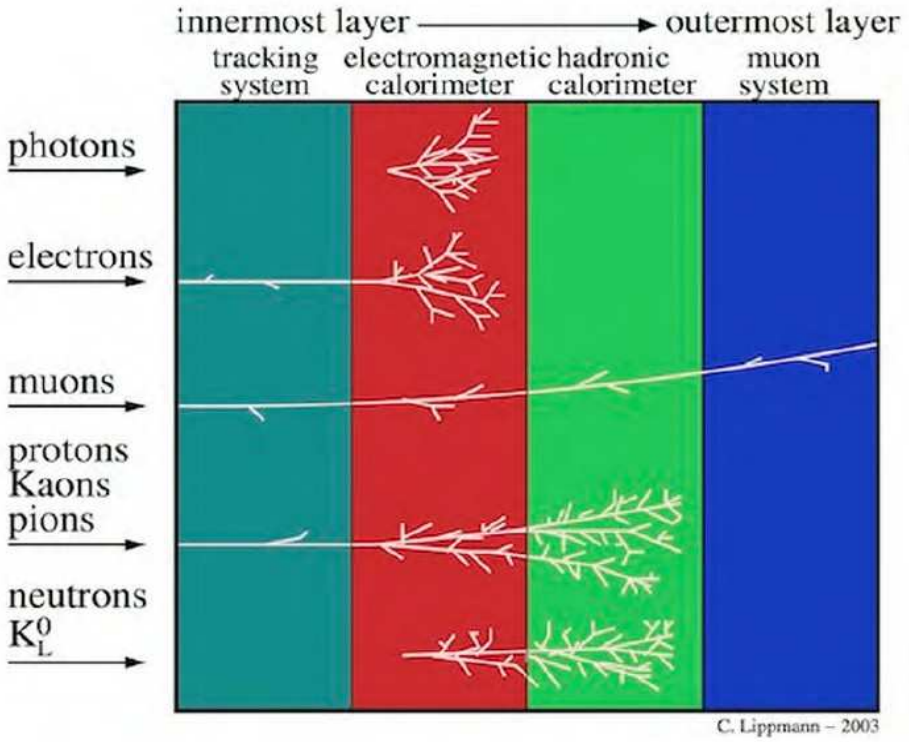

Figure 2.5: *Different detectors signatures of different particles [106]*

2.4.6 Photon Spectrometer

In order to measure the energy and spatial resolution in the range of $0.1 < E_\gamma < 100$ GeV/c range, the Photon Spectrometer (PHOS) is used, which is a homogeneous calorimeter detector [109]. Measuring the photons with very high accuracy is the main goal of PHOS. In the detection cells each PHOS module is divided. It is made of lead - tungsten and is capable of stopping and detecting photons due to its dense material. PHOS is located 4.6 m away from interaction point and its pseudorapidity coverage is $|\eta| < 0.12$.

2.4.7 High Momentum Particle Identification Detector

To enhance the particle identification of charged hadrons with momentum between 3 - 5 GeV/c the High Momentum Particle Identification Detector (HMPID) uses Ring Imaging Cherenkov (RICH) technology [110]. Cherenkov radiation also measures the velocity of charged particles in a liquid perfluorohexane radiator. In order to identify the particles, velocity information must be combined with momenta measurement from ITS/TPC. The hits left by charged particles are illustrated in Fig. (2.6). The HMPID pseudorapidity range is $|\eta| < 0.6$ and covers about 5 % phase space of the central barrel and its azimuthal angle is $1.2^0 < \phi < 58.8^0$.

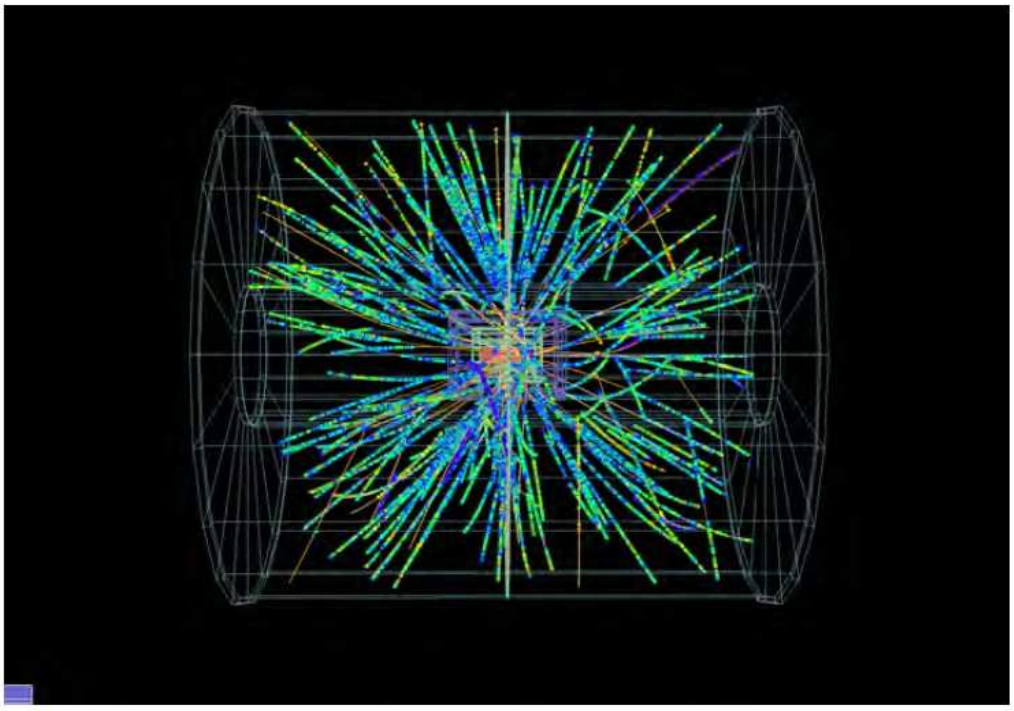

Figure 2.6: *An artistic view of p-Pb event made of the hits left by charged particles in the inner volume of the TPC detector [111].*

2.5 Forward and Trigger Detector

2.5.1 V_0 Detector

V_o is the main trigger detector [112, 113]. In heavy ion collisions VZERO V_o can be used as a minimum bias, multiplicity trigger, central and semi-central trigger detector. Multiplicity in heavy ion interactions is measured by the V_o detector, which is used in the offline analysis for the centrality measurement. In luminosity measurements, V_o also contributes in pp collisions. V_o is also used to reject background. Two V_o detectors are

placed at the forward pseudorapidities regions on each side of the point of interaction. The V_o - A covers $2.8 < \eta < 5.1$ while V_o - C covers -1.7 $< \eta <$ -3.7. Plastic scintillators used by both the detectors have disk shaped arrays which are connected to photomultiplier tubes via wavelength shifting fiber. In the radial direction every detector is divided into four rings and eight sectors in azimuth. Anisotropic flow measurement and event plane determination is allowed by these segmentations.

2.5.2 T_0 Detector

In order to initialize the signals for the TOF detector, the two TZERO (T_0) detectors are used for the particle identification with a very good precision ($<$ 25 ps) and can measure the timing of the collision. Accelerator team also used it as a start and luminosity monitoring detector. This detector is placed near the beam line and consist of two arrays with 12 Cherenkov counters. The pseudorapidity range of this detector is, $4.61 < \eta <$ 4.92 (T_0 - A) and -3.28 $< \eta <$ -2.97 (T_0 - C).

2.5.3 Forward Multiplicity Detector

Forward Multiplicity Detector (FMD) at forward rapidities measures the charged particles. To allow multiplicity measurement over a large η range, the FMD covers η range: -3.4 $< \eta <$ -1.7 as well as $1.7 < \eta < 5$, and overlaps partially with the SPD. There are five rings of the FMD in which three on the A-side and two on the C-side consists of 51200 silicon strips.

2.5.4 Photon Multiplicity Detector

Measurement of the photons spatial and multiplicity distribution in the forward region is done by Photon Multiplicity Detector (PMD), [114, 115] in the pseudorapidity range $2.3 < \eta < 3.7$ at full azimuth. Lead converter inside this detector consists of two gas proportional counters so the second detector layer detect photons while signal of charged particles appears in both layers.

2.5.5 Zero Degree Calorimeter

A detector which is used to measure the spectators energy is called Zero Degree Calorimeter (ZDC), [116]. It also gives an important information about the number of spectators and centrality or impact parameter of nuclei in heavy ion collisions. In LHC tunnel, the distance of hadronic ZDC from the interaction point is 116 m. The LHC bending magnets

do not deflect the spectator neutrons so two neutron ZDCs (ZN) can be used to detect these spectators, while the LHC bending magnets deflect the protons spectators due to its higher charge to mass ratio. Therefore proton ZDC is used to detect them in the LHC tunnel. As a detection material both the ZDCs use a passive absorber with embedded quartz fibers. A particle shower is created in the absorber as illustrated in Fig. (2.5), and produces the Cherenkov radiation in the fibers which is detected in the photomultiplier tube (PMT). It can be moved out of the horizontal beam plane, when not required.

2.6 Muon Spectrometer

With respect to the other particles muon penetrate into matter easily, therefore at forward rapidities -4.0 $< \eta <$ -2.5 a set of absorbers are placed. The muon spectrometer allows the study of heavy mesons and heavy quarks vector meson resonances which are produced from the decays of muons. Actually the muon spectrometer has a passive front absorber (about 4 m long) plus an additional iron wall (1.2 m) in order to absorb hadrons and photons produced in the collisions [117, 118], as shown in Fig. (2.7). By a series of tracking detectors the muons are detected at this point which are able to pass through those filters. The muon spectrometer is capable to take data with a higher rate and luminosity.

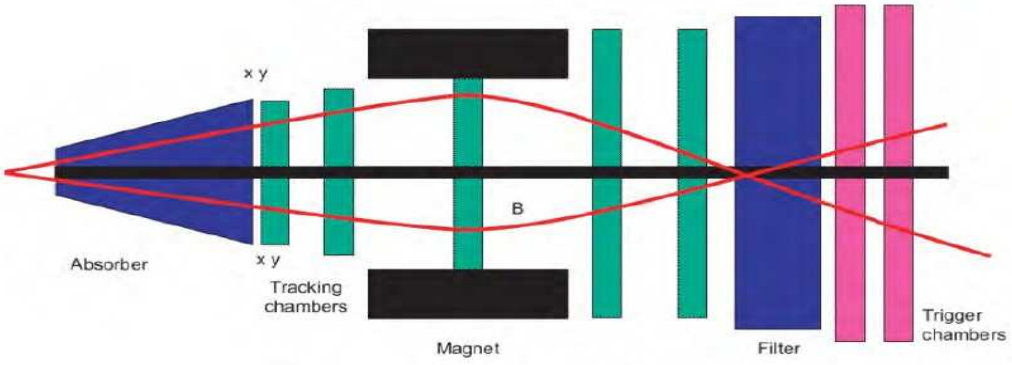

Figure 2.7: *Muon Spectrometer in ALICE composed of an absorber [119].*

2.7 ACORDE

ACORDE stands for Alice Cosmic Rays Detectors which detect cosmic rays of high energy, in conjunction with TPC, TRD and TOF, by triggering the arrival of atmospheric muons. The top surface of L3 magnet has an array of these plastic scintillators. To some of the tracking detectors in ALICE it also provides fast trigger signals.

2.8 Trigger

At the LHC high energy physics experiments the collision rate is very high and large storage capacity is required to store its resulting data. So some form of triggering is required to preferentially select interesting events for analysis and storage.

Chapter 3

Methodology

To achieve the aim, we have used MC simulation packages with FORTRAN-77 and C++ languages. We have used different MC models such as HIJING-1.0, UrQMD-3.4, EPOS-1.99, SIBYLL-2.3c, QGSJETII-04 and EPOS-LHC, and simulated 150000 events. Using the simulated data we constructed p_T, η, y, R_{pPb} distributions for the charged particles produced in p-Pb collisions. This data was obtained for the most central p-Pb collisions. The simulated data were compared with the experimental data obtained from different LHC experiment such as ALICE, ATLAS, and CMS. The p-Pb collisions were simulated for the energies 0.9 TeV and 5.02 TeV. For charged particles we considered proton, anti-protons, $\pi^{\pm}$, $K^{\pm}$ mesons. The main purpose of these MC event generators is to produce virtually the relevant collisions events as being produced in real experiments, predicting the same average behavior, and fluctuation that would be seen in the real data. Monte Carlo techniques are used in the event generators to select random variables based on the probability distributions. In this chapter, the simulation of hadron-hadron and hadron-nucleus collisions using different high energy event generators such as HIJING-1.0, UrQMD-3.4, EPOS-LHC, EPOS-1.99, SIBYLL-2.3c and QGSJETII-04 models are presented. The detailed description of these models is given below.

3.1 HIJING-1.0

A Monte Carlo event Generator Heavy Ion Jet Interaction Generator (HIJING) [120] is developed to study phenomenology of "pp", "pA" and "AA" collisions at high energies. HIJING is written in FORTRAN-77 language. In HIJING we also study particle production and jets in pp, pA and AA collisions. For jet fragmentation [121], this model combines Lund model [122] with QCD inspired model for the multiple jet production [123, 124]. Lund FRITIOF [125] and Dual Parton Model [126-128] are based on the HIJING formulation. Production of multiple minijets including radiation in initial and final states is also considered by HIJING. The production of multiple minijets in the

interactions of hadron and nucleus at high energy becomes more and more important. For the study of new physics in QGP formation, information must be extracted about the minijets. In HIJING, the parameters have to be tested first in pp collisions and when extrapolating to heavy ion collisions some other effects have to be considered such as parton shadowing, which is a nuclear effect, and final state interaction. In high energy nuclear interactions, to provide theoretical laboratory, a MC HIJING model is used for studying jets and one of its important feature called jet quenching [129]. It also includes nuclear shadowing [130] of parton function structure to study the nuclear effects and also study the final state interactions of jets at high p_T in terms of, dE/dz (parameter for effective energy loss) [131, 132]. To address the relations between hard pQCD processes and non-perturbative physics at low p_T, HIJING makes an important effort at pp and $p\bar{p}$ level. This model is extensively tested for energies from $\sqrt{s} = 50$ GeV to $\sqrt{s} = 1800$ for $p + p(\bar{p})$ and at moderate energies $\sqrt{s} = 20$ GeV/n for pA, AA collisions [133, 134]. In this version of the HIJING model, however the final state interactions between the partons and hadrons was not considered [135].

3.1.1 Mathematical description

In pQCD the hard parton scattering cross section can be written as [136].

$$\frac{d\sigma_{jet}}{dp_T^2 dy_1 dy_2} = K \sum_{a,b} x_1 x_2 f_a(x_1, p_T^2) f_b(x_2, p_T^2) d\sigma^{ab}(\hat{s}, \hat{t}, \hat{u})/d\hat{t} \tag{3.1}$$

where $y_1 y_2$ represent scattered partons rapidities and $x_1 x_2$ are carried fraction momentum of the initial partons. The summation is done over all partons species. The x_1 and x_2 are given by $x_1 = x_T(e^{y_1} + e^{y_2})/2$, and $x_2 = x_T(e^{-y_1} + e^{-y_2})/2$, where $x_T = 2p_T/\sqrt{s}$. For the higher order corrections a factor $K \approx 2$ is roughly included. In HIJING, $f_a(x, Q^2)$, is the default structure functions, the Duke-Owens structure functions, set to 1 [137]. The total inclusive jet cross section, σ_{jet} can be calculated by integrating Eq. (3.1) using a low p_T cutoff p_0. At impact parameter, b, for a nucleon-nucleon collisions the average number of semihard partons is $\sigma_{jet} T_N(b)$, where $T_N(b)$ is taken between two nucleons partonic overlap function. The probability of multiple minijets production from semiclassical probabilistic model [138] is then:

$$g_j(b) = \frac{[\sigma_{jet} T_N(b)]^j}{j!} e^{-\sigma_{jet} T_N(b)}, j \geq 1. \tag{3.2}$$

Similarly the soft interactions are represented by some inclusive cross section σ_{soft}, which, unlike σ_{jet}, can be obtained from phenomenology. So without any hard processes the probability for only soft interactions is:

$$g_0(b) = [1 - e^{-\sigma_{soft} T_N(b)}] e^{-\sigma_{jet} T_N(b)}. \tag{3.3}$$

To simulate multiple jets production in HIJING program AA collisions the total inelastic cross section is given by:

$$\sigma_{in} = \int d^2(b) \sum_{j=0}^{\infty} g_j(b) = \int d^2(b)[1 - e^{-}(\sigma_{soft} + \sigma_{jet})T_N(b)]. \tag{3.4}$$

3.2 UrQMD-3.4

UrQMD stands for Ultra-relativistic Quantum Molecular Dynamics Model [139] and is a MC simulation code used for pp, pA as well as AA collisions. For studying a wide variety of heavy ion related effects UrQMD, uses transport model for dynamical understanding. It is designed as multipurpose tool ranging from multifragmentation and collective flow to particle productions and correlations. In heavy ion collisions UrQMD also gives a detailed information about the multi fragmentation. This model includes the PYTHIA routines from the LUND group [140] for hard pQCD scattering. In nuclear, particle and detector physics this model has large number of applications. In heavy ion collisions, for creation of hot and dense hadronic medium many important theories are also taken into account in this model. On the particle level using interaction cross sections between hadrons and resonances, pp and AA collisions at low energies are modelled while the excitation of color strings fragmenting into hadrons is applied at higher energies.

Like other Quantum Molecular Dynamics (QMD) models, in UrQMD model within a sphere with radius *R(A)*, the nucleons of the colliding nuclei have been randomly distributed such as.

$$R(A) = r_0(\frac{1}{3}[A + (A^{\frac{1}{2}} - 1)^3])^{\frac{1}{3}} \tag{3.5}$$

$$r_0 = (\frac{3}{4\pi\rho_0})^{\frac{1}{3}} \tag{3.6}$$

where ρ_0 is the normal density of nuclear matter. The nucleon takes its location randomly if the density is too high. The nucleons take their initial momentum randomly between 0 and Thomas Fermi momentum:

$$p_F^{max} = \hbar c(3\pi^2\rho)^{\frac{1}{3}} \tag{3.7}$$

where ρ is the proton or neutron local density. According to the quadratic measure ($dW \sim bdb$) impact parameter of a collisions has been calculated in UrQMD. Projectile and target in UrQMD, at given impact parameter are placed along the collisions axis at 3 fm. The interaction in UrQMD is possible if $b < sqrt(\frac{\sigma_{tot}}{\pi})$. Here σ_{tot} and b denotes cross section and impact parameter respectively. Interaction cross sections in UrQMD have been taken from the high energy computer simulation program PYTHIA [141]. There

are 55 different types of baryons and 32 types of mesons species contained in the UrQMD model.

3.2.1 Physical description

For different colliding nuclei the UrQMD model is used to simulate events from Coulomb potential to LHC energies. The following phenomena occur in UrQMD model:

- At high temperature creation of dense hadronic matter.
- Nuclear matter properties, delta and other resonance matter.
- Anti-matter and mesonic matter creation.
- The rare particles creation and transport in hadronic matter.
- In matter modification, destruction and creation of strangeness.
- Electromagnetic probes emission.

3.3 Cosmic Ray Monte Carlo package

The Cosmic Ray Monte Carlo (CRMC) is a package providing an interface for access to different cosmic ray and non cosmic ray event generators. To access the output from event generators the CRMC package provides a common interface. As the interface is linked to wide range of models, the main focus is on using these models for the simulation of extensive cosmic ray air showers. This package is used to model the secondary charged particle production in the hadronic collision. The Cosmic ray MC codes are based on the Gribov-Regge theory (GRT). The models included are described below:

3.4 EPOS

EPOS stands for Energy conserving quantum mechanical multi-scattering approach, based on Parton (parton ladders), Off-shell remnants and Splitting parton ladder and is a MC event generator used for hadronic interactions which exchange parton ladder between two hadrons for their interaction [142]. EPOS is established on two theories: Parton-Based GRT in which effective field principle is used by the GRT and it focuses on soft interactions. Pomerons are the objects through which hadrons interact. They play an essential role in the calculation of cross section of multiple scattering, as shown in Fig. (3.1) The gluons and quarks are introduces by parton model which interact by the exchange of gluons. According to this model there are two parts of the parton ladder,

one is the hard part that depicts the hard scattering of the partons while the second part is the soft part which is parameterized in Regge pole fashion it is parameterized. It is ensured in the parton model as well as in the GRT combination, that in the cross section and production of particles, the energy is shared properly. The parton production is represented by Lund string model [143]. There are two parton ladders i.e. open parton ladder which contribute to inelastic scattering and support particle production while the closed parton ladder support the elastic scattering as shown in Fig. (3.1).

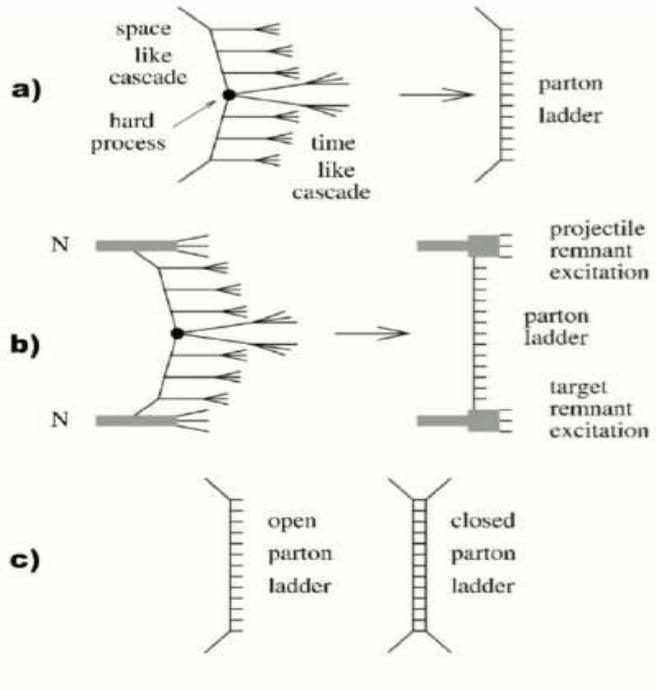

Figure 3.1: *a)Elementary parton-parton scattering, represented as parton ladder. b)Full representation of scattering, completed with remnants. c)Open and closed parton ladder [144]*

.

EPOS can be used for cosmic ray physics and heavy ion physics. To depict reactions at high energy interactions in RHIC and LHC, the EPOS model is used [145]. EPOS model has another speciality which is its target and projectile remnants, that provide a good description for the production of baryons and anti baryons.

3.4.1 Gribov-Regge Theory (GRT)

By construction GRT, is a theory of multiple scattering, in which interactions are taking place through "pomerons". The exchanges of a single pomeron representing to a single amplitude, T, is given by:

$$T(s,t) \sim \iota s^{\alpha_0 + \alpha' t} \tag{3.8}$$

where different parameters can be determined by experiment. There are several pomerons exchange in parallel in the hadron-hadron scattering, as shown in Fig. (3.2). For the

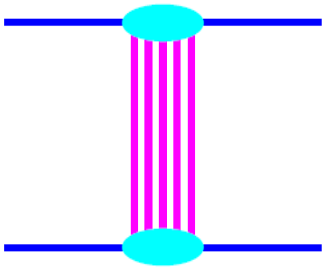

Figure 3.2: *Scattering of Hadron-Hadron in GRT where between the hadrons the thick lines represent Pomeron each [146].*

inelastic cross section one can obtain an expression using general cutting rules of field theory,

$$\sigma_{inel}^{h_1 h_2} = \int d^2b\{1 - exp(-G(s,b))\} \tag{3.9}$$

where $G(s,b)$ is the Fourier transform of $T(s,t)$ and represents an elementary interaction. This theory is generalized to AA interaction, where corresponding cross sections formula are then derived.

3.4.2 The Parton Model

For AA scattering the parton models standard approach is to represent the partons projectile and target by, f_{h_1} and f_{h_2}, momentum distribution functions, and calculation of the production of parton jets is done through inclusive cross sections with the squared transverse momentum, $p_\perp^2$ larger than some cutoff Q_0^2 given by:

$$\sigma_{inel}^{h_1 h_2} = \sum_{i,j} \int dp_\perp^2 \int dx^+ \int dx^- f_{h_1}^i(x^+, p_\perp^2) f_{h_2}^j(x^-, p_\perp^2) \frac{d\hat{\sigma}_{ij}}{dp_\perp^2}(x^+ x^- s)\theta(p_\perp^2 - Q_0^2) \tag{3.10}$$

where parton flavor is represented by i, j and $\frac{d\hat{\sigma}_{ij}}{dp_\perp^2}$ represents the elementary parton parton cross section.

3.4.3 Parton-based Gribov-Regge Theory

A newer access to the hadronic interaction provides a rigorous treatment of the multiple scattering aspects where, by the rules of the field theory, the energy conservation is clearly determined for particle production and for cross section calculations. In both cases energy is shared in different interactions properly which occur in parallel as shown in Fig. (3.3),

for the pp and Fig. (3.4), for the pA interactions which can be generalized for the AA interaction.

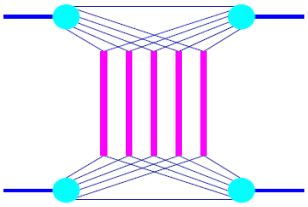

Figure 3.3: *Graphical representation of elastic amplitude for proton-proton scattering [146].*

It is a crucial aspect of this approach, that is considered the first step for the high energy nuclear scattering to construct a consistent model.

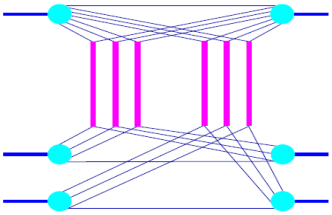

Figure 3.4: *Graphical representation of elastic amplitude for proton-nucleus scattering or a proton interaction with two target [146].*

As shown by the thick lines in the Figs. (3.3) and (3.4), the elementary interactions are the sum of the hard, semi hard and soft contribution which provide a coherent treatment of hard and soft scattering. This approach provides a connection between parton model and Gribov-Regge approach, called "Parton-based Gribov-Regge Theory". There are different versions of EPOS model. In our simulation we will use EPOS-1.99 and EPOS-LHC, which are explained below.

3.5 EPOS-1.99

EPOS-1.99 is based on multiple scattering GRT, string fragmentation and perturbative QCD approach. In the study of Extensive Air Shower (EAS), EPOS is the most widely used hadronic interaction model. EPOS-1.61 was the first version of EPOS which was carefully tested and tuned with the RHIC and SPS experimental data. However some results were in contradiction with the KASCADE data [147], when used in air shower simulation program like CORSIKA [148]. In fact the hadrons produced by EPOS-1.61 carry excessively low energy and as a result the shower were too old when they reached the ground. To take into account these discrepancies and implement other improvements in the code, a new version of EPOS-1.99 was developed. In EPOS-1.99 model some

effects have been introduced such as nuclear effects, screening and parton saturation. Furthermore in EPOS-1.99 model the high density effects leading to collective behavior in heavy ion collisions were also taken into account. The non-linear effects at high energy and high densities are specially crucial in the extrapolation of EAS and in EPOS-1.99 model this is the main part which has been modified.

3.6 EPOS-LHC

EPOS-LHC is the high energy hadronic interaction and one of the latest post-LHC model. To reproduce experimental data on hadronic interactions the EPOS-LHC model has been tuned according to different LHC experiments up to $\sqrt{s} = 7$ TeV [149, 150]. Like EPOS-1.99 model, EPOS-LHC also depends on multiple scattering GRT, string fragmentation and pQCD. But few modifications are included in the EPOS-LHC related to flow parameterization of the produced thermalized matter at high density in heavy ion or pp collisions, the core decay and the formation of baryons (with, as compared to string fragmentation, the multistrange production being more important). For the cross sec-

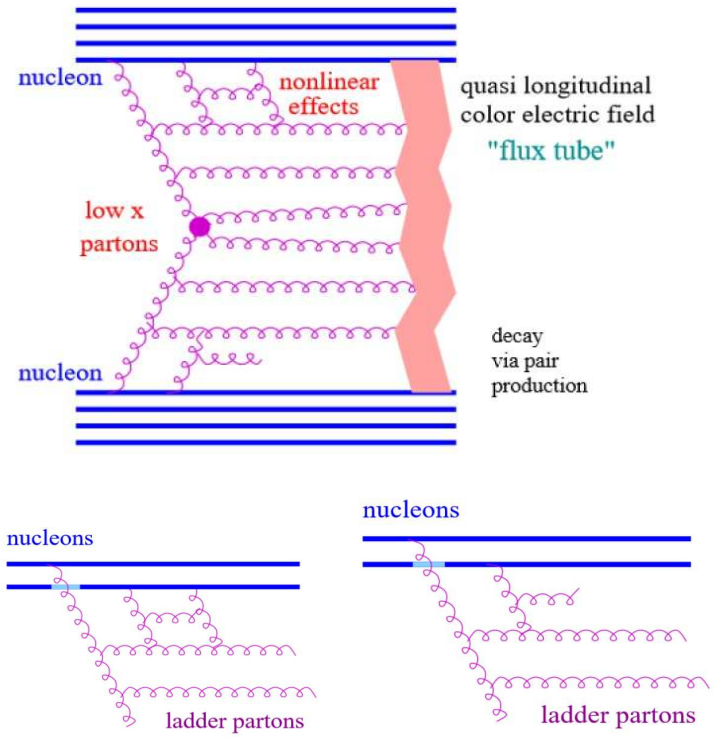

Figure 3.5: *Elementary interaction in EPOS model shown in the top of the figure, the below left figure show the elastic parton ladder rescattering while the right figure show the inelastic parton ladder rescattering [151]*

tion below $\sqrt{s} = 7$ TeV, the EPOS-1.99 and EPOS-LHC predicts almost similar values. However at high energies the predictions begin to separate. The non-linear effects are

parameterized in the EPOS-LHC models. The gluon densities get high enough at higher energy for gluon fusion to occur due to which two types of rescattering i.e. elastic as well as inelastic are produced as shown in Fig. (3.5). Where the ladder partons rescatters of the projectile and target nucleon/parton. The total and inelastic cross section reduced due to screening in elastic scattering and therefore the particle production decreases. The elastic scattering parameters depend on nuclear mass and centre of mass energy of hadron collision and saturate at high energies. The parameters of inelastic scattering are very important for reproducing charged particle production and transverse momentum spectra. Unlike other models, EPOS-LHC is on the microcanonical level (parton level) rather than the canonical level (hadron level). All the Pomeron-Pomeron couplings of the multiple scattering is calculated by the EPOS-LHC model.

3.7 QGSJETII-04

QGSJETII-04 is a Monte Carlo generator for hadronic interactions [152]. Like EPOS model, the QGSJETII-04 model is also based on the Gribov-Regge effective field theory [153, 154]. In EPOS model the treatment of semihard process is based on the QGSJET. However in QGSJET the Gribov-Regge theory is applied to hadrons while in EPOS it is applied to partons. As a consequence, in QGSJET the amplitude level energy is not conserved [155]. The treatment of non-linear effects does not parameterize in QGSJETII-04 model. To account for the non-linear effects QGSJETII-04 uses pomeron-pomeron coupling from the Gribov-Regge theoretical framework. The interaction of partons cascades are represented through the pomeron-pomeron coupling when they overlap in phase space. To calculate the total and elastic cross section of all the possible pomeron interactions the QGSJETII-04 does the resummation of all the enhanced diagrams as shown in Fig. (3.6) where parton cascade is represented by cut pomerons while the uncut pomerons the elastic rescatterings of the cascade of the projectile and target partons. The triple-pomeron coupling also depends upon the impact parameter and parton density (or c.m energy).

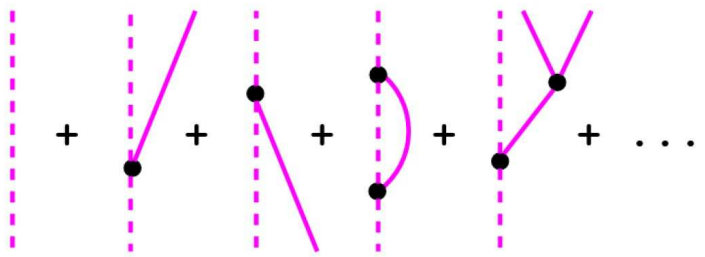

Figure 3.6: *Enhanced diagram in QGSJETII-04 [156]*

In QGSJETII-04, the less number of parameters do not depend on nuclear mass number

but only depend on the pomeron diagrams. In QGSJETII-04 model it is not necessary to get additional parameter from pp to pA or AA interactions. From resummation of the enhanced cut diagrams the extrapolation is followed and extended Gribov-Regge with Glauber theory [157, 158]. QGSJETII-04 model has also some disadvantages in which one is that the multi-pomeron coupling is dominated by soft processes, therefore in this approach there is only saturation for the soft processes. For hard processes the multi-pomeron coupling is not taken into account by the QGSJETII-04 and therefore for the hard processes there is no screening/saturation in the model. The second disadvantage is that the energy is not conserved between the multiple scattering in the QGSJETII-04 model. The advantage of this model over the EPOS-LHC is that it has less number of parameters.

3.8 SIBYLL-2.3c

SIBYLL-2.3c [159-161] is a MC event Generator which is based on the Dual Parton Model (DPM) [162-164], minijet model [165-167] and Lund MC fragmentation [168, 169]. In the simulations of extensive air shower, the SIBYLL-2.3c is one of the standard event generator used. The design of SIBYLL-2.3c is based on the description of the general features of hadronic multiparticles production, like the production of diffractively excited states of projectile and target, the leading particle effect, the approximate scaling of leading particle distributions with interaction energy and the formation of high p_T jets predicted by QCD. The main focus of the SIBYLL-2.3c model is on those physics aspects which are most relevant for the development of extensive air showers, like particle production and energy flow in the forward phase space region. The SIBYLL-2.3c is a new version. Elements of the Gribov-Regge theory are implemented in the newer version of SIBYLL-2.3c. The DPM is based on quarks and diquarks. Here two quarks are formed between the quark(diquark) of the target and diquark(quark) of the projectile. If the mass of these strings is higher than some threshold mass then the fragment following the Lund string fragmentation such as in EPOS-LHC and in QGSJETII-04 model where the pairs of $q\bar{q}$ and $qq - \bar{q}\bar{q}$ pairs are created. At higher centre of mass energies greater than hundreds of GeV the increase of multiplicity, mean transverse momentum as well as density of central rapidity particles with energy can not be described well by this model. These effects in SIBYLL-2.3c model are associated with low transverse momentum jets from hard interactions and are described by perturbative minijets model (instead of DGLAP equation in EPOS-LHC and QGSJETII-04). The SIBYLL-2.3 c model has relative large phase space for soft interaction. For multiple scattering some elements of the Gribov-Regge theory are implemented in this model. Similar to the Good Walker [170] used by the QGSJETII-04 the diffractive interaction are modeled by a two channel eikonal

model. By Glauber scattering [171] the extrapolation from pp interaction to pA interaction is done but a combination between Glauber theory and superposition model is used for AA interactions, i.e. the semisuperposition model [172]. As compared to the full Glauber model used by the EPOS-LHC and QGSJETII-04 the semisuperposition model for nucleus-nucleus interaction is less precise which is a disadvantage of this model.

3.9 Data Analysis Framework

3.9.1 ROOT

ROOT [173, 174] is an object oriented program for the data analysis developed by the CERN. An old software pacakge called Physical Analysis Workstation (PAW) [175] was replaced by ROOT software. PAW has been developed at CERN since 1986. PAW is written in FORTRAN programming language while ROOT is written in C++ language which was initially developed by the Bjarne Stroustrup. Rene Brun in turn developed ROOT using C++ for further usage. The reason they developed ROOT is, it was not expected that PAW needs to handle such a large amount of LHC data because the data was expected to be very huge as compared to the previous experimental outputs. ROOT is designed as a framework, a software tool and a set of C++ classes. In coherent ensembles all ROOT tools are integrated. All types of mathematical operations are provided by ROOT like fitting and unfolding. The ROOT packages [176] contain important functions such as graphing, curve fitting, histogrammings, statistical tools for the data analysis, matrix algebra, to analyze the distribution and function, four-vector used in high energy physics and minimization of functional which makes analysis easy and comprehensive. ROOT is designed for high computing efficiency because it processes huge amount of data produced by the LHC experiments of the order of several petabytes per year. For physics analysis not only the equipment is needed for the experiment like ALICE, software tools must be provided for the simulation of events and of the detector. Furthermore for simulation and measured events a reconstruction is required for which AliRoot [177] is used which is based on ROOT and contains all C++ classes required exclusively by the ALICE experiments.

3.9.2 Origin

For data analysis Origin is a powerful, publication-quality graphing and full-featured software, suitable for the need of engineers and scientists. For beginners the Origin software offers an easy-to use interface and ability to customize the analysis and graphing tasks using templates, programming, and themes for advanced users.

3.9.3 Rivet

Robust Independent Validation of Experiment and Theory (Rivet) toolkit [178] is a framework which uses HepMC format for the events analysis. For analysis Rivet also provides the infrastructure, and a set of efficient observable calculator. For generator validation, tuning and regression testing rivet is designed to be an efficient and simple to use system. The analyses code from LHC and other high energy collider experiments is preserved for comparison to and development of future theory models through Rivet. Rivet is used by MC generator developer, phenomenologists and experimentalists on the LHC and other facilities.

3.9.4 HepMC 2.06.09

HepMC [179] written in C++ is an object oriented event record in HEP for the MC Generators. To a particular experiments and event generator it has been developed independently. HepMC can be used for both purposes i.e. it can be used as a event generator framework and for storing events it is used as a container class. It confesses for the modularization of event generators, where for different steps or components of the event generation process the different event generators could be employed. Using diagram with a graph structure shown in Fig. (3.7) (left) the physics events are generally visualised, while the HepMC reproduced these event graphs by separating out particles from vertices and in the form of edge and nodes respectively, shown in Fig. (3.7) (right). The incoming and outgoing particles listing is maintained at each vertex while each particle points back to its production vertex and decay vertex.

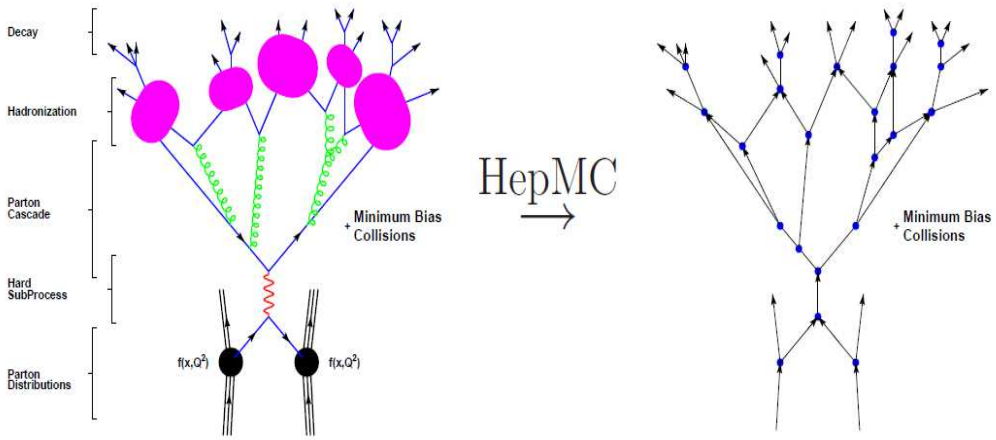

Figure 3.7: *A collision event visualised by physicist (left), similar events in HepMC are stored in graph structure (right) [179]*

The extension to multiple collisions is natural- from several different initial processes there is a superposition of graph and so the event may contain unlimited graphs (possibly interconnected). In each event the number of particles/vertices is also open-ended. The event subset may be examined or modified without having to interpret complex parent/child relationships codes or re-shuffle the rest of the event record.

3.9.5 Features of the HepMC Event Record

- The information provided by iterator and range method is simple and easy to access them.
- It has minimum dependencies.
- Physically similar to the collision event, it stores information in a graph structure.
- It allows specification of units of the momentum and length.
- It allows for the spin density matrices inclusion.
- It allows for an arbitrary number of flow pattern tracing.
- It has the ability to store random number generator states (as integers).
- It provides facility to store an arbitrary number of event weight.
- It has the ability to store the information of parton distribution function.
- It has the ability to store information of heavy ion collision.
- It has the ability to store information of generated cross section on an event by event basis.
- It supports standard I/O streaming .
- To support other event records it provides strategies for conversion to/from HEPEVT [180] which are easily extendible.
- To support other form of persistency, it provides strategies for input/output to/from ASCII file which are easily extendible.

Chapter 4

Results and Discussion (Part-I)

4.1 p-Pb collisions

In this chapter results for charged particles transverse momentum, p_T, pseudorapidity, η, rapidity, y, multiplicity, $dN/d\eta$, distributions are presented for p-Pb collision systems at LHC energies, 0.9 TeV, 5.02 TeV and 7 TeV. We have also compared the results of p-Pb collisions with those obtained from pp collisions. In this section we compare the results from model predictions with the experimental data. In heavy ion program at the LHC p-A collisions can be used as a reference to understand and interpret A-A collisions data. They allow disentangling initial state effects from final state effects already existing in cold nuclear matter and also a baseline measurement for A-A collisions. It is clearly pointed out by several measurements that p-A collisions cannot be explained by incoherent superposition of pp collision, since it represents the existence of already observed effects in A-A collisions [181].

4.1.1 Study of transverse momentum distributions in p - Pb interactions at 0.9 TeV and 5.02 TeV

The p_T distribution of primary charged particles including $\pi^{\pm}$, $K^{\pm}$ mesons, proton and anti - proton have been investigated in p-Pb interaction at $\sqrt{s_{NN}}$ = 0.9 TeV and 5.02 TeV using Monte-Carlo models such like, EPOS-LHC, QGSJETII-04 and EPOS-1.99. All the above mentioned particles are considered as primary charged particles, including the strange hadron decays, at variance to what is done by the LHC experiments.

Figures (4.1-4.5) show the comparison of p_T distributions of particles produced in the trio models with the ALICE data at $\sqrt{s_{NN}}$ = 5.02 TeV [182] for the pseudorapidity regions, $|\eta| < 0.3$, $0.3 < |\eta| < 0.8$, $0.8 < |\eta| < 1.3$, and with the data from the CMS experiment for $1.3 < |\eta| < 1.8$ [183]. The comparison is carried out for the central, mid, forward

and most-forward pseudorapidity regions: $|\eta| < 0.3$, $0.3 < |\eta| < 0.8$, $0.8 < |\eta| < 1.3$, $1.3 < |\eta| < 1.8$ and $1.8 < |\eta| < 2.3$ respectively with 150k events simulated in the models.

Figure (4.1), shows the differential yield of primary charged particles as a function of p_T for the pseudorapidity interval $|\eta| < 0.3$ at $\sqrt{s_{NN}} = 0.9$ TeV and 5.02 TeV. The figure shows that at 0.9 TeV, EPOS-1.99 model gives higher prediction compared to the other two models and a random behavior is observed at $p_T \approx 10$ GeV/c. For $\sqrt{s_{NN}} = 5.02$ TeV simulated distributions are compared with the ALICE experimental data. The shape of the distribution obtained from the models look similar to the experiment. However, all of these models overestimate in comparison with the experimental data for the region up to $p_T \approx 5$ GeV/c, after which the models seem to be consistent with the experimental data where as EPOS-LHC reproduces the experimental data very well. On the other hand, after $p_T \approx 5$ GeV/c, EPOS-1.99 distributions have lower multiplicity and QGSJETII-04 model gives higher multiplicity.

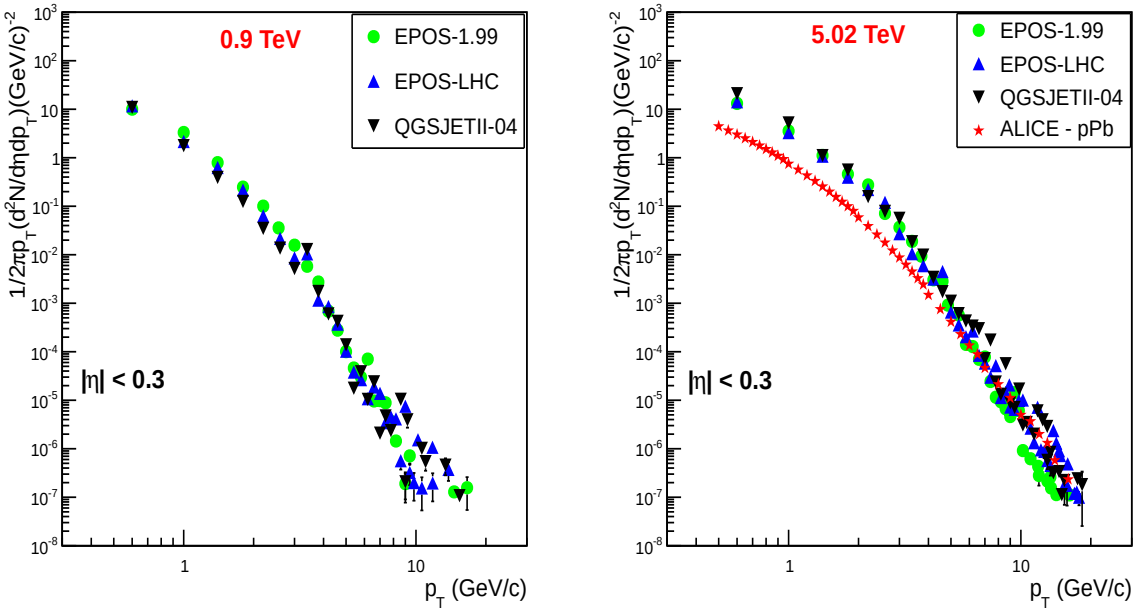

Figure 4.1: *p_T distributions in p-Pb collisions at $\sqrt{s_{NN}} = 0.9$ TeV and 5.02 TeV in $|\eta| < 0.3$ region.*

From Figs. (4.2-4.3), it seems that at 0.9 TeV, for $0.3 < |\eta| < 0.8$, these models seem to be consistent up to $p_T \approx 3$ GeV/c and the multiplicity is steadily declining with some (statistical) fluctuation. For $0.8 < |\eta| < 1.3$ all three models give similar predictions up to $p_T \approx 1.5$ GeV/c. In the pseudorapidity regions $0.3 < |\eta| < 0.8$ and $0.8 < |\eta| < 1.3$ at $\sqrt{s_{NN}} = 5.02$ TeV, model predictions are closer to the distributions from the experimental data after $p_T \approx 5$ GeV/c. For $p_T > 5$ GeV/c, EPOS-LHC seems to describe experimental data very well. EPOS-1.99 gives lower multiplicity while QGSJETII-04 model gives higher multiplicity. The p_T distribution for the forward $|\eta|$ - region is shown in Fig. (4.4)

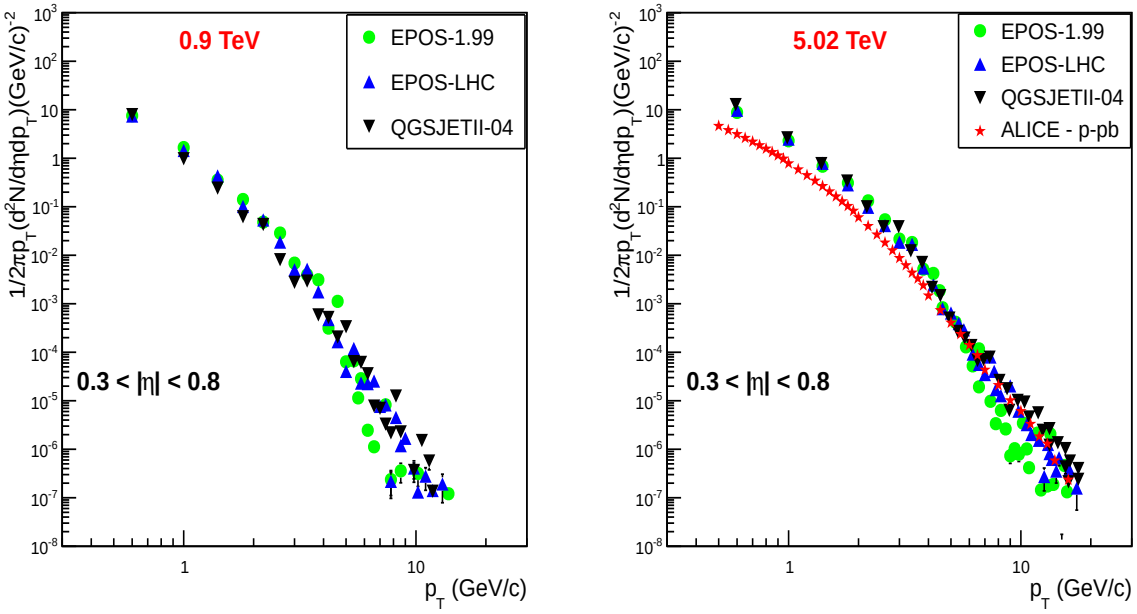

Figure 4.2: *p_T distributions in p-Pb collisions at $\sqrt{s_{NN}}$ = 0.9 TeV and 5.02 TeV in $0.3 < |\eta| < 0.8$ region.*

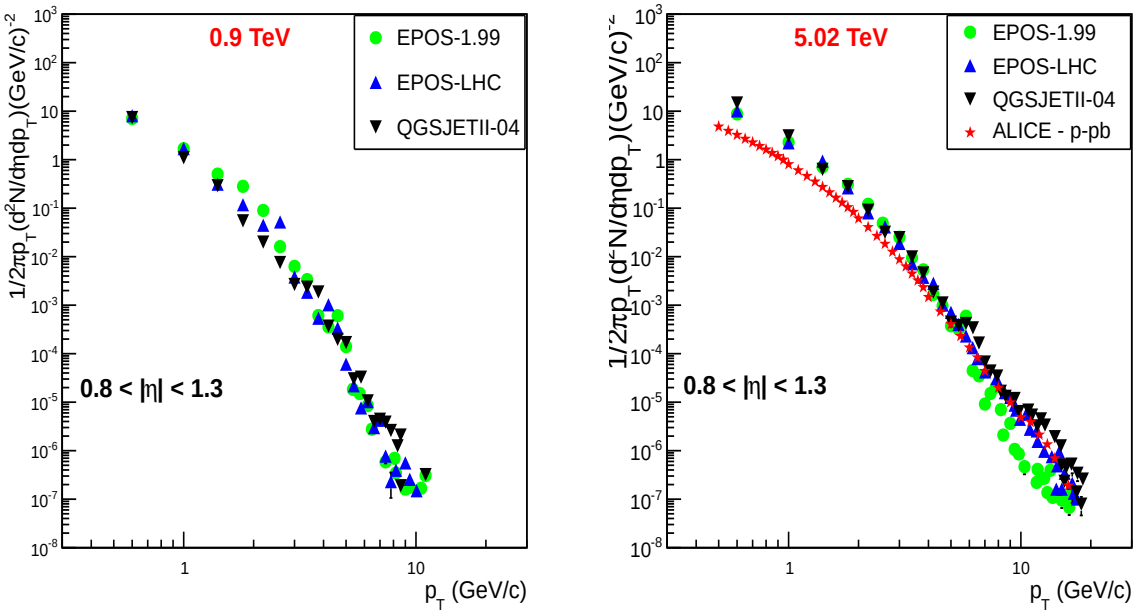

Figure 4.3: *p_T distributions in p-Pb collisions at $\sqrt{s_{NN}}$ = 0.9 TeV and 5.02 TeV in $0.8 < |\eta| < 1.3$ region.*

obtained using the simulations from EPOS-1.99, EPOS-LHC and QGSJETII-04 models and it is observed that at 0.9 TeV for $1.3 < |\eta| < 1.8$ these models are consistent up to $p_T \approx 3$ GeV/c and the multiplicity is steadily declining with some (statistical) fluctuation. We have also compared the simulation results obtained from the models with the CMS

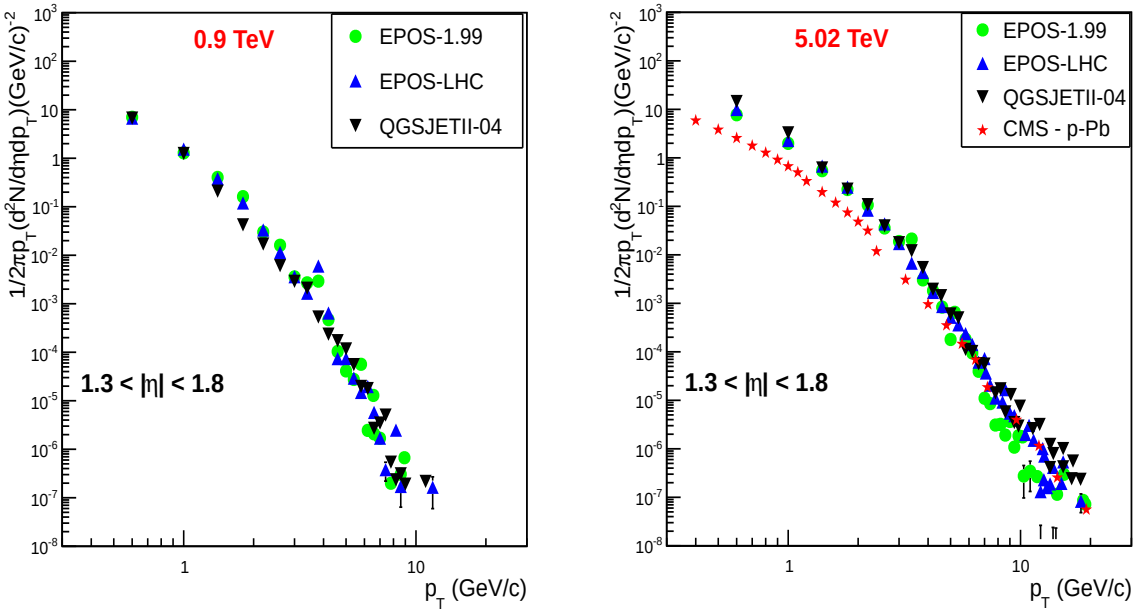

Figure 4.4: *p_T distributions in p-Pb collisions at $\sqrt{s_{NN}}$ = 0.9 TeV and 5.02 TeV in $1.3 < |\eta| < 1.8$ region.*

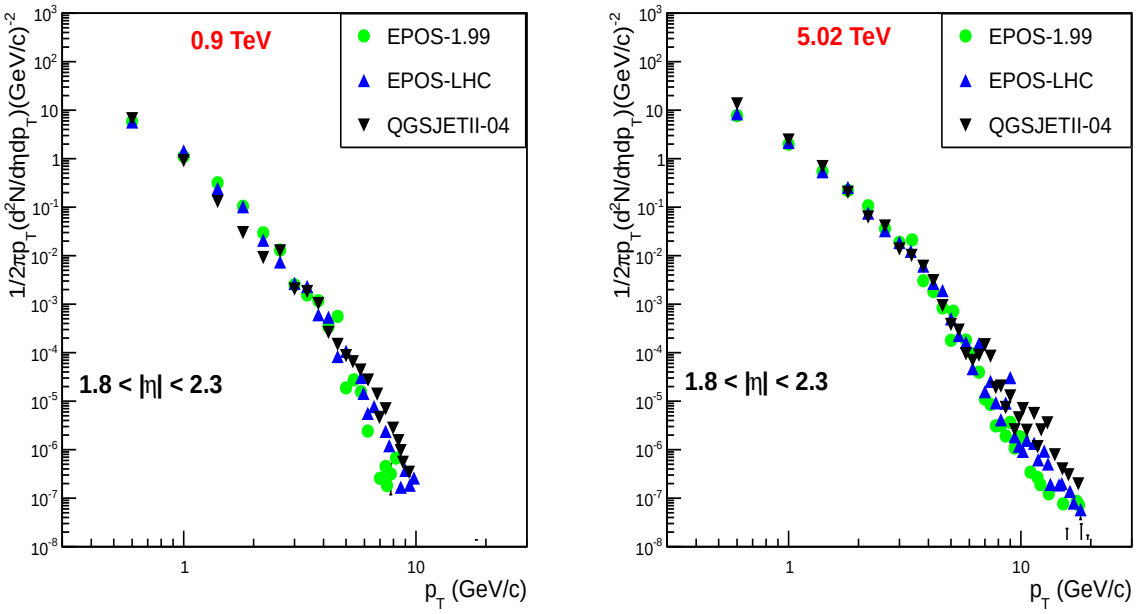

Figure 4.5: *p_T distributions in p-Pb collisions at $\sqrt{s_{NN}}$ = 0.9 TeV and 5.02 TeV in $1.8 < |\eta| < 2.3$ region.*

experimental data.

For very forward $|\eta|$ - region, $1.8 < |\eta| < 2.3$, EPOS-1.99, EPOS-LHC and QGSJETII-04 models seem to be consistent with each other up to $p_T \approx 5$ GeV/c for 0.9 TeV and 5.02 TeV after that QGSJETII-04 model gives predictions of higher multiplicity as compared

to the other two models. The overall distributions shows that the models can not explain experimental data in low p_T region where the models predictions are systematically overestimated as compared to the experimental data while in higher p_T region, the models can describe experimental data very well. We think that the reason of this observed Cronin effect at low p_T region could be multiple particle interactions because low energy particles will interact more frequently than those at higher energy. Therefore we can see that in models this probability is more than that of the experiments. Similarly decreasing the probability of multiple particle interactions for the low energy particles could mean that the models can not take into account the collective interactions of partons. As these models are parton based, therefore in high p_T region where parton interactions are dominant, their production coincides with experimental data very well.

4.1.2 Observation of universality for high p_T distribution at LHC energies

Differential yield versus p_T are investigated for the primary charged particles in the $|\eta|$ - regions, $0.3 < |\eta| < 0.8$, $0.8 < |\eta| < 1.3$ and $1.3 < |\eta| < 1.8$ as shown in Fig. (4.6). We have compared the HIJING-1.0 and UrQMD-3.4 results with CMS [184] as well as ATLAS [185]. We are using Y_{exp}, Y_{HIJ} and Y_{UrQ} for the yields coming from the experimental data, HIJING model and UrQMD model, respectively. There are two prominent regions in Fig. (4.6) (top left): region - I for $p_T < 1.3$ GeV/c; and region - II for $p_T > 1.3$ GeV/c. In region - I, the behavior of the yields as a function of p_T is different and we have $Y_{exp} > Y_{HIJ} > Y_{UrQ}$ and the ratios $R_{HIJ} > R_{UrQ}$ ($R_{HIJ} = Y_{HIJ}/Y_{exp}$ and $R_{UrQ} = Y_{UrQ}/Y_{exp}$) are less than 1 and increase weakly with p_T. In region - II, it is observed that $Y_{exp} \simeq Y_{HIJ} \simeq Y_{UrQ}$. So in this region, one can see that the behavior of the yields do not depend upon model definitions. Differential yields as a function of p_T are studied in the pseudorapidity region, $0.8 < \eta < 1.3$ as shown in Fig. (4.6) (top right), where again two p_T regions can be noted: region - I for $p_T < 8.2$ GeV/c and region - II for $p_T > 8.2$ GeV/c. In region - I the behaviors of the yields are different, one can see that $Y_{exp} > Y_{HIJ} > Y_{UrQ}$. In region - II, $Y_{exp} \simeq Y_{HIJ} \simeq Y_{UrQ}$. Similarly the differential yields as a function of p_T in the pseudorapidity region, $1.3 < \eta < 1.8$ are studied which is shown in Fig. (4.6) (bottom). One can see that there are also two p_T regions for the primary charged particles, region - I is for $p_T < 6.2$ GeV/c while region - II is for $p_T > 6.2$ GeV/c.

In region - I, the yields as a function of p_T are again different with $Y_{exp} > Y_{HIJ} > Y_{UrQ}$, and for region - II, we have $Y_{exp} \simeq Y_{HIJ} \simeq Y_{UrQ}$. In Fig. (4.6), the low p_T regions are connected with the leading particles or projectile fragmentation. Also, there is a difference of yield distribution at low p_T regions and simulated data is lower than the experimental data. Region II is a newly investigated region where simulated results are

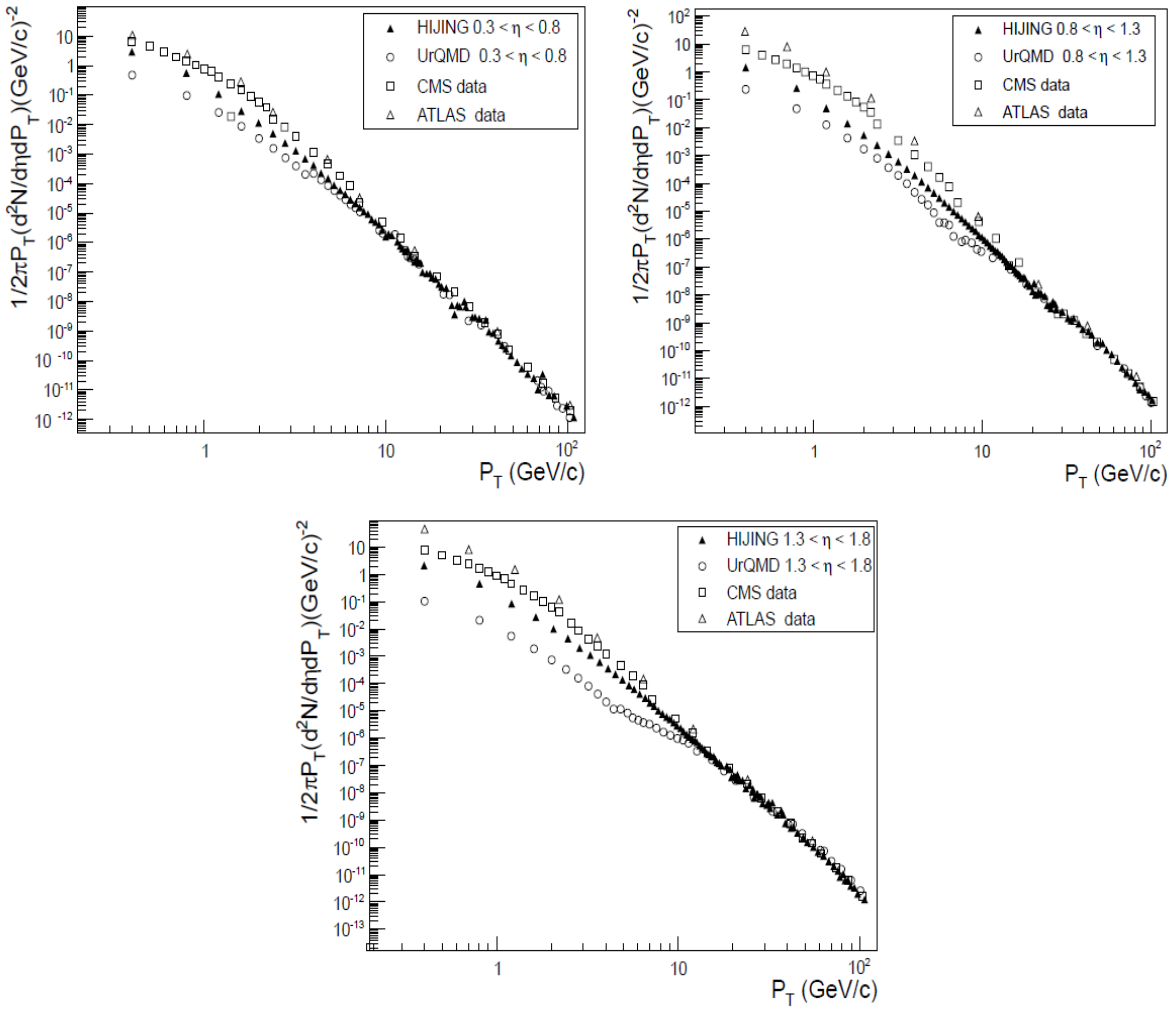

Figure 4.6: *p_T distributions of the primary charged particles produced in p-Pb collisions at $\sqrt{s_{NN}} = 5.02$ TeV in the $0.3 < \eta < 0.8$, $0.8 < |\eta| < 1.3$ and $1.3 < |\eta| < 1.8$ regions.*

almost the same as that of experimental predictions. In Fig. (4.7) (top left), the ratios $R_{HIJ} \simeq R_{UrQ} \simeq 1$ do not depend upon p_T as well as on models. In Fig. (4.7) (top right), with $0.8 < |\eta| < 1.3$, the ratios of R_{HIJ} and R_{UrQ} are less than 1, and again a little onward do not depend on p_T, where $R_{HIJ} \simeq R_{UrQ}$. The ratios R_{HIJ} and R_{UrQ} increase weakly with p_T, being around 1, almost independent of model codes. The ratios of $R_{HIJ} > R_{UrQ}$ are less than 1 and also do not depend on p_T. Similarly in Fig. (4.7) (bottom), shows that $R_{HIJ} \simeq R_{UrQ} \simeq 1$ do not depend on p_T. Again, we see some universality in the behavior of p_T distribution. While the ratios of the outcome from HIJING model to ATLAS data and UrQMD to ATLAS data are suppressed in three $|\eta|$ - regions at low p_T values, at high p_T values, they do not depend on the models.

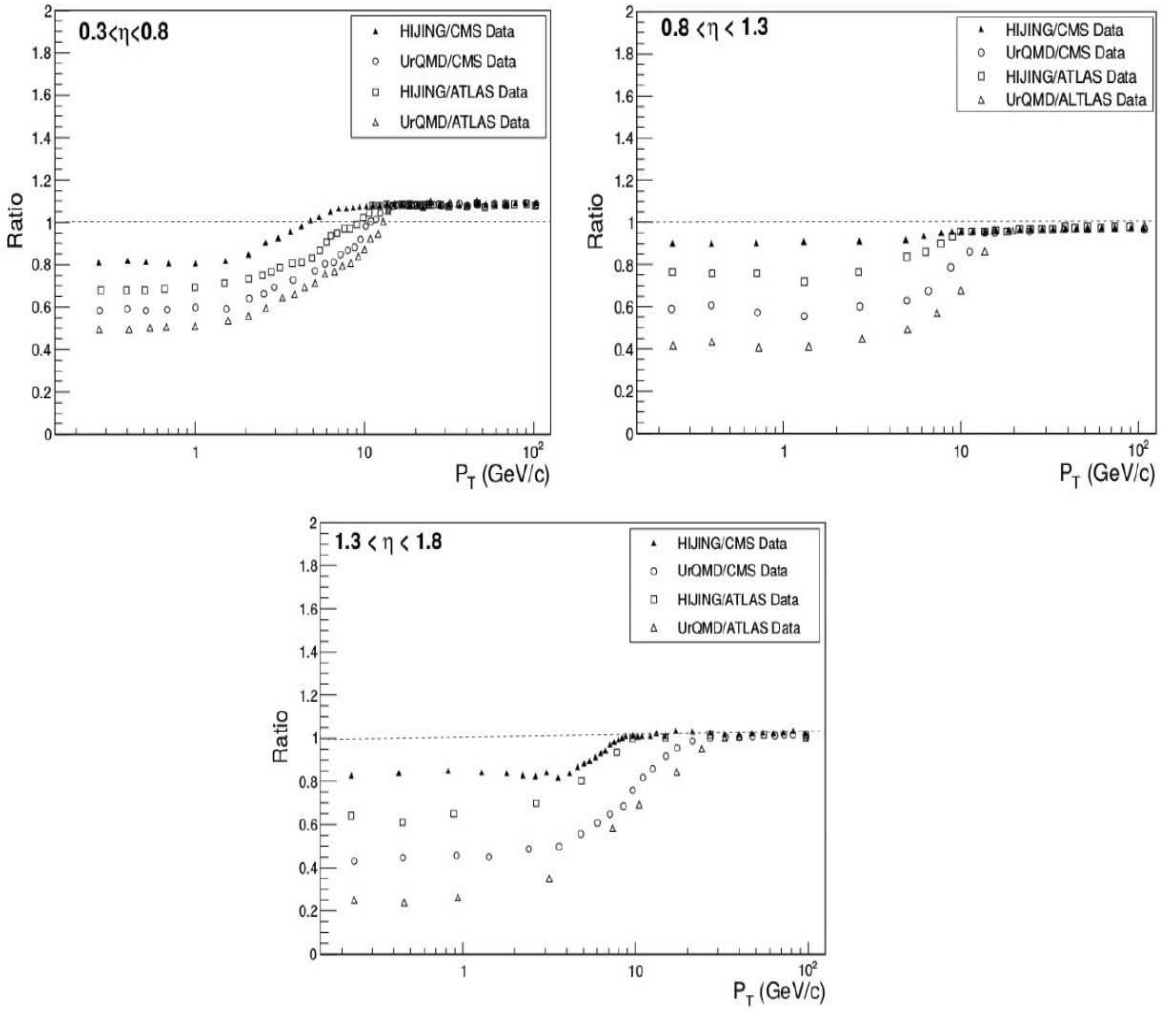

Figure 4.7: *Ratios of models to the experiment at* $\sqrt{s_{NN}} = 5.02$ *TeV in the* $0.3 < |\eta| < 0.8$, $0.8 < |\eta| < 1.3$ *and* $1.3 < |\eta| < 1.8$ *regions.*

4.1.3 Study of p_T distributions and Nuclear Modification factor of Charged particles Production in *p-Pb* Interactions at LHC Energies

In these simulations, we have used, HIJING-1.0 and UrQMD-3.4 models. We considered the same primary charged particles in the analysis: protons, anti-protons, K^+, K^-, π^+ and π^- based on the HIJING-1.0 and UrQMD-3.4 code definitions. This simulation is done for the $|\eta|$ - regions: $|\eta| < 0.3$, $0.3 < |\eta| < 0.8$ and $0.8 < |\eta| < 1.3$ in the transverse momentum range $0 < p_T < 20$ GeV/c with 150k events simulated from HIJING-1.0 and UrQMD-3.4 models each and compared them with ALICE data [186].

Figure (4.8), shows the invariant yield of charged particles in central pseudorapidity region $|\eta| < 0.3$, at 0.9 and 5.02 TeV. The yield of charged particles production at 5.02 TeV is compared to ALICE data. HIJING model describes the experimental data very well for $1 < p_T < 3$ GeV/c and gives multiplicities values higher than the experimental data for

$p_T > 3$ GeV/c. But in case of UrQMD, the data points have lower multiplicities than the experimental data points for, $0.3 < p_T < 2.5$ GeV/c, and after that UrQMD data points have a bit higher values of multiplicities. It is observed that for small interval of p_T i.e. $7 < p_T < 15$ GeV/c the model predictions match very well with the experimental data points and for $p_T > 15$ GeV/c it has lesser multiplicity. One can see the universality in the behavior of p_T distribution that can be due to a nuclear transparency effects or can better be described through the leading particle effects. A suppression in the UrQMD distribution is connected with the medium effects as can be seen clearly at 0.9 TeV energy (left panel). The comparison of HIJING and UrQMD distributions matches with each other for $p_T > 3$ GeV/c.

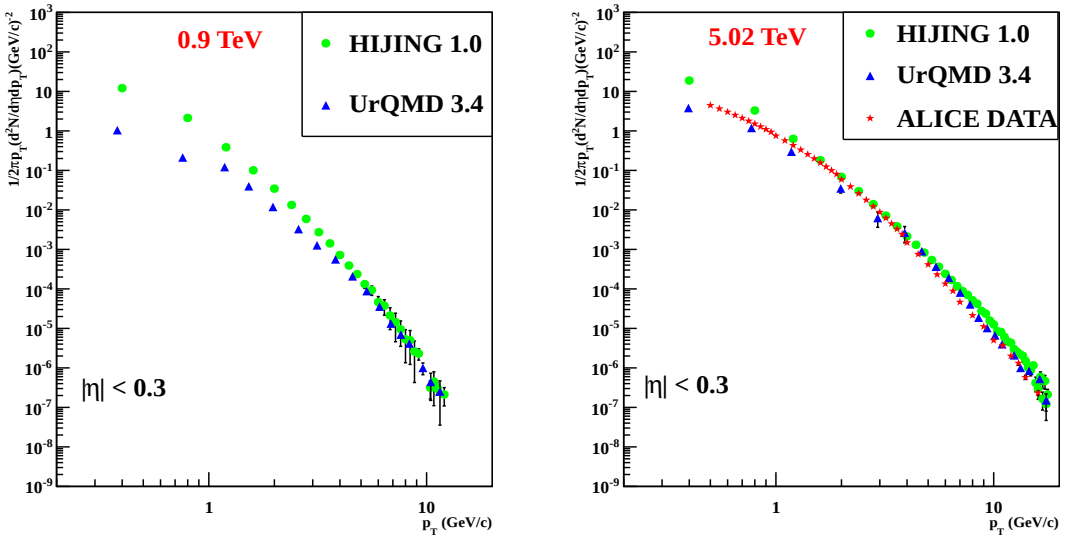

Figure 4.8: *p_T distributions of the primary charged particles for the pseudorapidity region of $|\eta| < 0.3$ from the simulated data obtained from the HIJING - 1.0 and UrQMD - 3.4 codes.*

Figure (4.9), shows the invariant differential yield of charged particles in mid-pseudorapidity region, $0.3 < |\eta| < 0.8$. It seems that the HIJING model can describe the experimental data very well for $0.4 < p_T < 1$ GeV/c, but gives lower multiplicity for $1 < p_T < 1.2$ GeV/c and experimental data points have higher multiplicity in this region. While it is observed that HIJING and UrQMD can better describe the experimental data points for higher p_T values. It is also observed that the UrQMD distributions get closer to experimental and HIJING distributions, for $0.3 < |\eta| < 0.8$. The comparison of HIJING and UrQMD distributions shows that they match with each other for $p_T > 2$ GeV/c. The yield of charged particles also decreases while moving from $|\eta| < 0.3$, to $0.3 < |\eta| < 0.8$.

Similarly, in Fig. (4.10), HIJING model describes the experimental data for large p_T region of $0.4 < p_T < 5$ GeV/c and for other p_T values the data points are higher multiplicity. UrQMD model predictions are lower multiplicity for $p_T < 5$ GeV/c and higher multiplicity for $p_T > 5$ GeV/c. In case of 0.9 TeV energy, the comparison of two model

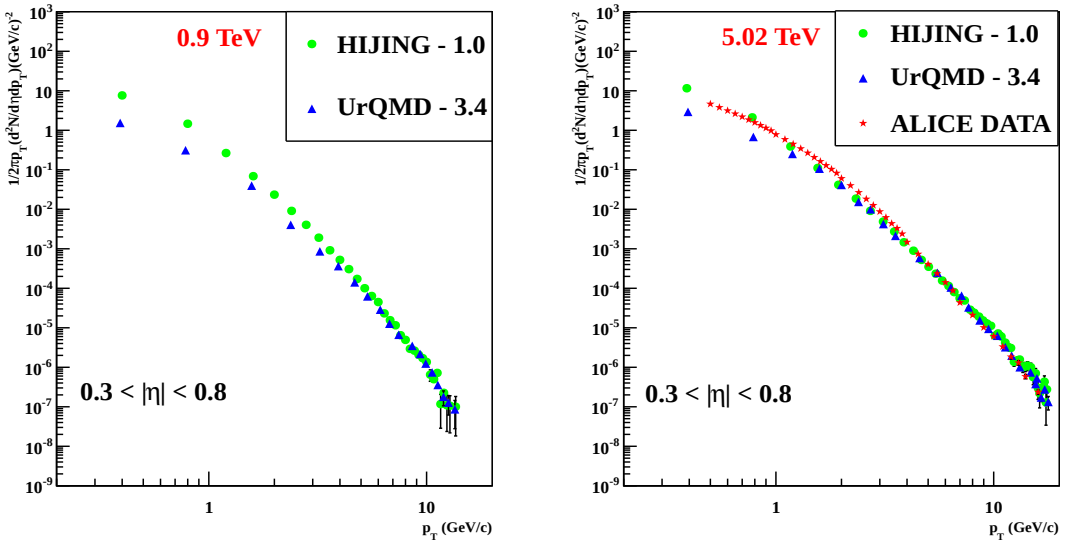

Figure 4.9: *p_T distributions of the primary charged particles for the pseudorapidity region of $0.3 < |\eta| < 0.8$ from the simulated data obtained from the HIJING - 1.0 and UrQMD - 3.4 codes.*

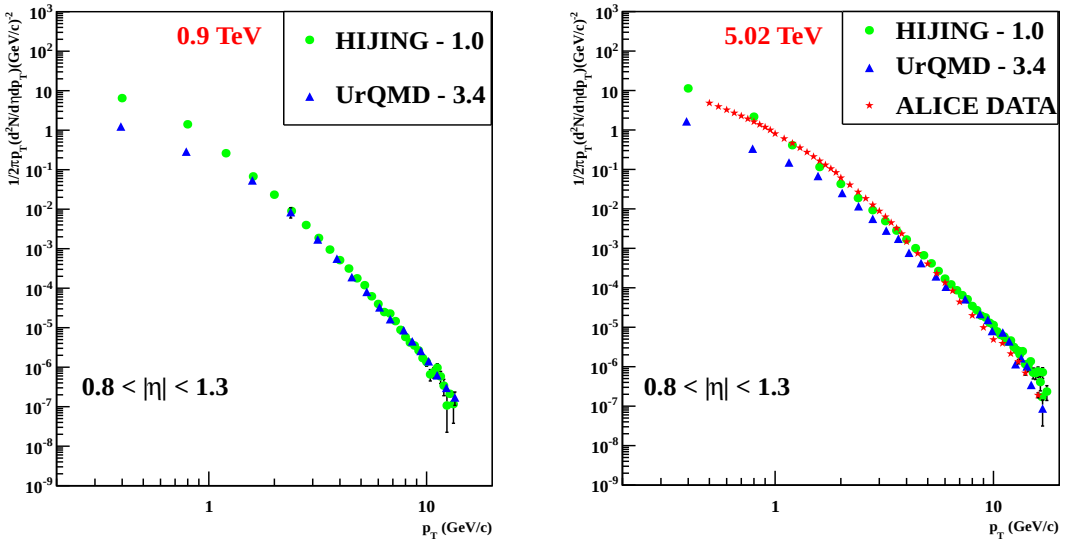

Figure 4.10: *p_T distributions of the primary charged particles for the pseudorapidity region of $0.8 < |\eta| < 1.3$ from the simulated data obtained from the HIJING - 1.0 and UrQMD - 3.4 codes.*

distributions depict that the data points are matching each other for $p_T > 1.5$ GeV/c and yield decreases for most forward $|\eta|$ - region. Figure (4.11), shows the ratio of p_T spectra for forward $|\eta|$ - region of $0.3 < |\eta| < 0.8$, to central $|\eta|$ - region of $|\eta| < 0.3$. Left panel in Fig. (4.11), at 0.9 TeV, shows that both models follow the same trend and are higher at high p_T values and lower at low p_T values, while the UrQMD models gives a distribution which is lower as compared to the HIJING results due to the medium effects.

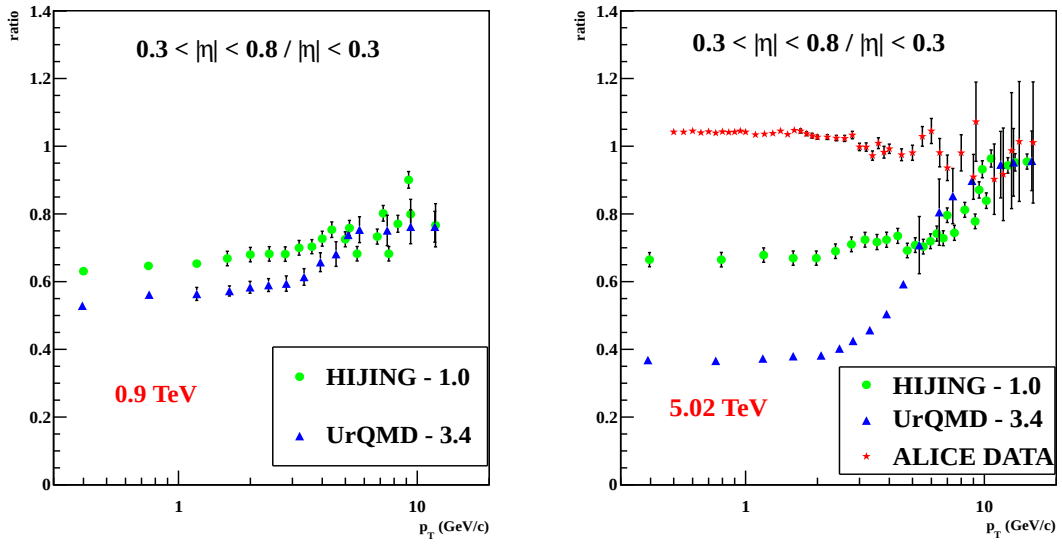

Figure 4.11: *Ratio distribution as a function of p_T of the primary charged particles at $\sqrt{s_{NN}}$ = 0.9 and 5.02 TeV for the pseudorapidity interval of 0.3 < |η| < 0.8/|η| < 0.3 and 0.8 < |η| < 1.3/|η| < 0.3.*

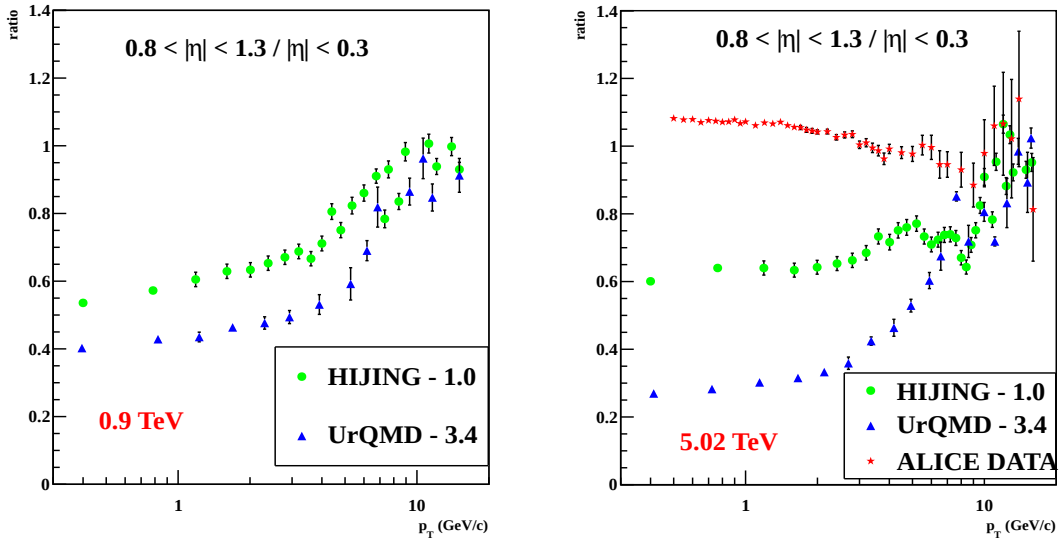

Figure 4.12: *Ratio distribution as a function of p_T of the primary charged particles at $\sqrt{s_{NN}}$ = 0.9 and 5.02 TeV for the pseudorapidity interval of 0.3 < |η| < 0.8/|η| < 0.3 and 0.8 < |η| < 1.3/|η| < 0.3.*

At 5.02 TeV energy as shown in right panel of Fig. (4.11), both model distributions are lower as compared to ALICE data at low p_T values. However the universality behavior is visible at high p_T region where all the three data points coming from experimental data and model data coincide with each other. The universality is connected with the leading particle effect. Figure (4.12), shows the ratio of p_T spectra for most forward $|\eta|$ - region of $0.8 < |\eta| < 1.3$ to central $|\eta|$ - region of $|\eta| < 0.3$, also follow the same trend as in the

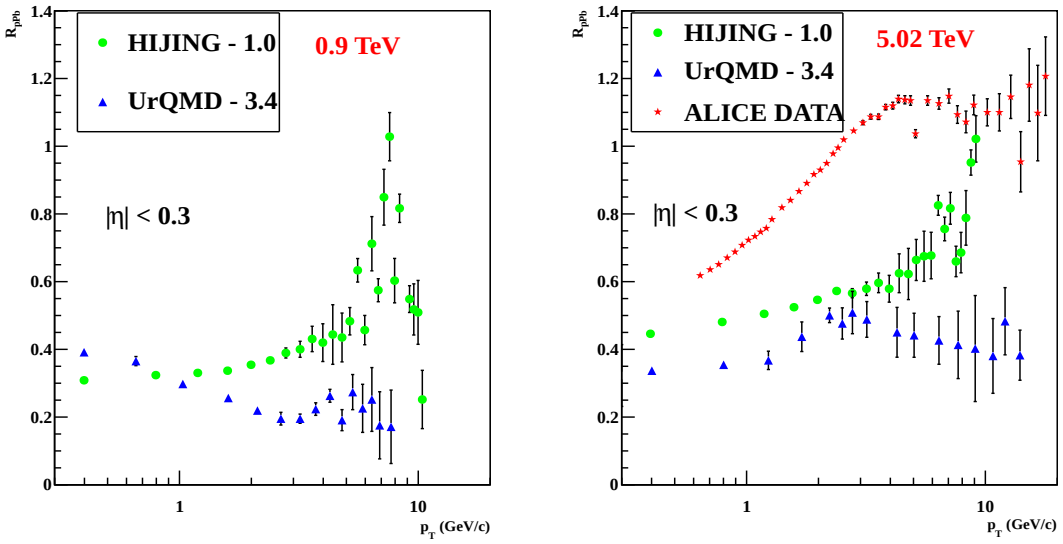

Figure 4.13: *R_{pPb} distribution as a function of p_T of the primary charged particles at $\sqrt{s_{NN}}$ = 0.9 and 5.02 TeV for the pseudorapidity interval of $|\eta| < 0.3$.*

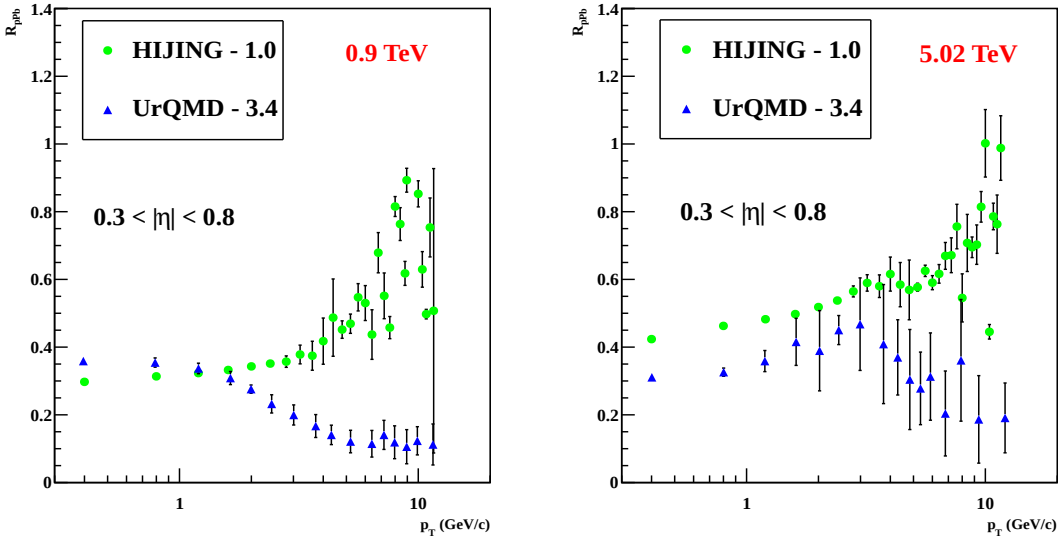

Figure 4.14: *R_{pPb} distribution as a function of p_T of the primary charged particles at $\sqrt{s_{NN}}$ = 0.9 and 5.02 TeV for the pseudorapidity interval of $0.3 < |\eta| < 0.8$.*

case of Fig. (4.11).

Figure (4.13), shows the R_{pPb} calculated using HIJING and UrQMD models and compared to the ALICE data at 5.02 TeV. The left panel in Fig. (4.13), shows that the value of R_{pPb} is less than 1, showing the suppression in data points. But at p_T region of $5 < p_T < 10$ GeV/c, one can first observe the increasing and then decreasing trend. When compared with ALICE data, it is seen that HIJING model does not show any energy loss while UrQMD data shows a suppression in signal at high p_T values. Similarly, R_{pPb}

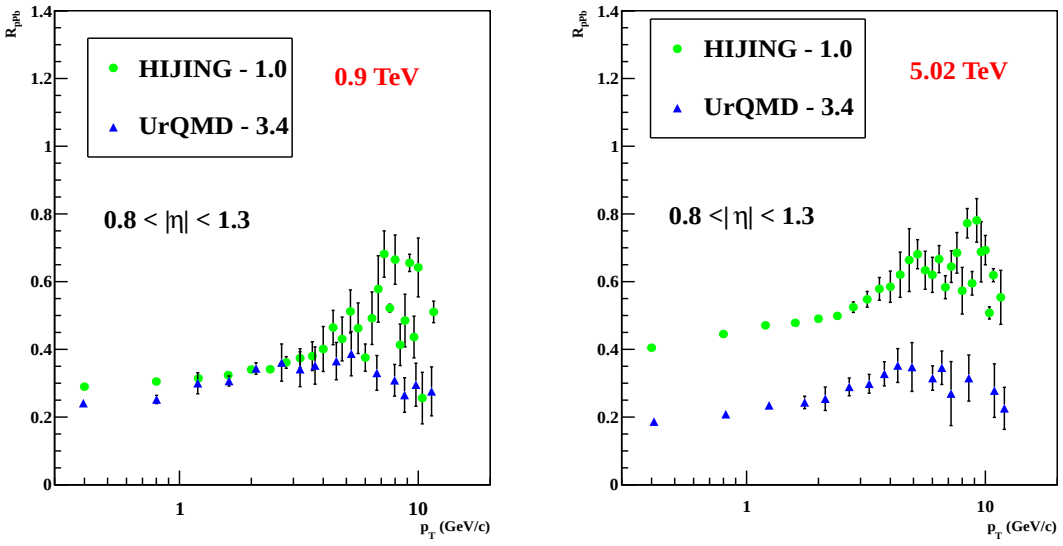

Figure 4.15: *R_{pPb} distribution as a function of p_T of the primary charged particles at $\sqrt{s_{NN}}$ = 0.9 and 5.02 TeV for the pseudorapidity interval of 0.8 < |η| < 1.3.*

distribution for forward and most forward $|\eta|$ - regions at two LHC energies of 0.9 TeV and 5.02 TeV are shown in Fig. (4.14) and (4.15). This clearly shows that the R_{pPb} distribution for the most forward $|\eta|$ - regions are more suppressed as compared to the forward $|\eta|$ - region.

4.1.4 Models prediction of transverse momentum and nuclear modification factor distributions of the charged particles in *p+Pb* collisions at $\sqrt{s_{NN}}$ = 5.02 TeV and $\sqrt{s_{NN}}$ = 7 TeV

For the analysis we again choose primary charged particles like protons, anti-protons, K^+, K^-, π^+ and π^- based on EPOS-1.99, QGSJETII-04 and EPOS-LHC code definitions. In this work, we have studied the p_T spectra and Nuclear Modification Factor, R_{pPb} distributions of the charged particles in p-Pb collisions at $\sqrt{s_{NN}}$ = 5.02 TeV. For the R_{pPb}, we have also simulated pp collision at $\sqrt{s_{NN}}$ = 5.02 TeV.

Figure (4.16), shows the comparison of p_T distribution of particles in minimum bias p-Pb collisions. Figures (4.17-4.19), show the comparison of p_T distributions of particles in minimum bias pp collisions. Figure (4.20) shows the comparison of ratio of kaons to pions and protons to pions distributions in minimum bias p-Pb collisions at $\sqrt{s_{NN}}$ = 5.02 TeV.

Figure (4.21) shows the comparison of NMF distribution of particles in minimum bias p-Pb collisions. This simulation is done for the mid-rapidity region -0.5 < |y| < 0 with 150k events simulated from EPOS-1.99, EPOS-LHC and QGSJETII-04 models and compared

with the ALICE data [187].

Figure (4.16), shows the p_T distributions of the primary charged particles such as pions, anti-pions, kaons, anti-kaons, protons and anti-protons in minimum bias p-Pb collisions for the mid-rapidity region: -0.5 < $|y|$ < 0, at $\sqrt{s_{NN}}$ = 5.02 TeV from EPOS-1.99, EPOS-LHC and QGSJETII-04 models. Figure (4.16), shows that all the three models distribution are in good agreement with each other but get overestimated with the experimental data.

Figures (4.17-4.19), shows the p_T distributions of the charged particles such as pions, anti-pions, kaons, anti-kaons, protons and anti-protons in pp collisions for the rapidity region: $|y| < 0.8$, at $\sqrt{s_{NN}}$ = 5.02 TeV and 7 TeV. The distributions gives overestimated behavior as compared with the experimental data but have nearly similar behaviour.

Figure (4.20), shows the ratio distributions of kaons plus anti-kaons to pions plus anti-pions and protons plus anti-protons to pions anti-pions in minimum bias p-Pb collisions at $\sqrt{s_{NN}}$ = 5.02 TeV. Figure (4.20) (left), shows that EPOS-LHC is in good agreement with the experimental data as compared to the other two models, i.e. EPOS-1.99 and QGSJETII-04.

Figure (4.21), shows the R_{pPb} distributions of pions, anti-pions, kaons, anti-kaons, protons and anti-protons in minimum bias p–Pb collisions at $\sqrt{s_{NN}}$ = 5.02 TeV. The figure shows that for (anti) pions, (anti) kaons and (anti) protons the models distribution is around 1. One can see that at low p_T, the predictions from the models are the same up to 3 GeV/c but these predictions get different in the high p_T, regions. We see that as compared to the EPOS-1.99 and QGSJETII-04 model the EPOS-LHC can describe the experimental data very well.

For $\pi^+ + \pi^-$ mesons, models can not describe the experimental data in the region of p_T < 2 GeV/c. This results could be connected with that the pions at low p_T absorbed by the medium weakly than it is expected from the models. At intermediate p_T, the (anti) proton, R_{pPb} shows Cronin-like enhancement while pions and kaons shows no nuclear modifications. Main things coming from Fig. (4.21), is that there is not any suppression so there is no QGP forming in p-Pb collisions.

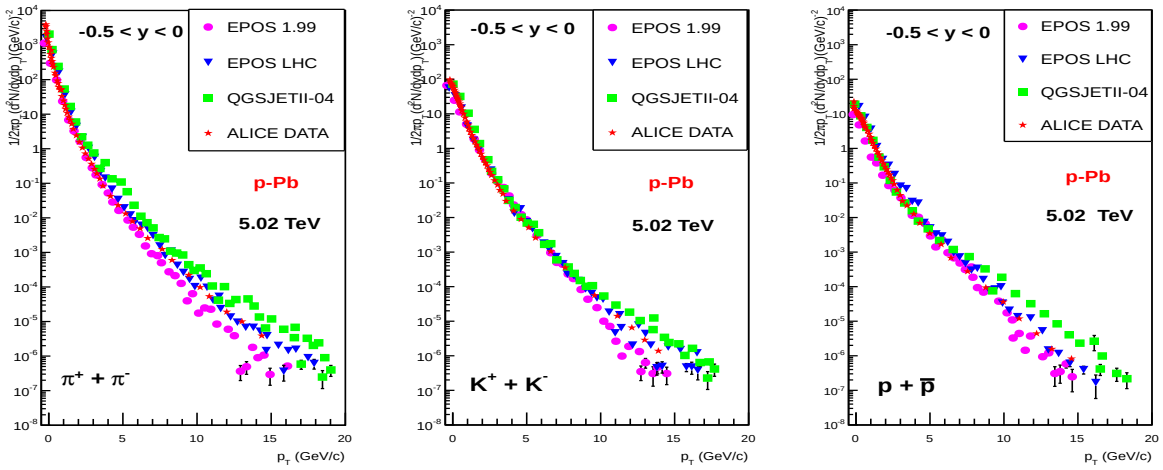

Figure 4.16: *p_T distributions of the charged particles in -0.5 < |y| < 0 at $\sqrt{s_{NN}}$ = 5.02 TeV from the EPOS-1.99, EPOS-LHC and QGSJETII-04 Models. ALICE data is also plotted for comparison with transverse momentum distribution at 5.02 TeV.*

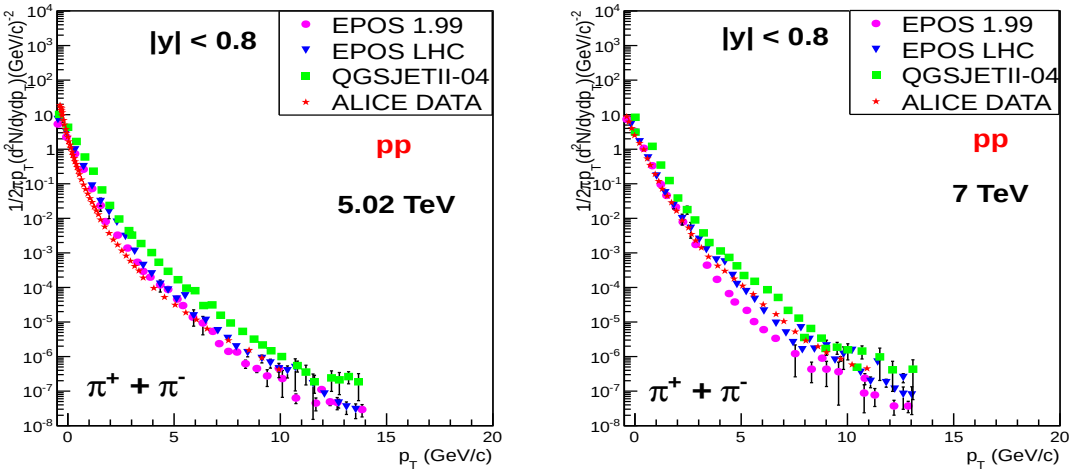

Figure 4.17: *p_T distributions of the charged particles of pions in -0.5 < |y| < 0 at $\sqrt{s_{NN}}$ = 5.02 TeV and 7 TeV from the EPOS-1.99, EPOS-LHC and QGSJETII-04 Models. ALICE data of pp is also plotted for comparison with transverse momentum distribution at 5.02 TeV and 7 TeV.*

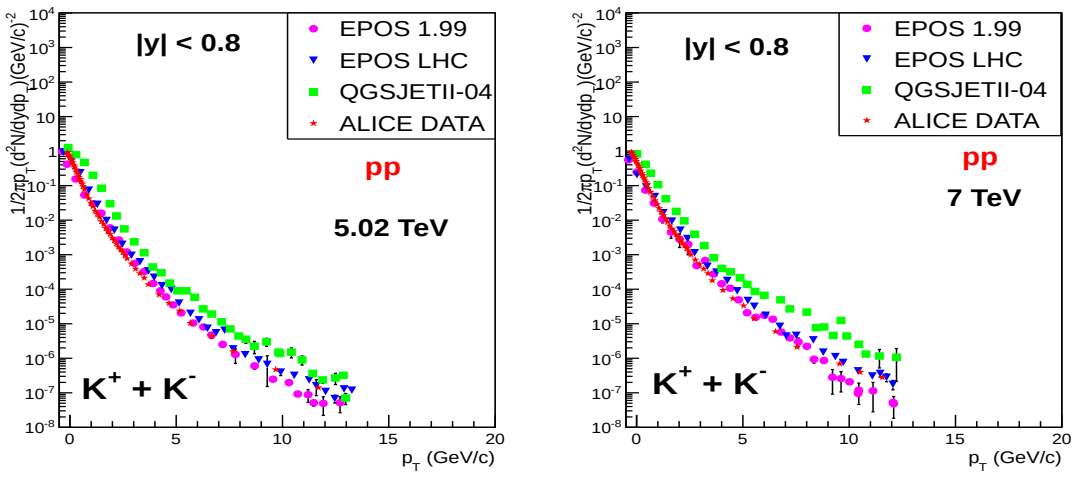

Figure 4.18: *p_T distributions of the charged particles of kaons in -0.5 < |y| < 0 at $\sqrt{s_{NN}}$ = 5.02 TeV and 7 TeV from the EPOS-1.99, EPOS-LHC and QGSJETII-04 Models. ALICE data of pp is also plotted for comparison with transverse momentum distribution at 5.02 TeV and 7 TeV.*

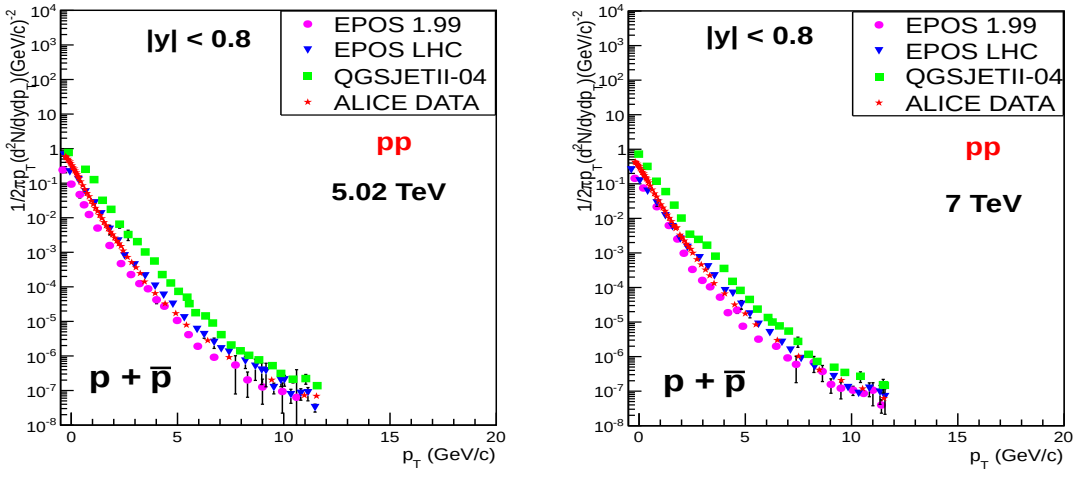

Figure 4.19: *p_T distributions of the charged particles of (anti) protons in -0.5 < |y| < 0 at $\sqrt{s_{NN}}$ = 5.02 TeV and 7 TeV from the EPOS-1.99, EPOS-LHC and QGSJETII-04 Models. ALICE data of pp is also plotted for comparison with transverse momentum distribution at 5.02 TeV and 7 TeV.*

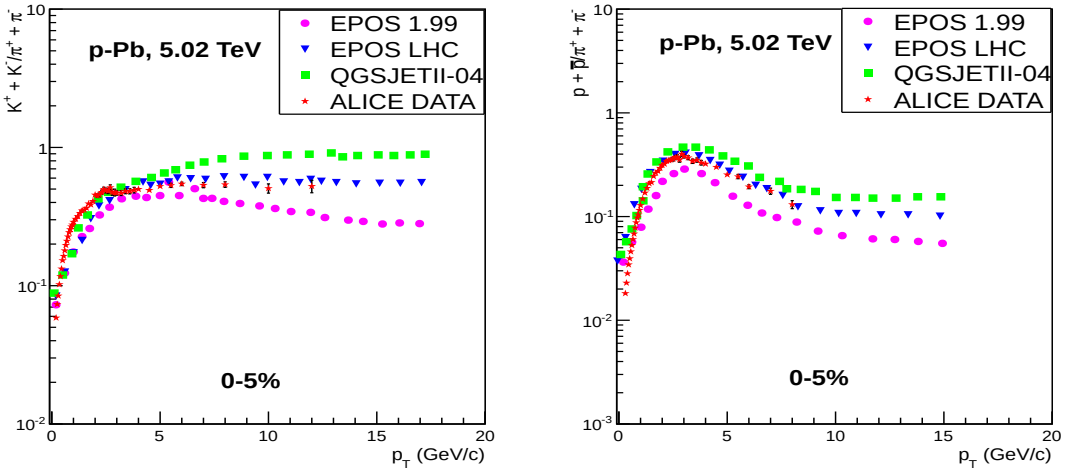

Figure 4.20: *Ratio distribution of kaons to pions and (anti) proton to pions of charged particles in -0.5 < |y| < 0 at $\sqrt{s_{NN}}$ = 5.02 TeV from the EPOS-1.99, EPOS-LHC and QGSJETII-04 Models. ALICE data is also plotted for comparison at 5.02 TeV.*

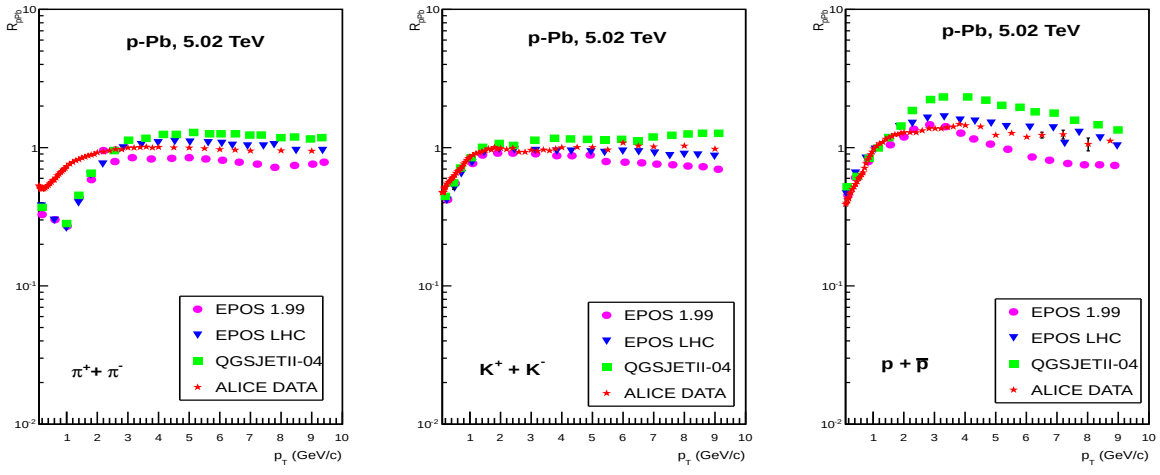

Figure 4.21: *Nuclear modification factor distribution for pions, kaons and protons of the charged particles at $\sqrt{s_{NN}}$ = 5.02 TeV from the EPOS-1.99, EPOS-LHC and QGSJETII-04 Models. ALICE data is also plotted for comparison at 5.02 TeV.*

Chapter 5

Results and Discussion (Part-II)

5.1 pp collisions

In this chapter we have studied pp collisions as they are considered as a baseline to understand p-Pb and Pb-Pb collisions. In order to quantify the R_{pPb}, the study of pp collisions is very necessary. Therefore the pp collision play a key role in heavy ion collisions for reference.

5.1.1 Distributions of charged particles transverse momentum and pseudo-rapidity in pp collisions at 0.9 TeV

In our simulations, we have studied charged particle multiplicity dependence on p_T spectra and η - distributions in pp collisions at $\sqrt{s} = 0.9$ TeV. We have used EPOS-1.99, EPOS-LHC, QGSJETII-04 and SIBYLL-2.3c models to obtain the simulated data. We have simulated 100k events. In order to check the rationale of our simulations results obtained from these models, we have compared the simulated data with the experimental data of ATLAS experiment at LHC at 0.9 TeV for pseudorapidity (η) region $|\eta| < 2.5$ [188]. Figure (5.1), shows the comparison of charged particle multiplicity distributions as a function of p_T in pp collisions for the pseudorapidity interval of $|\eta| < 2.5$ at $\sqrt{s} = 0.9$ TeV. The ratio of simulated data to experimental data is also plotted in Fig. (5.1). It seems that SIBYLL-2.3c predictions are closer to the experimental data up to $p_T \sim 0.4$ GeV/c and EPOS-1.99 predictions are closer to the experimental data for $0 < p_T < 1.5$ GeV/c. QGSJETII-04 overestimate in the p_T range $2.5 < p_T < 6$ GeV/c while at high p_T values, EPOS-LHC and SIBYLL-2.3c overestimate, while rest of the models underestimate the experimental data. Figure (5.2), shows the distribution of charged particles density. It is obvious from the Figs.(5.2) that QGSJETII-04 predictions are closer to the experimental data for $N_{ch} \sim 20$. EPOS-LHC and SIBYLL-2.3c overestimate, whereas QGSJETII-04

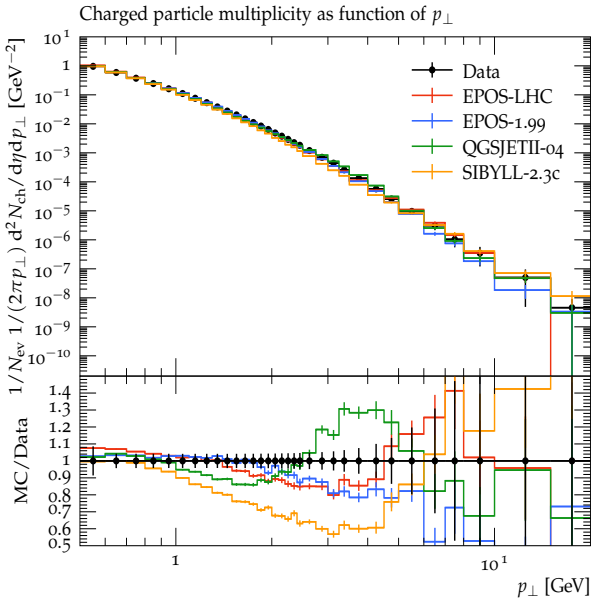

Figure 5.1: *Models' predictions of p_T - distributions of the differential yield of hadrons with $|\eta| < 2.5$ are compared with the ATLAS data. Filled circle is used to represent experimental data, solid blue line for EPOS–1.99, solid red line shows EPOS–LHC, solid green line shows the QGSJETII-04 and orange yellow shows the SIBYLL-2.3c model.*

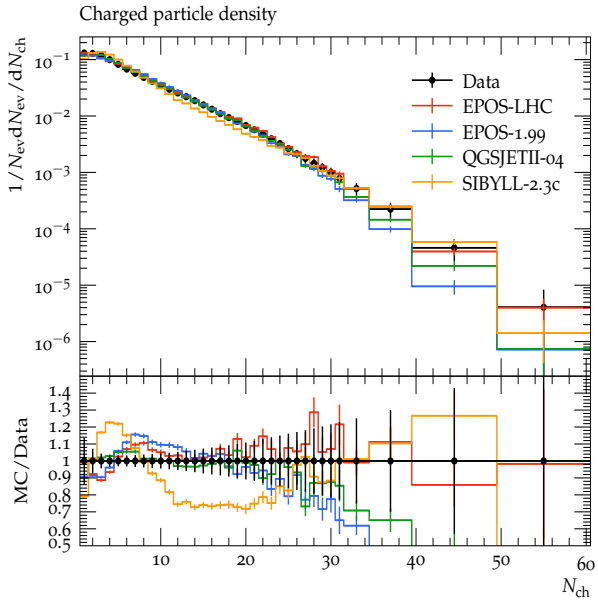

Figure 5.2: *Charged particles density as a function of charged particles produced in pp collisions with $|\eta| < 2.5$ at $\sqrt{s} = 0.9$ TeV from the EPOS–LHC, EPOS–1.99, QGSJETII-04 and SIBYLL-2.3c. ATLAS data with p_T distribution at 0.9 TeV is compared with models' predictions. Filled circle is used to represent experimental data, solid blue line for EPOS–1.99, solid red line shows EPOS–LHC, solid green line shows the QGSJETII-04 and orange yellow shows the SIBYLL-2.3c model..*

and EPOS-1.99 underestimate the experimental data at high N_{ch} values. Figure (5.3), shows the comparison of average p_T as a function of N_{ch} in minimum bias pp collisions. EPOS-LHC and SIBYLL-2.3c predictions are closer to the experimental data for $N_{ch} \sim$

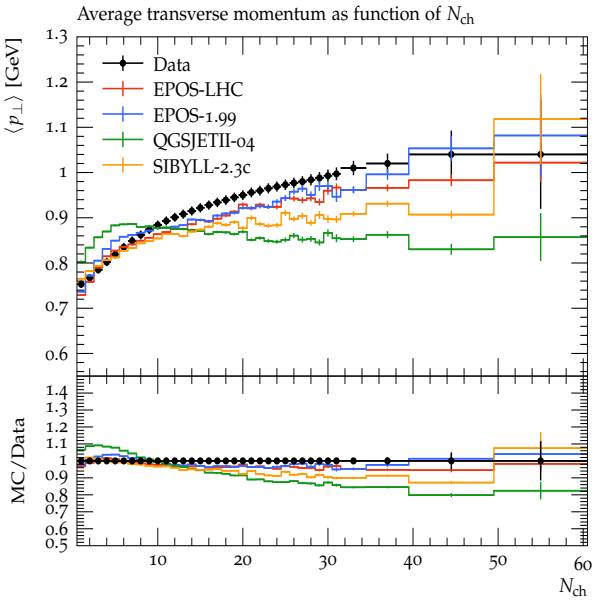

Figure 5.3: *Average p_T as a function of N_{ch} of the charged hadrons with $|\eta| < 2.5$ from the models given in legend. ATLAS data with p_T distribution at 0.9 TeV is compared with models predictions. Filled circle is used to represent experimental data, solid blue line for EPOS–1.99, solid red line shows EPOS–LHC, solid green line shows the QGSJETII–04 and orange yellow shows the SIBYLL–2.3c model.*

8. After that up to $N_{ch} \sim 40$ all of the models underestimate the experimental data and for $N_{ch} > 40$ QGSJETII-04 and SIBYLL-2.3c overestimate, while EPOS-1.99 and EPOS-LHC underestimate the experimental data.

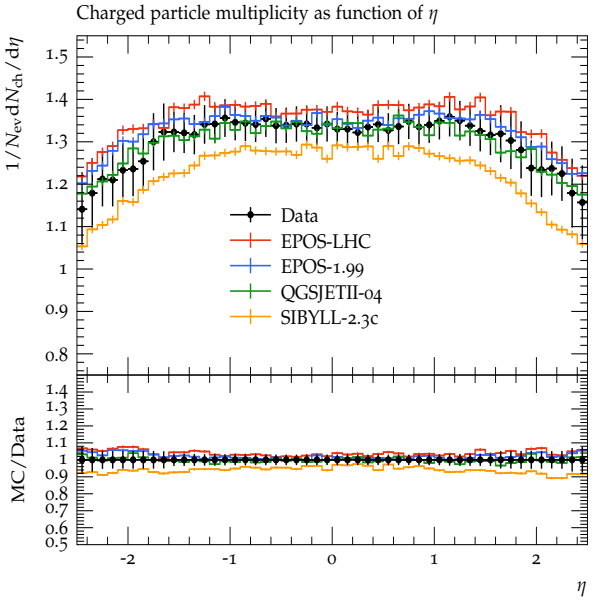

Figure 5.4: *$|\eta|$ - distribution of the charged hadrons with $|\eta| < 2.5$ produced in pp collisions at $\sqrt{s} = 0.9$ TeV from the EPOS–LHC, EPOS–1.99, QGSJETII–04 and SIBYLL-2.3c. ATLAS data with p_T distribution at 0.9 TeV is compared with models predictions.*

Figure (5.4), shows the charged particles pseudorapidity distribution and from the Figs.(5.4),

it is obvious that SIBYLL-2.3c underestimate the experimental data while EPOS-1.99 and EPOS-LHC overestimate the experimental data. QGSJETII-04 model predictions are closer to the behavior of distribution from the experimental data.

5.1.2 Study of Pseudorapidity and Transverse-Momentum Distributions of Charged Particles in pp Interactions at $\sqrt{s}$ = 13 TeV Using Hadron Production Models

We are reporting results on the study of selected charged particles produced in the pp interactions at $\sqrt{s} = 13$ TeV using simulated data obtained from Monte Carlo simulation codes: EPOS-1.99, EPOS-LHC and QGSJETII-04. This simulation is performed for the central pseudorapidity region of $|\eta| < 0.8$ in the transverse momentum range $0 < p_T < 20$ GeV/c with 150k events simulated from EPOS-1.99, EPOS-LHC and QGSJETII-04 models. For our analysis, we have selected primary charged particles like protons, anti-protons, K^+, K^-, π^+ and π^-. Figure (5.5), shows the p_T distributions obtained from simulated data and their comparison to the measurements of ALICE experiment for the pseudorapidity interval of $|\eta| < 0.8$. It is obvious that the EPOS-1.99 and QGSJETII-04 models are in good agreement with each other but do not describe the experimental data very well. Both models under predict the measurements of the experimental data. The EPOS-LHC model describes ALICE data very well over the entire range.

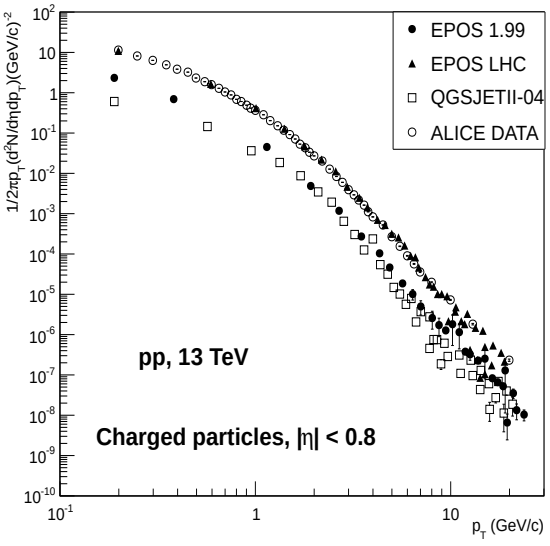

Figure 5.5: *p_T distributions of the charged particles produced in pp collisions at $\sqrt{s}$ = 13 TeV with $|\eta| < 0.8$ using EPOS-1.99, EPOS-LHC and QGSJETII-04 models compared with the ALICE experimental data. Vertical error bars in simulated data show statistical uncertainties.*

Figure (5.6), shows the ratio of p_T spectra of charged particles at $\sqrt{s} = 13$ TeV and 7 TeV. The published data at $\sqrt{s} = 7$ TeV is obtained from Ref. [189]. Figure(5.6), depicts

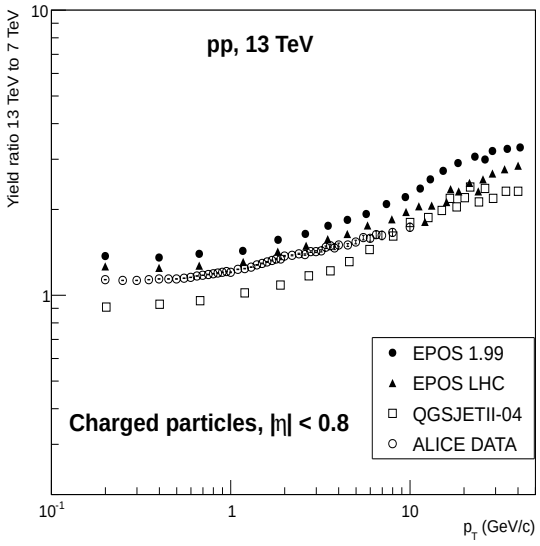

Figure 5.6: *Ratio distributions of the yield of the charged particles of 13 TeV to 7 TeV in* $|\eta| < 0.8$ *produced in pp collisions obtained from the EPOS-1.99, EPOS-LHC and QGSJETII-04 models compared with the ALICE measurements.*

the comparison of the ratio obtained from the models simulation to the ALICE data. It is clear from the figures that the EPOS-LHC can explain the experimental data very well as compared to the EPOS-1.99 and QGSJETII-04 models. Furthermore, the EPOS-1.99 overestimates while the QGSJETII-04 underestimates the spectra in comparison with that from the experimental data.

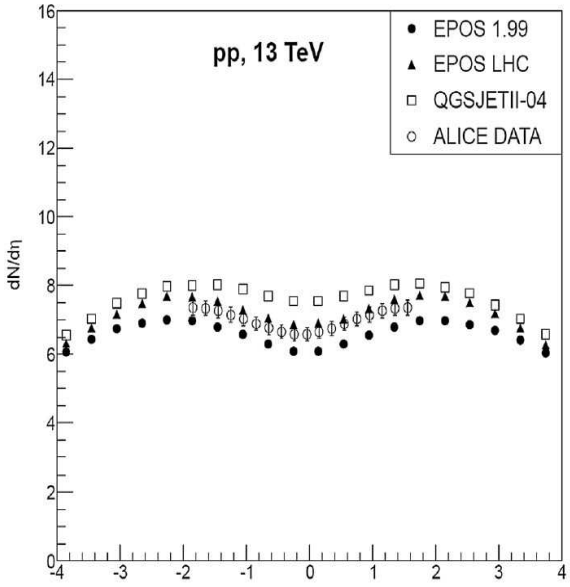

Figure 5.7: *Pseudorapidity distributions of the charged particles produced in pp collisions at* $\sqrt{s}$ *= 13 TeV with* $|\eta| < 0.8$ *obtained from the EPOS-1.99, EPOS-LHC and QGSETII-04 models compared with the measurements of ALICE.*

Figure (5.7), shows the pseudorapidity distributions obtained from the trios models and their comparison with the ALICE experimental data. It seems that the EPOS-LHC model can explain the experimental data very well as compared to the EPOS-1.99 and QGSJETII-04 model. EPOS-1.99 underestimates while QGSJETII-04 overestimates the the results as compared to those from the experimental data.

5.1.3 Distribution of Strange Particles' Transverse Momentum and Rapidity in High Energy Proton-Proton Collisions at $\sqrt{s}$ = 0.9 TeV at LHC

For the study of p_T and y of strange particles in pp collisions at $\sqrt{s}$ = 0.9 TeV, we have performed simulations, using EPOS-1.99, SIBYLL-2.3c, EPOS-LHC and QGSJETII-04 models. For the analysis, we have selected strange particles K^0_s, Λ and Ξ^- based on EPOS-1.99, SIBYLL-2.3c, EPOS-LHC and QGSJETII-04 code definitions. In our analysis, we studied p_T, rapidity and ratio distributions of the strange particles in pp collisions at $\sqrt{s}$ = 0.9 TeV. The models' predictions are compared with the CMS experimental data at $\sqrt{s}$ = 0.9 TeV [190]. This simulation is done for 150k events at $\sqrt{s}$ = 0.9 TeV simulated from EPOS-1.99, EPOS-LHC, SIBYLL-2.3c and QGSJETII-04 models.

Figure (5.8) shows the comparison of p_T distribution of the strange particles, K^0_s, Λ and Ξ^- in the p_T range $0 < p_T < 10$ GeV/c for the Non-Single Diffractive (NSD) of pp collisions. The p_T distribution of K^0_s shows that the experimental data is well explained by EPOS-LHC model in the lower p_T region of, $p_T < 0.3$ GeV/c as well as in the high p_T region of $p_T > 8$ GeV/c. The yields of particles from the EPOS-1.99, and QGSJETII-04 models are greater with respect to the experimental data for $p_T < 0.5$ GeV/c but becomes lower for $p_T > 0.5$ GeV/c. The predictions of SIBYLL-2.3c model underestimate the result as compared to the experimental data in lower as well as at high p_T ranges. The p_T distribution of Λ shows that QGSJETII-04 model explains the experimental data very well in the p_T regions, $2.5 < p_T < 3$ GeV/c and $3.5 < p_T < 4$ GeV/c. The yields of particles in the EPOS-1.99 models is greater with respect to the experimental data in the range $p_T < 0.6$ GeV/c but becomes lower in the range $p_T > 0.6$ GeV/c up to $p_T <$ 2.5 GeV/c. The predictions of EPOS-1.99 model is compatible with the experimental data in the p_T range $2.5 < p_T < 2.8$ GeV/c. The deviation between the EPOS-LHC and SIBYLL-2.3c models with the experimental data are maximum at lower as well as at higher p_T ranges. The p_T distribution of Ξ^- shows that the predictions of EPOS-LHC and experimental data are compatible in the p_T ranges $2.6 < p_T < 2.8$ GeV/c. The EPOS-1.99 model overestimate at lower p_T region while in the p_T range $1 < p_T < 1.2$ GeV/c, $1.6 < p_T < 1.8$ GeV/c and $2.6 < p_T < 2.8$ GeV/c, the model data seems closer to the experimental data.

Figure (5.9), shows the charged particles rapidity distribution in NSD pp collision. The

rapidity distribution for K_s^0 shows that only EPOS-1.99 model predictions are nearly close to the experimental data while EPOS-LHC, SIBYLL-2.3c and QGSJETII-04 underestimate results as compared with the experimental data. For Λ, the rapidity distribution shows that the EPOS-1.99 models only overestimate the multiplicity values as compared with the experimental data while EPOS-LHC, SIBYLL-2.3c and QGSJETII-04 underestimate them in comparison with the experimental data. The rapidity distribution for Ξ^- shows that the EPOS-1.99 model overestimates values in comparison with those from the experimental data while EPOS-LHC and SIBYLL-2.3c underestimate as compared to the experimental data. Figure (5.10) shows the comparison of strange particles ratio

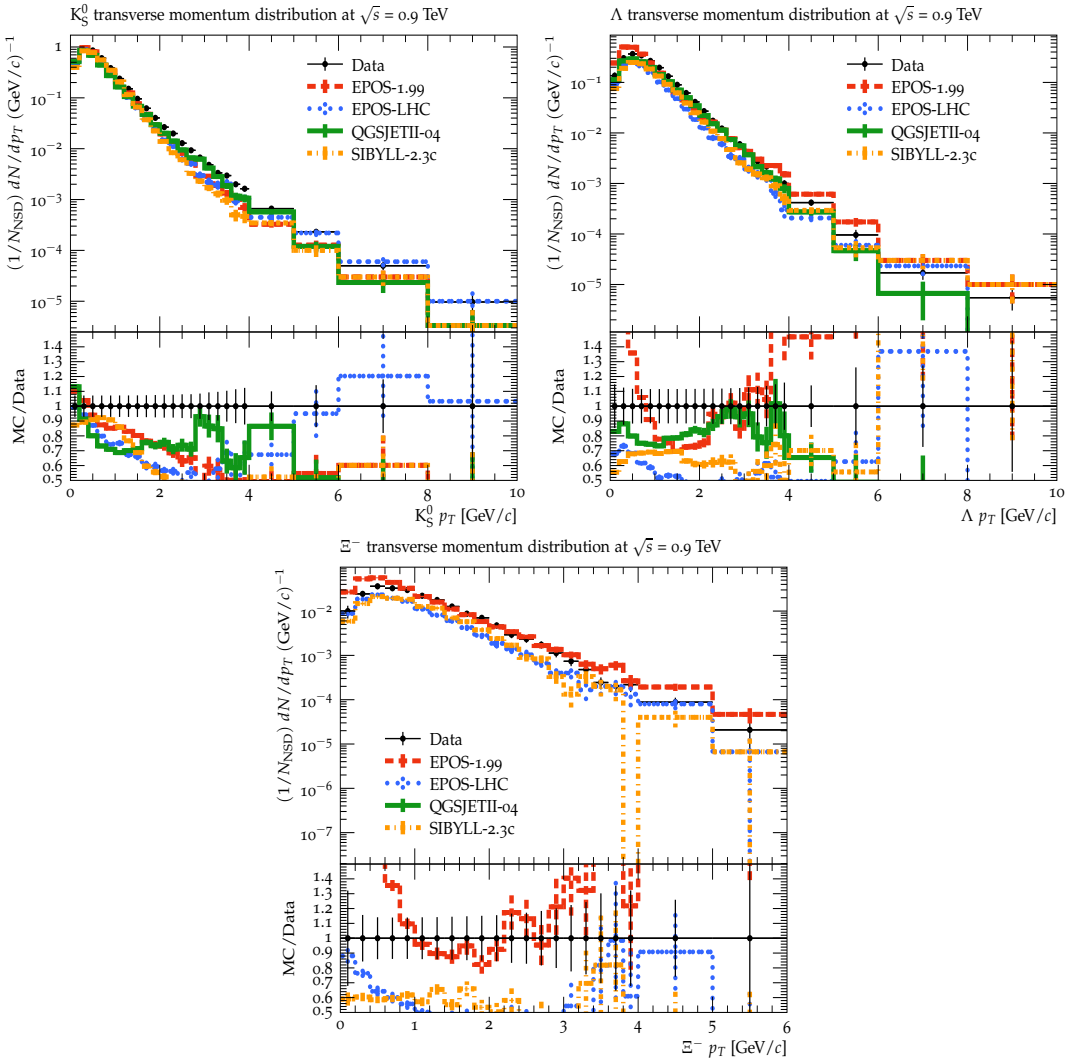

Figure 5.8: *Transverse momentum distributions of the, K_s^0, Λ and Ξ^- at $\sqrt{s}$ = 0.9 TeV from the EPOS-1.99, EPOS-LHC, QGSJETII-04, and SIBYLL-2.3 Models. CMS data is plotted for comparison at 0.9 TeV.*

of Λ/K_s^0 and Ξ^-/Λ distributions versus p_T. Figure (5.10) shows that for $p_T < 2.4$ GeV/c, EPOS-LHC underestimates the multiplicity in comparison with the experimental data while the results from the model coincide with experimental data very well in the p_T range $2.4 < p_T < 2.6$ GeV/c. QGSJETII-04 model explains experimental data very well

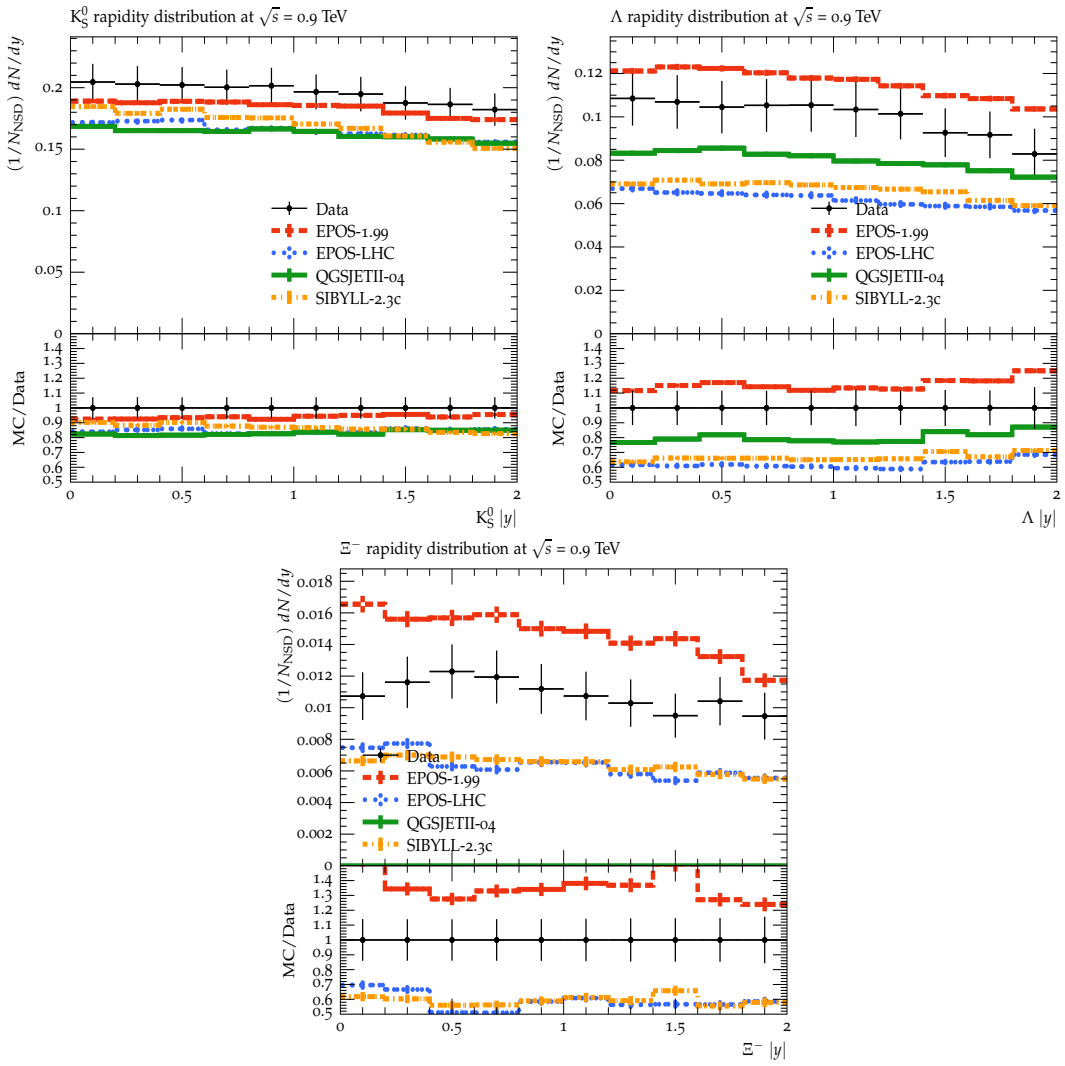

Figure 5.9: *Rapidity distribution of, K^0_s, Λ and Ξ^- at $\sqrt{s}$ = 0.9 TeV from the EPOS-1.99, EPOS-LHC, QGSJETII-04, and SIBYLL-2.3c models. CMS data is plotted for comparison at 0.9 TeV.*

in the p_T range $0.5 < p_T < 1$ GeV/c. Similarly EPOS-1.99, and SIBYLL-2.3c models predictions are closer to the experimental data in the p_T ranges of $1.5 < p_T < 2.2$ GeV/c and $1.3 < p_T < 1.6$ GeV/c respectively. Moreover, for Ξ^-/Λ versus p_T distributions, Figs.(5.10) shows that, EPOS-LHC model overestimates the values at $p_T < 0.4$ GeV/c and its results seem closer to the experimental data in the p_T range $0.6 < p_T < 1.2$ and $1.6 < p_T < 1.8$ GeV/c. The SIBYLL-2.3c model predictions in the p_T range $0.2 < p_T < 0.4$ GeV/c and $1.6 < p_T < 1.8$ GeV/c seem closer to the experimental data.

Figure (5.11) shows the comparison of charged particles ratio of Λ/K^0_s and Ξ^-/Λ distribution versus rapidity. Figsur (5.11) shows that only QGSJETII-04 model can explain experimental data very well in the p_T range of $0.4 < |y| < 0.6$, $1.4 < |y| < 1.6$, and at $|y| > 1.8$ while EPOS-LHC, and SIBYLL-2.3c models data is underestimated while that from EPOS-1.99, is overestimated in comparison with the results from the experimental

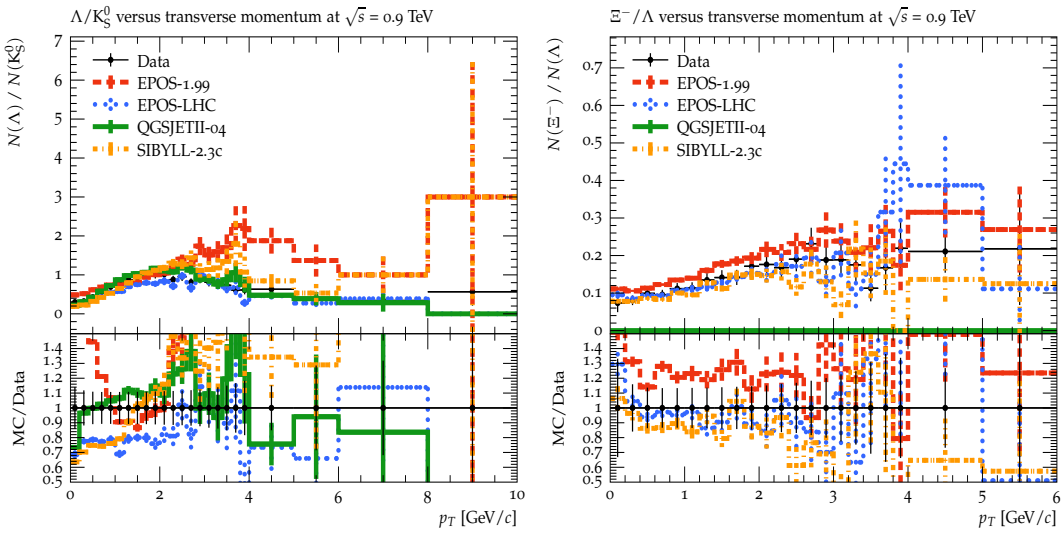

Figure 5.10: *Λ/K_s^0 and Ξ^-/Λ versus p_T distributions at $\sqrt{s}$ = 0.9 TeV from EPOS-1.99, EPOS-LHC, QGSJETII-04, and SIBYLL-2.3 models. CMS data is plotted for comparison at 0.9 TeV.*

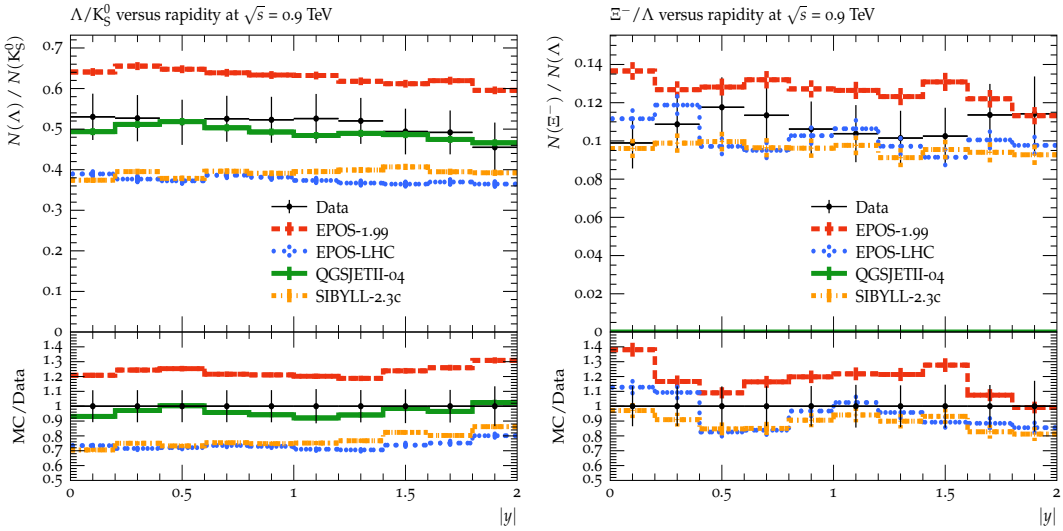

Figure 5.11: *Λ/K_s^0 and Ξ^-/Λ versus rapidity at $\sqrt{s}$ = 0.9 TeV from EPOS-1.99, EPOS-LHC, QGSJETII-04, and SIBYLL-2.3 models. CMS data is plotted for comparison at 0.9 TeV.*

data. In the second distribution of Ξ^-/Λ, the EPOS-1.99 can explain experimental data very well in the rapidity range, $|y| > 1.8$ and EPOS-LHC models' predictions are closer to the experimental data in the rapidity range $0.8 < |y| < 1.9$. Similarly, SIBYLL-2.3c model predictions seem closer to the experimental data in the rapidity region of $|y| < 0.2$ while they are underestimated as compared with the experimental data at $|y| > 0.2$.

5.1.4 Transverse momentum and rapidity distributions of strange particles in pp collisions at $\sqrt{s}$ = 7 TeV

The current analysis is done using selected strange particles, K^0_s, Λ and Ξ^-. The simulation is performed using EPOS-1.99, HIJING-1.0, SIBYLL-2.3c, EPOS-LHC and QGSJETII-04 models. The transverse momentum and rapidity distributions along with the ratio of Monte Carlo to data distribution of the strange particles at $\sqrt{s}$ = 7 TeV in pp collisions have been studied. The models' predictions are compared with the CMS data [190].

Figure. 5.12 (top left), shows the comparison of p_T distribution of the strange particles, K^0_s, Λ and Ξ^- in NSD in pp collisions in the p_T range $0 < p_T < 10$ GeV/c. The p_T distribution for K^0_s shows that for $p_T < 0.3$ GeV/c, EPOS-LHC, and EPOS-1.99 models predictions are closer to the experimental data while QGSJETII-04 and SIBYLL-2.3c models underestimate the values as compared to experimental data. HIJING model gives higher multiplicity in the p_T range, $p_T \approx 0.5$ GeV/c while they become underestimated at $p_T > 0.5$ GeV/c. The figure also shows that for $p_T > 8$ GeV/c SIBYLL-2.3c model overestimates the values as compared to the experimental data.

The p_T distribution for Λ in Fig. 5.12 (top right) shows that in the region $p_T < 0.4$ GeV/c, $p_T < 0.6$ GeV/c, $p_T < 0.8$ GeV/c, the QGSJETII-04, HIJING and EPOS-1.99 models overestimate the values as compared with the experimental data respectively while EPOS-LHC and SIBYLL-2.3c models underestimate them with respect to the experimental data. EPOS-1.99 underestimates the multiplicity up to $p_T = 2.5$ GeV/c and then for $p_T > 2.5$ GeV/c its predictions overestimate as compared to the values coming from the CMS experiment. EPOS-LHC models predictions underestimate up to $p_T = 8$ GeV/c but become closer with the experimental data in the p_T range $p_T > 8$ GeV/c. Similarly, QGSJETII-04 models underestimates the values compared to the experimental data throughout the distribution, while HIJING models underestimate the data points up to $p_T = 5$ GeV/c then overestimate beyond $p_T > 5$ GeV/c. SIBYLL-2.3c underestimate as compared to experimental data up to $p_T \approx 4$ GeV/c. It is observed that SIBYLL-2.3c explains the experimental data very well in the range $4 < p_T < 5$ GeV/c. The quantitative analysis of above distributions is done by taking the ratio of the Model/data in the lower panel of Fig. (5.12). The p_T distribution for Ξ^- in Fig. 5.12 (bottom) shows that only EPOS-1.99 models predictions are closer to the experimental data in the p_T range $1.2 < p_T > 2.4$ GeV/c while rest of the models therefore seem not good enough in this case and require further investigations for their improvements.

Figure (5.13) shows the rapidity distributions of strange particles, K^0_s, Λ and Ξ^-. The Fig. 5.13 (top left) shows the rapidity distribution for K^0_s, in which HIJING model overestimates the values as compared to the experimental data while EPOS-LHC, EPOS-1.99,

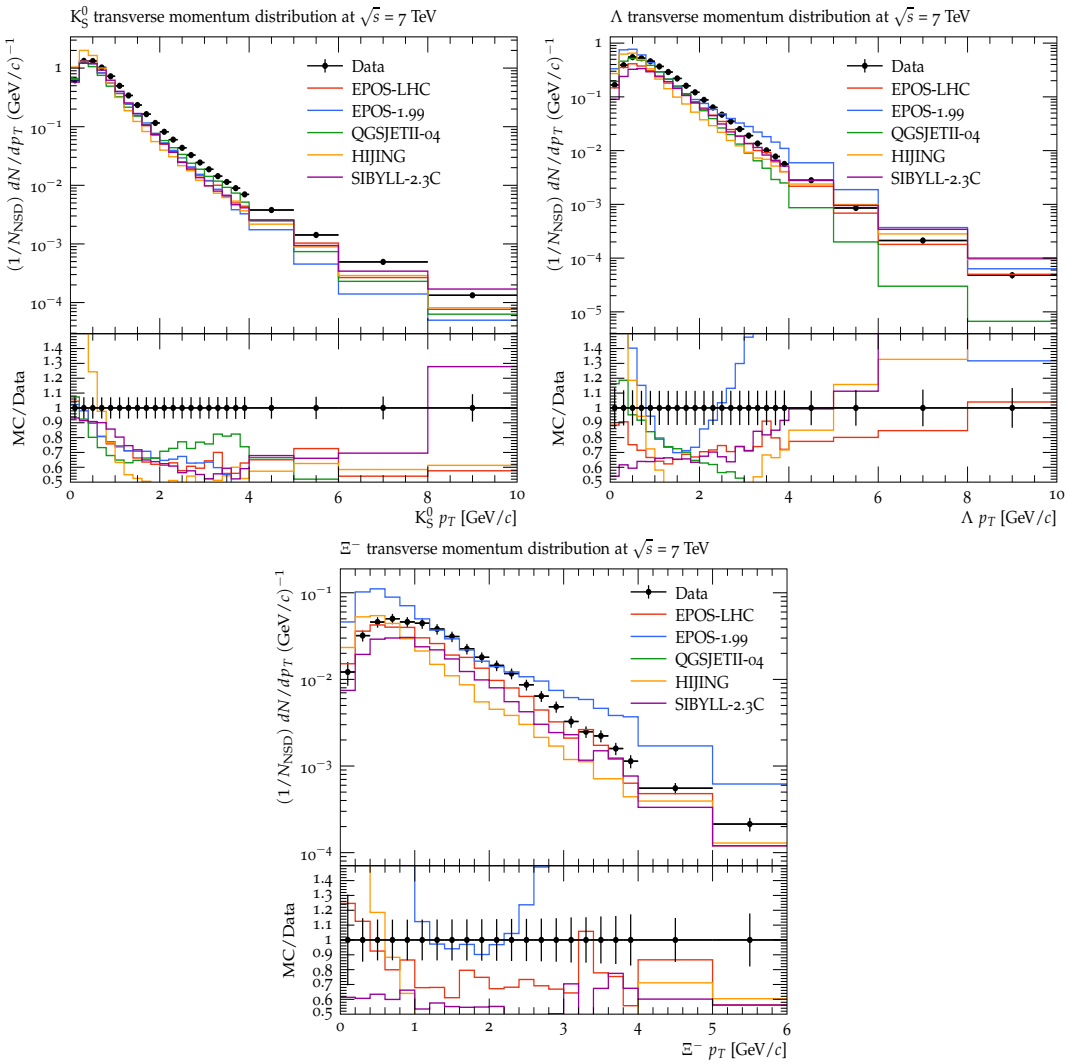

Figure 5.12: *Transverse momentum distributions of the, K^0_s, Λ and Ξ^- at $\sqrt{s}$ = 7 TeV from the EPOS-1.99, EPOS-LHC, QGSJETII-04, and SIBYLL-2.3 Models. CMS data is plotted for comparison at 7 TeV.*

SIBYLL-2.3c and QGSJETII-04 underestimate the values as compared to the experimental data. Figure 5.13 (top right) shows the rapidity distribution for Λ baryon which shows that EPOS-1.99 model overestimates the values as compared to the experimental data while QGSJETII-04 and HIJING models are in good agreement with each other but underestimate them as compared to the experimental data. Similarly EPOS-LHC and SIBYLL-2.3c models also underestimate the values as compared to the experimental data. The rapidity distribution for Ξ^- hyperon is shown in Fig. 5.13 (bottom). One can see that the data points of EPOS-1.99 model are overestimated than the experimental data points while the HIJING and SIBYLL-2.3c models underestimate them as compared with the experimental data. The EPOS-LHC model in the range $p_T < 1.4$ GeV/c underestimate the values as compared to the experimental data while in the range $1.4 < p_T < 1.6$ GeV/c explains the experimental data very well.

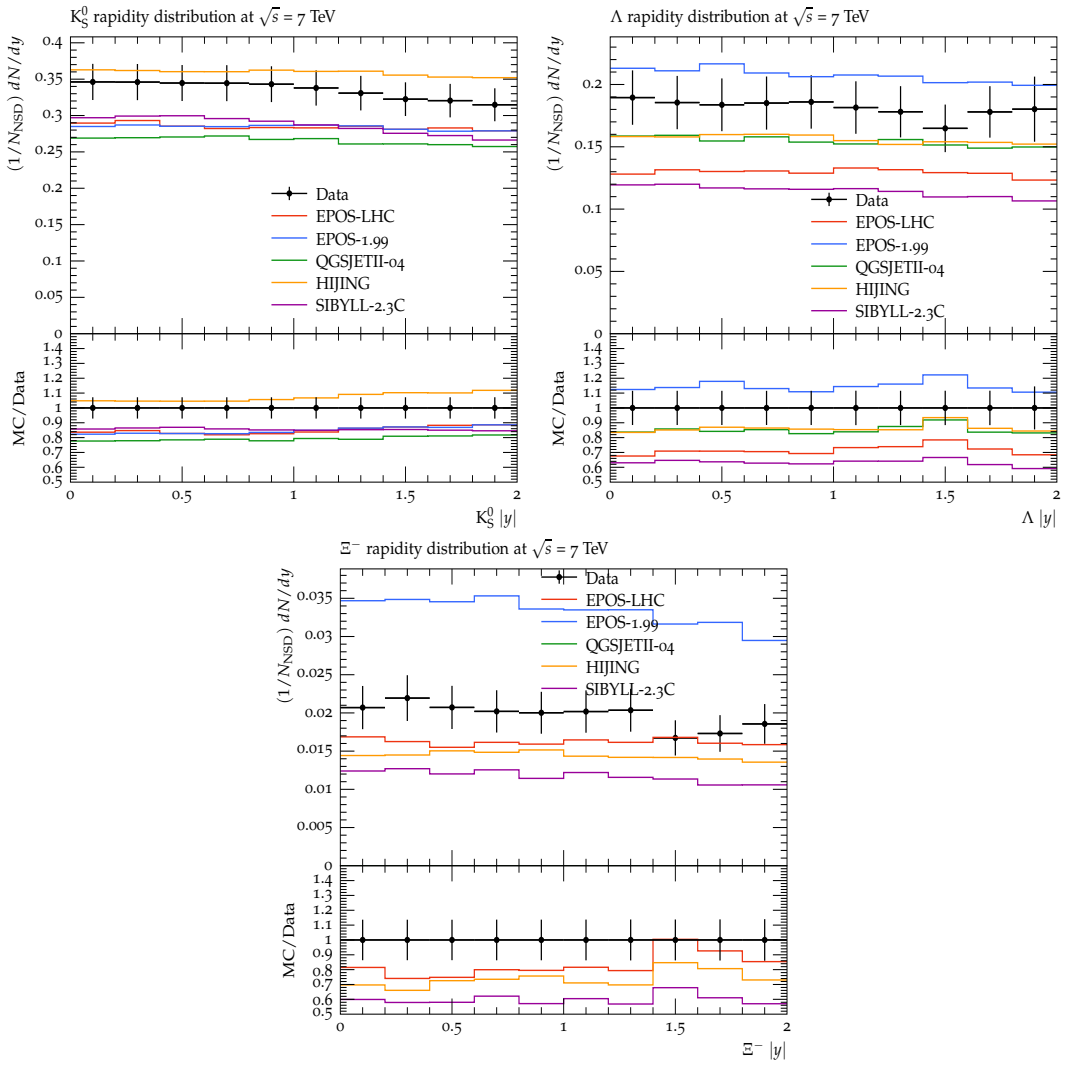

Figure 5.13: *Rapidity distribution of, K^0_s, Λ and Ξ^- at $\sqrt{s}$ = 7 TeV from the EPOS-1.99, EPOS-LHC, QGSJETII-04, and SIBYLL-2.3 models. CMS data is plotted for comparison at 7 TeV.*

Figure (5.14) shows the ratio of yields of Λ/K^0_s and Ξ^-/Λ distributions as a function of p_T. The Fig. 5.14 (left) shows that at low p_T values i.e. $p_T < 2$ GeV/c, EPOS-1.99 and QGSJET-04 overestimate the values in comparison with the experimental data while EPOS-LHC and SIBYLL-2.3c underestimate them. The predictions from HIJING model are closer to the experimental data. In the region of $p_T > 2$ GeV/c the QGSJETII-04 underestimate the values as compared to the experimental data, but rest of the models EPOS-LHC, EPOS-1.99, SIBYLL-2.3c and HIJING overestimate them in comparison with the experimental data. Fig. 5.14 (right) shows the ratio of Ξ^-/Λ, in which one can see that, EPOS-1.99 values are higher than the experimental data while HIJING and EPOS-LHC model overestimate at $p_T < 0.2$ GeV/c and $p_T < 1.4$ GeV/c respectively. As compared to the other models the EPOS-LHC model seems closer to the experimental data. The SIBYLL-2.3c model at $p_T < 1$ GeV/c is closer to the experimental data but at $p_T > 1$ GeV/c it underestimates these values as compared to the experimental data.

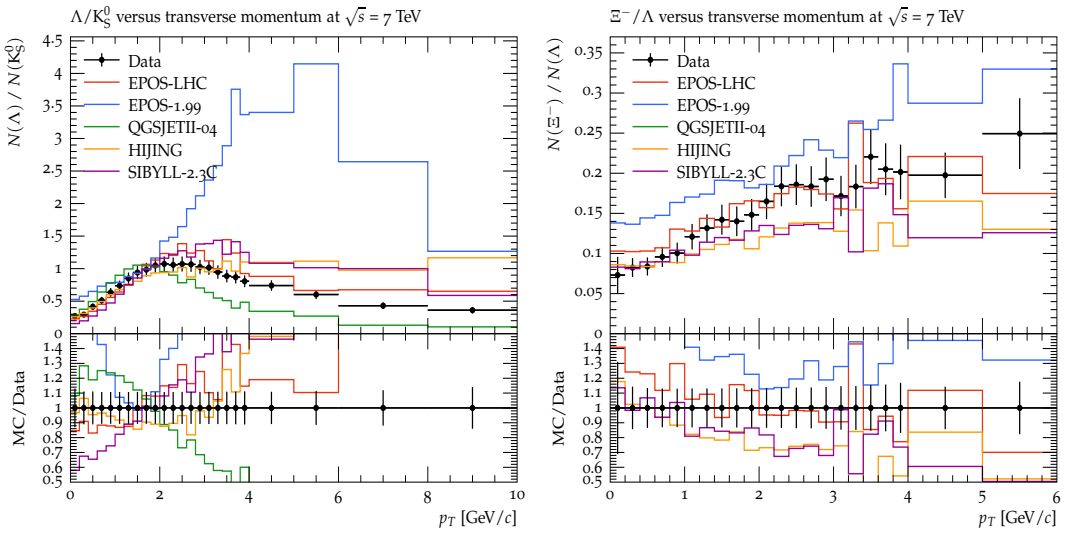

Figure 5.14: *Λ/K_s^0 and Ξ^-/Λ verses p_T distributions at $\sqrt{s}$ = 7 TeV from EPOS-1.99, EPOS-LHC, QGSJETII-04, and SIBYLL-2.3 models. CMS data is plotted for comparison at 7 TeV.*

Figure (5.15) shows the quantitative results by taking the ratio of the yield of Λ/K_s^0 and Ξ^-/Λ as a function of rapidity. The Fig. 5.15 (left panel) shows that EPOS-LHC, HIJING and SIBYLL-2.3c models underestimate the values as compared to the experimental data while EPOS-1.99 and QGSJET-04 models overestimate it with the experimental data. As compared to the SIBYLL-2.3c, EPOS-1.99, HIJING and EPOS-LHC the QGSJETT-04 model is closer to the experimental data. In Fig. 5.15 (right) the distribution shows that EPOS-1.99 and EPOS-LHC models give overestimated values and SIBYLL-2.3c as well as HIJING models underestimate the values as compared with the experimental data. However as compared to the other models the SIBYLL-2.3c and EPOS-LHC models predictions are closer to the experimental data. The rest of the models seem not good enough in this case and therefore require more investigations for their improvements.

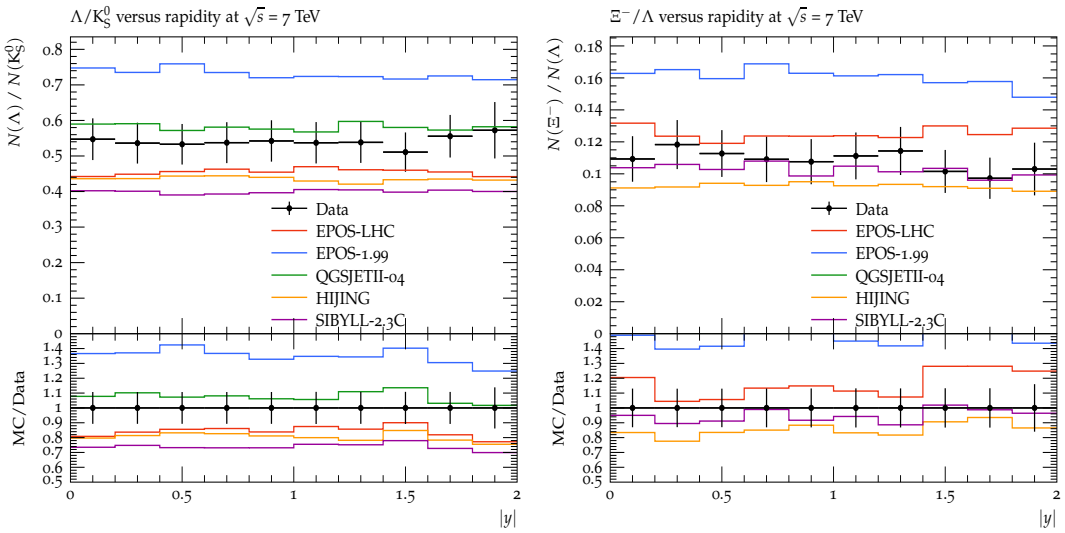

Figure 5.15: *Λ/K_s^0 and Ξ^-/Λ verses rapidity at $\sqrt{s}$ = 7 TeV from EPOS-1.99, EPOS-LHC, QGSJETII-04, and SIBYLL-2.3 models. CMS data is plotted for comparison at 7 TeV.*

5.2 List of Results

In this section we would like to mention main results obtained from our study:

1. The three models (EPOS-LHC, EPOS-1.99 and QGSJETII-04) give approximately the same behaviour for the p_T distribution for the $\pi^{\pm}$, $K^{\pm}$ - mesons, protons and anti-protons with p_T in the interval of $0 < p_T < 20$ GeV/c produced in p-Pb interaction at $\sqrt{s}_{NN} = 0.9$ TeV and 5.02 TeV. These models can not describe the experimental data satisfactorily in the interval of $p_T < 4$ GeV/c but in the region $p_T > 4$ GeV/c models give very good approximation for multiplicities as compared to the experimental data. In the interval of $p_T < 4$ GeV/c, models predictions are systematically greater than the values from the experimental data. So we can say that there are two distinct p_T regions with boundary values at $p_T \simeq 4$ GeV/c. We think that the reason of this result could be that there are multiple particle interactions, because at low energy this dynamics dominates. The result could be confirmed by the data on η distributions. The deviation between the experimental data and the values coming from the simulation data could mean that models can not take into account the collective interactions of partons approximately at low energies.

2. For the $\pi^{\pm}$, $K^{\pm}$ - mesons, protons and anti-protons with p_T in the interval of $0 < p_T < 100$ GeV/c produced in p-Pb interaction at $\sqrt{s}_{NN} = 5.02$ TeV, the models again get problems in describing the data at low p_T regions but give satisfactory predictions in high p_T regions. But in these cases the boundary values of p_T regions are shifted to the values of higher p_T. We have considered this result as some kind of universality behavior because different models (HIJING-1.0 and UrQMD-3.4) use

different dynamics but give same predictions in this region.

3. For the charged particles, $\pi^{\pm}$, $K^{\pm}$ - mesons, protons and anti-protons with p_T in the interval of $0 < p_T < 20$ GeV/c produced in p-Pb interaction at $\sqrt{s}_{NN} =$ 0.9 TeV and 5.02 TeV at high p_T regions universal behaviour of the distribution confirms our conclusion. For the behaviour of NMF, UrQMD-3.4 simulation shows more suppression compared with the HIJING-1.0 model. It may be due to medium effects.

4. For the identified charged particles $\pi^+ + \pi^-$, $K^+ + K^-$ and p + $\bar{p}$, produced in the p-Pb collisions at $\sqrt{s_{NN}} = 5.02$ TeV, the three models (EPOS-LHC, EPOS-1.99 and QGSJETII-04) are in good agreement with the experimental data at low p_T region (soft interaction), while at high p_T region (hard interaction), only EPOS-LHC can explain experimental data very well. For the behaviour of the NMF at low p_T the models prediction are similar to each other up to 3 GeV/c for the case of $K^+ + K^-$ and $p + \bar{p}$. But values of NMF are different for the high p_T regions. Similarly for the $\pi^+ + \pi^-$ mesons, models can not describe the experimental data in the region of $p_T < 2$ GeV/c. This result could be connected to the absorption of pions by the medium more weakly than it is expected by the models. At intermediate p_T region of $2 < p_T < 7$ GeV/c, in case of p + $\bar{p}$, the NMF shows Cronin-like enhancement while pions and kaons show no any modifications. The main conclusion from this result is that there is no suppression, so there is no signature of QGP formation in p-Pb collisions.

5. In the case of p_T, $|\eta|$ and ratio of ($\sqrt{s} = 13$ TeV to 7 TeV) distributions, EPOS-LHC only explain the experimental data very well for the charged particles $\pi^{\pm}$, $K^{\pm}$ - mesons, protons and anti-protons.

6. The study of strange charged particles K^0_s, Λ and Ξ^- at $\sqrt{s} = 0.9$ TeV and 7 TeV results shows that for the Λ/K^0_s and Ξ^-/Λ as a function of p_T distributions, EPOS-LHC describe experimental data very well for the low and high p_T and for the forward rapidity region.

Chapter 6

Summary and Conclusions

We have studied inclusive characteristics of secondary charged particles produced in p-Pb collisions at LHC energies using simulations data coming from different codes. The results have been compared with the ones obtained from pp collisions which act as baseline measurements for Pb-Pb collisions. Transverse momentum and pseudorapidity distributions of the selected charged particles, including $\pi^{\pm}$, $K^{\pm}$, protons and anti-protons have been studied for the pp collisions at $\sqrt{s}_{NN}$ = 0.9 TeV, 5.02 TeV and 7 TeV in non-single diffractive p-Pb collisions at $\sqrt{s}_{NN}$ = 0.9 TeV and 5.02 TeV. The study includes the pseudorapidity regions of $|\eta| < 0.3$, $0.3 < |\eta| < 0.8$, $0.8 < |\eta| < 1.3$, $1.3 < |\eta| < 1.8$ and $1.8 < |\eta| < 2.3$, whereas the transverse momentum ranges are $0 < p_T < 20$ GeV/c and $0 < p_T < 100$ GeV/c. The Nuclear Modification Factor was calculated using the pp collisions as a reference. In addition, charged particles density as a function of charged particles multiplicity, average transverse momentum as a function of charged particles multiplicity, charged particles density as a function of pseudorapidity and charged particles multiplicity have been studied for the pp collisions. We have used several MC event generators such as, HIJING-1.0, UrQMD-3.4, EPOS-LHC, EPOS-1.99, QGSJETII-04 and SIBYLL-2.3c, 150k events to simulated the data for p-Pb and pp interactions each.

The obtained results lead us to the conclusions that:

1. There is some universality in behavior of the characteristics of the charged high p_T particles with $0 < p_T < 20$ GeV/c and for the ones with $0 < p_T < 100$ GeV/c.
2. The UrQMD model gives more suppression as compared to HIJING which can be due to some medium effect thus produced.
3. The EPOS-LHC, EPOS-1.99, QGSJETII-04 codes give good predictions for the soft interactions and only EPOS-LHC can explain hard interactions satisfactorily.
4. The models show that the pions at low p_T are absorbed by the medium weakly than it is expected by the relevant models.
5. The Cronin-like enhancement was observed for the (anti) protons with intermediate

p_T.

6. There can not be observed any suppression in the p-Pb collisions.
7. EPOS-LHC model describes the experimental data better as compared to EPOS-1.99 and QGSJETII-04 models.

References

[1] Fayyazuddin and Riazuddin, "A modern introduction to particle physics", 3rd Ed. World Scientific (2011).

[2] P. B. Munzinger, *et al.,* Nucl. Phys. A 987, 144 (2019).

[3] W. Busza, *et al.,* Ann. Rev. Nucl. Part. Sci. 68, 1 (2018).

[4] D. G. d' Enterria and D. Peressonuko, Eur. Phys. J. C 46, 451 (2006).

[5] M. Klasen, *et al.,* J. High Energy Phys. 1310, 119 (2013).

[6] K. Aamodt, *et al.,* (ALICE Collaboration), Phys. Lett. B 696, 328 (2011).

[7] R. A. Dunlap, "An introduction to the physics of nuclei and particles", Brooks/Cole-Thomson Learning Inc. (2003).

[8] D. Griffiths, Introduction to elementary particle physics, John Wiley Sons Inc. (1987).

[9] G. Aad, *et al.,* (ATLAS Collaboration), Phys. Lett. B 716, 1 (2012).

[10] S. Chatrchyan *et al.,* (CMS Collaboration), Phys. Lett. B 716, 30 (2012).

[11] D. Perkins, "Introduction to high energy physics", 3rd Ed. (Addison-Wesley, London, 1987).

[12] J. E. Augustin, *et al.,* Phys. Rev. Lett. 33, 1406 (1974).

[13] The Standard Model, http://en.wikipedia.org/wiki/Particle physics/media/File

[14] E. D. Bloom, *et al.,* Phys. Rev. Lett. 23, 930 (1969).

[15] J. Bjorken and E. A. Paschos, Phys. Rev. 185, 1975 (1969).

[16] M. Gell-Mann, Phys. Lett. 8, 214 (1964).

[17] G. Zweig, CERN-TH-412, NP-14146, PRINT-64-170 (1964).

[18] V. Barnes, *et al.,* Phys. Rev. Lett. 12, 204 (1964).

[19] K. G. Wilson, Phys. Rev. D 10, 2445 (1974).

[20] M. C. Diamantini, Commun. Phys. 1, 77 (2018).

[21] G. M. Prosperi, *et al.,* Prog. Part. Nucl. Phys. 58, 438 (2007).

[22] S. Bethke, Prog. Part. Nucl. Phys. 58, 351 (2007).

[23] R. K. Ellis, *et al.,* Part. Part. Nucl. Phys. Cosmol. 8, 1 (1996).

[24] K. Yagi, *et al.,* Part. Phys. Nucl. Phys. Cosmol. 23, 1 (2005).

[25] K. Nakamura, (Particle Data Group), J. Phys. G 37, 075021 (2010).

[26] B. Muller, "The Physics of the Quark-Gluon Plasma", Lecture Notes in Physics 225, Springer, Berlin (1985).

[27] R. C. Hwa, "Quark Gluon Plasma", World Scientific, Singapore (1990).

[28] R. C. Hwa, "Quark Gluon Plasma", World Scientific, Singapore (1995).

[29] P. B. Munzinger, *et al.,* Nucl. Phys. A 610 (1996).

[30] http://www.kheper.net/cosmos/universe/CosmicTimeline.jpg. [cited on page 5]

[31] J. C. Collins and M. J. Perry, Phys. Rev. Lett. 34, 1353 (1975).

[32] E. V. Shuryak, Phys. Rept. 61 158, (1980).

[33] J. Baechler, *et al.,* Nucl. Phys. A 525, 226 (1991).

[34] M. Gaździcki, *et al.,* Nucl. Phys. A 498, 384 (1989).

[35] E. Andersen, *et al.,* Phys. Lett. B 449, 406 (1999).

[36] J. Rafelski and B. Muller, Phys. Rev. Lett. 48, 1066 (1982).

[37] T. Matsui and H. Satz, Phys. Lett. B 178, 416 (1986).

[38] M. C. Abreu, *et al.,* Phys. Lett. B 410, 343 (1997).

[39] R. Arnaldi, *et al.,* Nucl. Phys. A 774, 76 (2006).

[40] A. Adare, *et al.,* Phys. Rev. C 84, 054912 (2011).

[41] B. B. Abelev *et al.,* Phys. Lett. B 734, 327 (2014).

[42] T. Matsui and H. Satz, Phys. Lett. B 178, 416 (1986).

[43] D. G. Moon, *et al.,* (CMS Collaboration), Nucl. Phys. A 904, 591 (2013).

[44] C. Y. Wong, "Introduction to high energy heavy ion collision", World Scientific Publishing Co. (1994).

[45] R. Stock, "Relativistic nucleus-nucleus collisions and the QCD matter phase diagram", Springer-Verlag (2008).

[46] A. Adare, *et al.,* Phys. Rev. C 91, 064904 (2015).

[47] J. Adam, *et al.,* Phys. Lett. B 754, 248 (2016).

[48] J. D. Bjorken, FERMILAB-PUB 82, 059 (1982).

[49] K. Aamodt, *et al.,* (ALICE Collaboration), Phys. Lett. B 696, 30 (2011).

[50] K. Aamodt, *et al.,* (ALICE Collaboration), Phys. Rev. Lett. 108, 092301 (2012).

[51] S. Chatrchyan, *et al.,* (CMS Collaboration), Eur. Phys. J. C 72, 1945 (2012).

[52] A. Adcox, *et al.,* (PHENIX Collaboration), Nucl. Phys. A 757, 184 (2005).

[53] J. Adams, *et al.,* (STAR Collaboration), Nucl. Phys. A 757, 102 (2005).

[54] B. B. Back, *et al.,* (PHOBOS Collaboration), Nucl. Phys. A 757, 28 (2005).

[55] B. Hong, *et al.,* (BRAHMS Collaboration), Nucl. Phys. A 757, 1 (2005).

[56] R. Stock, arXiv: nucl. exp. 0807.1610, 10 (2008).

[57] E. Applet, "Jet and charged hadron nuclear modification factor in pPb collisions with CMS" Talk given at Quark Matter, 2014.

[58] M. L. Miller, Ann. Rev. Nucl. Part. Sci. 57, 205 (2007).

[59] S. Chatrchyan, *et al.,* (CMS Collaboration), Phys. Rev. C 87, 014902 (2013).

[60] A. Saini, *et al.,* J. Nucl. P. Phys. 4, 164 (2014).

[61] S. Voloshin and Y. Zhang, Z. Phys. C 70, 665 (1996).

[62] J. Adams, *et al.,* (STAR Collaboration) Phys. Rev. C 72, 014904 (2005).

[63] K. Aamodt, *et al.,* (ALICE Collaboration), Phys. Rev. Lett. 105, 252302 (2010).

[64] S. Chatrchyan, *et al.,* (CMS Collaboration), Phys. Rev. C 87, 014902 (2013).

[65] M. Krzewicki, (ALICE Collaboration), J. Phys. G 38, 124047 (2011).

[66] T. D. Lee and G. C. Wick, Phys. Rev. D 9, 2291 (1974).

[67] E. V. Shuryak, Sov. Phys. JETP, 47, 212 (1978).

[68] G. Baym, Nucl. Phys. A 698, XXIII (2002).

[69] I. Zakout and C. Greiner, arXiv:1002.3119.v5 [nucl-th] 29 Nov (2010).

[70] Z. Fodor and S. Katz, JHEP 0404, 050 (2004).

[71] S. Gupta, J. Phys. G 35, 104018 (2008).

[72] M. A. Stephanov, Prog. Theor. Phys. Suppl. 153, 139 (2004).

[73] B. Pacík, http://www.quantumdiaries.org/2010/04/26/the-quark-gluon-plasma/.Accessed: 2016-04-10.

[74] J. Gomez, *et al.,* (CMS Collaboration), CMS-NOTE-AN-10-412, (2010).

[75] K. Krajczar, J. Phys. G 38, 124041 (2011).

[76] J. Bjorken, Phys. Rev. D 27, 140 (1983).

[77] R. Sahoo, "Relativistic kinematics", arXiv: [nucl-ex] 1604.02651v1 10 April (2016).

[78] http://en.wikipedia.org/wiki/Pseudorapidity.

[79] G. Roland, *et al.,* Prog. Part. Nucl. Phys. 77, 70 (2014).

[80] L. Evans and P. Bryant, LHC Machine, JINST 3, S 08001 (2008).

[81] O. S. Bruning, *et al.,* CERN (2004), CERN-2004-003-V-1, CERN-2004-003.

[82] O. Buning, *et al.,* CERN (2004), CERN-2004-003-V-2, CERN-2004-003.

[83] M. Benedikt, *et al.,*, CERN (2004), CERN-2004-003-V-3, CERN-2004-003.

[84] Holzer, *et al.,*, CERN Yellow Report CERN-2017-004-SP pp. 253-284 arXiv:1804.08873 [physics.acc-ph]

[85] K. Nakamura, *et al.,* (PDG) JPG 37, 075021 (2010).

[86] K. Aamodt, *et al.,* (ALICE Collaboration), JINST 3, S08002 (2008).

[87] G. Aad *et al.,* (ATLAS Collaboration), JINST 3, S08003 (2008).

[88] S. Chatrchyan, *et al.,* (CMS Collaboration), JINST 3, S08004 (2008).

[89] A. Augusto, *et al.,* (LHCb Collaboration), JINST 3, S08005 (2008).

[90] O. Adriani, *et al.,* (LHCf Collaboration), JINST 3, S08006 (2008).

[91] G. Antchev, *et al.,* Nucl. Instrum. Meth. A 617, 62 (2010).

[92] J. Pinfold, *et al.,* (MoEDAL Collaboration), CERN (2009), CERN-LHCC-2009-006. MoEDAL-TDR-001.

[93] C. Lefèvre, The CERN accelerator complex, CERN CDS, (2008).

[94] S. Chapeland, (ALICE Collaboration), CERN (1995), CERN/LHCC/95-71, LHCC/P3.

[95] K. Aamodt, *et al.,* (ALICE Collaboration), JINST 3, S08002 (2008).

[96] F. Carminati, *et al.,* (ALICE Collaboration), J. Phys. G 30, 1517 (2004).

[97] B. Alessandro, *et al.,* (ALICE Collaboration), J. Phys. G 32, 1295 (2006).

[98] J. Alme, *et al.,* The ALICE TPC, 622, 316 (2010).

[99] L. Betev, *et al.,* (ALICE Collaboration), CERN (2003), ALICE-INT-2003-038.

[100] C. Lippmann and D. Vranic, ALICE TPC Numbering Conventions CERN (2007).

[101] G. Dellacasa, (ALICE Collaboration), CERN (1999), CERN /LHCC 99-12, ALICE TDR 4.

[102] K. Aamodt *et al.,* (ALICE Collaboration), JINST 0803, S08002 (2008).

[103] P. Cortese, (ALICE Collaboration), CERN (2001), ALICE-TDR-9, CERN-LHCC-2001-021, LYCEN-2001-97.

[104] A. TDR, (ALICE Collaboration), CERN (2000), ALICE-TDR-8, CERN-LHCC-2000-012.

[105] G. Dellacasa, *et al.,* (ALICE Collaboration), CERN (2002), ALICE-TDR-8-add-1, CERN-LHCC-2002-016.

[106] C. Lippmann. Particle identification. Nucl. Instrum. Meth., A666:148, (2012).

[107] G. Conesa, *et al.,* (ALICE Collaboration), CERN (2006), CERN-LHCC-2006-014, CERN/LHCC 96-32-Add3.

[108] P. Cortese, *et al.,* (ALICE Collaboration), CERN-LHCC-2008-014, ALICE-TDR-014.

[109] J. D. Groot, *et al.,* (ALICE Collaboration), CERN (1999), CERN/LHCC 99-4, ALICE TDR 2.

[110] J. D. Groot, *et al.,* (ALICE Collaboration), CERN (1998), CERN / LHCC 98-19, ALICE TDR 1.

[111] W. Fischer, *et al.,* CERN–ACC–2015–0015, 22 January (2015).

[112] P. Cortese, *et al.,* (ALICE Collaboration), CERN (2004), CERN-LHCC-2004-025, ALICE-TDR-011.

[113] E. Abbas, *et al.,* (ALICE Collaborations), JINST P 8, 10016 (2013).

[114] B. Alessandro, *et al.,* (ALICE Collaboration), CERN (1999), CERN /LHCC 99-32, ALICE TDR 6.

[115] H. D. Groot, (ALICE Collaboration), CERN (2003), CERN /LHCC 2003-038, Addendum 1 to ALICE TDR 6.

[116] J. D. Groot, (ALICE Collaboration), CERN (1999), CERN/LHCC 99-5, ALICE TDR 3.

[117] P. Crochet, *et al.,* (ALICE Collaboration), CERN (1996), CERN/LHCC 96-53, LHCC/P3-Addendum 1.

[118] Antinori, *et al.,* (ALICE Collaboration), CERN (1999), CERN/LHCC 99-22, ALICE TDR 5.

[119] A. Morsch,*et al.,* Eur. Phys. J. C 34, 317 (2004).

[120] X. -N. Wang and M. Gyulassy, Phys. Rev. D 44, 3501 (1991).

[121] A. Bialas, *et al.,* Nucl. Phys. B 291, 793 (1987).

[122] B. Andersson, *et al.,* Phys. Rep. 97, 31 (1983).

[123] M. Connors, *et al.,* (ALICE Collaboration), Nucl. Phys. A 931, 1174 (2014).

[124] D. Stump, *et al.,* J. High Energy Phys. 10, 046 (2003).

[125] B. Andersson, *et al.,* Nucl. Phys. B 281, 289 (1987).

[126] A. Capella, *et al.,* Z. Phys. C 3, 329 (1980).

[127] J. Ranft, Phys. Rev. D 37, 1842 (1988).

[128] J. Ranft, Phys. Lett. B 188, 379 (1987).

[129] M. Gyulassy and M. Plumer, Phys. Lett. B 243, 432 (1990).

[130] J. Ashman, *et al.,* (EM Collaboration), Phys. Lett. B 202, 603 (1988).

[131] X. N. Wang and M. Gyulassy, Phys. Rev. Lett. 68, 148 (1992).

[132] M. Gyulassy, *et al.,* Nucl. Phys. A 538, 37c (1992).

[133] X. N. Wang and M. Gyulassy, Phys. Rev. D 44, 3501 (1991).

[134] X. N. Wang and M. Gyulassy, Phys. Rev. D 45, 844 (1992).

[135] E. Eichten, *et al.,* Rev. Mod. Phys. 56, 579 (1984).

[136] D. W. Duke and J. F. Owens, Phys. Rev. D 30, 50 (1984).

[137] P. l'Heureux, *et al.,* Phys. Rev. D 32, 1681 (1985).

[138] K. Geiger and B. Muller, Nucl. Phys. B 369, 600 (1992).

[139] S. A. Bass, *et al.,* Prog. Part. Nucl. Phys. 41, 255 (1998).

[140] T. Sjostrand, *et al.,* Comput. Phys. Commun. 135, 238 (2001).

[141] S. Ostapchenko, *et al.,* Phys. Rev. D 74, 014026 (2006).

[142] H. J. Drescher, Phys. Rept. 350, 93 (2001).

[143] M. Stefaniak, EPJ Web of Conferences 164, 07013 (2017).

[144] K. Werner, *et al.,* Phys. Rev. C 74, 044902 (2006).

[145] M. Stefaniak, *et al.,* EPJ Web Conf. 164, 07013 (2017).

[146] H. J. Drescher *et al.,* Physics Reports, 350 93 (2001).

[147] W. D. Apel, *et al.,* Nucl. Part. Phys. 36, 035201 (2009).

[148] D. Heck, *et al.,* FZKA-6019, (1998).

[149] T. Pierog, *et al.,* Phys. Rev. C 92, 034906 (2015).

[150] T. Pierog, J. of Physics: Conference Series 409, 012008 (2013).

[151] K. Werner, *et al.,* Phys. Rev. C 82, 044904 (2010).

[152] S. Ostapchenko, Phys. Rev. D 83, 014018 (2011).

[153] V. N. Gribov, Sov. Phys. JETP 26, 414 (1968).

[154] M. Baker, *et al.,* Phys. Rept. 28, 1 (1976).

[155] D. d'Enterria, *et al.,* Astropart. Phys. 35, 98 (2011).

[156] S. Ostapchenko, EPJ Web Conf. 52, 02001 (2013).

[157] V. N. Gribov, Sov. Phys. JETP 29, 483 (1969).

[158] R. J. Glauber and G. Matthiae, Nucl. Phys. B 21, 135 (1970).

[159] R. S. Fletcher, *et al.,* Phys. Rev. D 50, 5710 (1994).

[160] F. Riehn, *et al.,* PoS ICRC 2015, 558 (2016).

[161] E. -J. Ahn, *et al.,* Phys. Rev. D 80, 094003 (2009).

[162] A. Capella and A. Krzywicki, Phys. Rev. D 18, 3357 (1978).

[163] A. Capella and J. Tran Thanh Van, Z. Phys. C 10, 249 (1981).

[164] A. Capella, *et al.,* Phys. Rept. 236, 225 (1994).

[165] T. K. Gaisser and F. Halzen, Phys. Rev. Lett. 54, 1754 (1985).

[166] G. Pancheri and Y. Srivastava, Conf. Proc. C 850313, 28 (1985).

[167] L. Durand and P. Hong, Phys. Rev. Lett. 58, 303 (1987).

[168] H. -U. Bengtsson and T. Sjostrand, Comput. Phys. Commun. 46, 43 (1987).

[169] T. Sjostrand, Int. J. Mod. Phys. A 3, 751 (1988).

[170] M. L. Good and W. D. Walker, Phys. Rev. 120, 1857 (1960).

[171] R. J. Glauber and G. Matthiae, Nucl. Phys. B 21, 135 (1970).

[172] J. Engel, *et al.,* Phys. Rev. D 46, 5013 (1992).

[173] R. Brun and F. Rademakers, Nucl. Instrum. Meth. A 389, 81 (1997).

[174] I. Antcheva, *et al.,* CPC 180, 2499 (2009).

[175] "PAW webpage". http://paw.web.cern.ch/paw/.

[176] W. Verkerke, *et al.,* RooFit Users Manual, v2.91 14 October (2008).

[177] AliRoot, http://svnweb.cern.ch/world/wsvn/AliRoot/.

[178] http://projects.hepforge.org/rivet/trac/wiki.

[179] http://savannah.cern.ch/projects/hepmc/.

[180] E. Boos, *et al.,* arXiv:hep-ph/0109068.

[181] C. Oppedisano, (ALICE Collaboration), Nucl. Phys. A 932, 399 (2014).

[182] B. Abelev, *et al.,* (ALICE Collaboration), Phys. Rev. Lett. 110, 082302 (2013).

[183] V. Khachatryan, *et al.,* Eur. Phys. J. C 75, 237 (2015).

[184] J. Velkovska, (CMS Collaboration), CERN Report No. CMS-PAS-HIN-12-017, (2013).

[185] E. Shulga, (ATLAS Collaboration), J. Phys. Conf. Ser. 798 012066 (2017).

[186] B. Abelev, *et al.,* (ALICE Collaboration), Phys. Rev. Lett. 110, 082302 (2013).

[187] J. Adam, *et al.,* (ALICE Collaboration), CERN-EP-2016-003, (2016).

[188] G. Aad, *et al.,* (ATLAS Collaboration), Phys. Lett. B 688, 21 (2010).

[189] J. Adam, *et al.,* (ALICE Collaboration), Phys. Lett. B 753, 319 (2016).

[190] V. Khachatryan, *et al.,* (CMS Collaboration), J. High Energy Phys. 05, 064 (2011).